Multiplexed, scalable, and functionality compatible platforms for 3D spatially resolved proteomic profiling

by

Yuxuan Tian

B.E., Chemical Engineering, Tsinghua University, 2016

Submitted to the Department of Chemical Engineering
in partial fulfillment of the requirements for the degree of

Doctor of Philosophy in Chemical Engineering

at the

MASSACHUSETTS INSTITUTE OF TECHNOLOGY

May 2024

Authored by……………………………………………………………………………………..
Yuxuan Tian
Department of Chemical Engineering
May 3, 2024

Certified by……………………………………………………………………………………...
Kwanghun Chung
Associate Professor of Chemical Engineering
Thesis supervisor

Accepted by…………………………………………………………………………………….
Hadley D. Sikes
Willard Henry Dow Professor of Chemical Engineering
Chairman, Committee for Graduate Students

Multiplexed, scalable, and functionality compatible platforms for 3D spatially resolved proteomic profiling

by

Yuxuan Tian

Submitted to the Department of Chemical Engineering on May 5, 2024
in partial fulfillment of the requirements for the degree of
Doctor of Philosophy in Chemical Engineering

Abstract

Extracting and interpreting the network of biomolecular information is crucial for comprehending complex biological systems. Due to the highly dynamic, deeply interconnected network of various biomolecules, it is necessary to characterize the spatial distribution and molecular functionality of biomolecules within the context of their local microenvironment and their interactive role in the whole biomolecular network. Spatial proteomics serves as an indispensable tool for extracting and deciphering cellular and molecular information of proteins, one of the important type of functional biomolecules, within biological systems. However, compared with high throughput technologies such as single cell sequencing or spatial transcriptomics, its widespread application is often hindered by the constrained volumetric scalability and multiplexing capability inherent in current approaches.

Additionally, existing spatial proteomics focus more on capturing the information of molecular identity and their spatial locations, often neglecting the information of functionality. Since proteins, together with other functional biomolecules (glycans, neurotransmitters, lipids, etc.), are major participants of biological processes, their functionality profile can provide valuable insights into molecular recognition, signal transduction, and functional abnormality directly related to disease diagnostics and therapeutics. However, the widely used chemical fixation protocols don’t support functional detection of proteins, triggering the development of new tissue preservation technology for the unfulfilled aim of spatially resolved functional detection.

To address these challenges, two projects were implemented during my PhD to improve the volumetric scalability, multiplexing capacity, and the possibility of spatially resolved functional detection of spatial proteomics. Here we firstly present a robust, easy-to-implement 3D proteomic mapping platform with both volumetric and multiplexing scalability. With this platform, multiround, multichannel protein detection can be achieved on millimeter scale tissues in a unique buffer environment. We showcased two modalities for 3D proteomic analysis: dense labeling, better at morphological characterization of cytoarchitectures, and stochastic sparse labeling, compatible to combinatorial barcoding strategy for enhanced multiplexing scalability. Eventually, we displayed the potential of our spatial proteomic platform by performing comparative cellular profiling, pathological investigation and structural characterization on multiple regions between long banked human brain samples diagnosed with Alzheimer’s Disease and control. Additionally in the second project, we developed a fixative-free technology enabling 3D in situ functional detection of proteins. As a demonstration, we confirmed the mechanical interlocking effect on various types of biological tissues, and verified the entanglement between dense polymer chains and biomolecules. As we predicted, signals of enzymatic activity from endogenous proteases in mouse colon tissues were successfully captured in 3D, spatially resolved way. Together, we envision that our results will serve as pioneering technologies to enable spatial proteomic profiling with better volumetric scalability, multiplexing capacity, and possibility of spatially resolved functional detection.

Thesis supervisor: Kwanghun Chung

Title: Associate Professor of Chemical Engineering

Acknowledgements

I’d like to express my sincere gratitude to my advisor and mentor, Professor Kwanghun Chung, for all the support, mentorship and guidance in my academic ambitions, inspirations, communication skills, as well as research details. I’d also like to thank all of my thesis committee members, Professor J. Christopher Love and Professor K. Dane Wittrup, for your valuable suggestions on my projects and the possibilities of my future career. I’m lucky to receive your mentorship along with my journey of the entire PhD program.

I’d like to express my thanks to all of my colleagues that I have worked with on multiple projects and collaborations. I’m very grateful that I can meet all of the outstanding research scientists, post docs, graduate students, lab mates at MIT, who not only taught me their knowledge and expertise, shared their research experiences, but also supported me to go through challenges. From the valuable experience of working with them, I learned the importance of collaborative teamwork.

Finally, I’d like to thank my family and friends who keep supporting me physically and emotionally throughout this journey. My father (Lin Tian) and my mother (Chunyan Lu) were always there for me no matter how frustrated I felt. I’m grateful they never complained that I rarely went home, and tried to visit me across such long distance. And I’d like to thank all my friends from my high school, undergraduate college, and graduate school, no matter where they are now. They really made my life outside labs interesting and colorful. I’m so grateful that my PhD was full of so much happy memories with them all.

Table of Contents

List of Figures

List of Tables

Chapter 1. Introduction

1.1 Brain and its biomolecules

Complex functions of mammalian organs require the engagement and the precise regulation of an enormous diversity of biochemical processes. The integration of such complicated cellular functionality requires systematic coordination of a huge variety of cells, and more fundamentally, the huge variety of biomolecules that facilitate the physiological processes. Throughout the process of gene expression, energy conversion, signal communication, and specialized function implementation, almost all of the cellular behaviors rely on the interaction of multiple types of molecules, including DNA, RNA, proteins, lipids, carbohydrates, neurotransmitters, metabolites, etc (**Figure 1-1 a**). Therefore, the spatial context and the microenvironment of biomolecules are not supposed to be neglected for interactive and comprehensive understanding of biomolecular networks.

Among all mammalian organs, brains are one of the most complicated with billions of neurons and glia, highly regionalized based on anatomical and functional conditions[1,2]. Due to such complexity, it remains challenging to precisely study the molecular identity and the interactive network of individual biomolecules in human brains. Ever since the emergence of high throughput technologies such as single cell sequencing, the way of molecular/cellular characterization in brains has been revolutionized into highly multiplexed analysis of genes, transcripts and other biomolecules. Therefore, although classic histology based molecular detection has enabled countless insightful discoveries in the whole biological research field, the multiplexing capacity is far less than the diversity of biomolecules, limiting the systematic analysis of the local interactive biomolecular network. With the development of spatially resolved multi-omics technologies, we are able to investigate on many central nervous system related questions within the context of overall genome, transcriptome, proteome and/or metabolome.

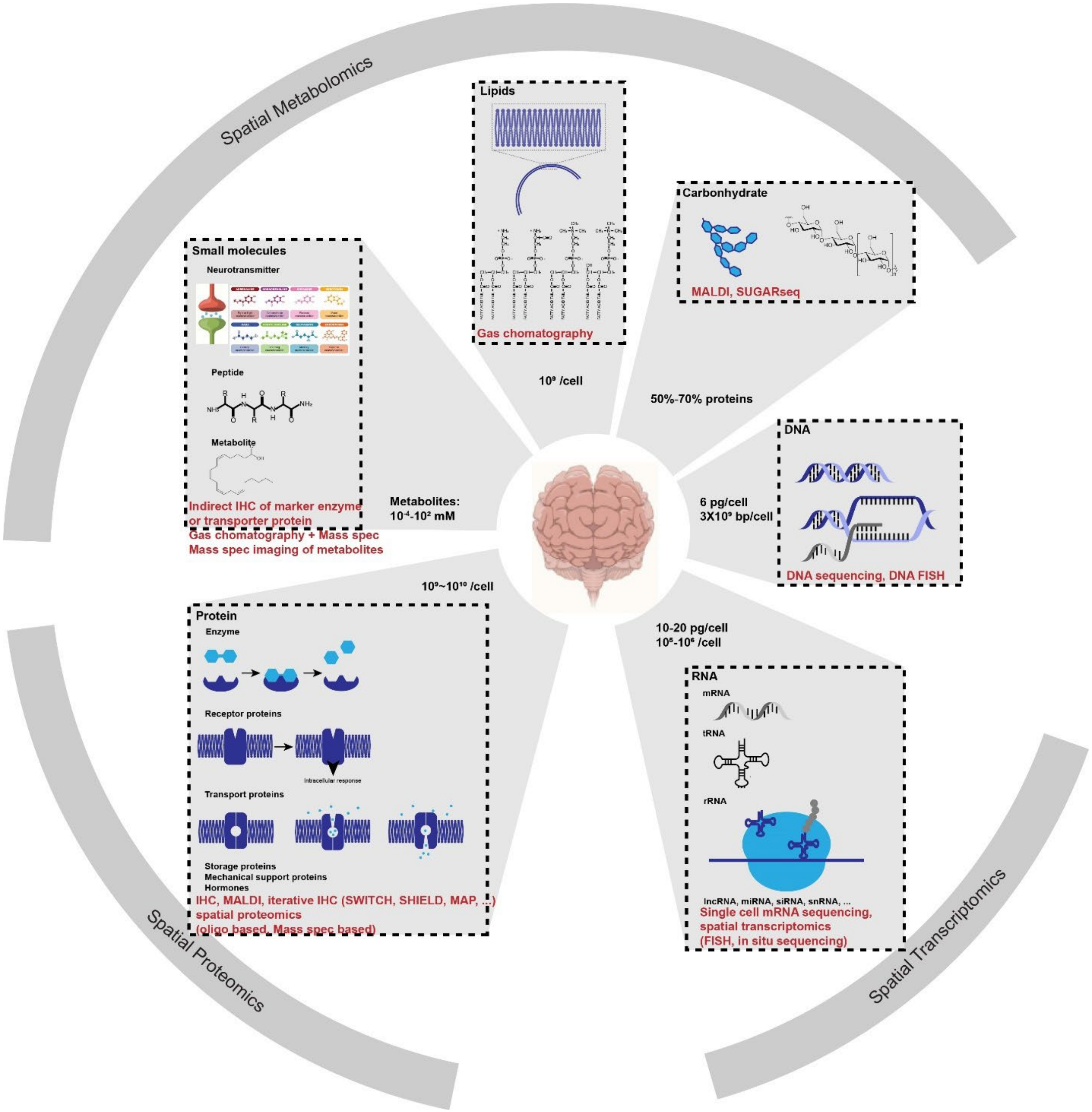

Figure 1-1. Major categories of biomolecules inside brains, and respective technologies to study them.

1.2 Chemistry for biomolecule preservation

Cells, in the context of tissues, organs, and individual organisms, have complicated functions that require coordination of multiple types of biomolecules (**Figure 1-2**). To extract and analyze the multi-omics information behind the huge biomolecule network, it is important to preserve the original state of biomolecules and ensure their accessibility to probing. Here we summarize some trending tissue processing technologies that are currently applied to spatial omics analysis, and reveal their chemical mechanisms (**Figure 1-3**).

In the history of the development of histology, aldehyde fixation is the most popular and widely accepted option. Aldehyde reagents, such as paraformaldehyde and glutaraldehyde, are still frequently used by most of the researchers due to the simplicity and robustness of aldehyde fixation. In terms of the mechanism, aldehydes react with primary amines and thiols from the biomolecules, and subsequently forms methylene bridges with less reactive groups, such as primary amides and guanidine groups. Specifically, aldehyde fixation can effectively preserve nucleic acids with adenosine and cytidine nucleotides, proteins or peptides with lysine and cysteine residues, and metabolites with free primary amine groups. Apart from aldehyde fixation, chemicals with epoxide groups are also candidates for preserving biomolecules that have primary amines. The epoxide ring can be opened by amine groups to generate an amino alcohol. For example, Park et al. reported their success in preserving protein fluorescence, protein immunoreactivity, and nucleic acids with a polyfunctional, flexible epoxide[3].

In contrast to the chemical crosslinking of biomolecules, non-fixation method is a better option in the cases where less modification is favored in particular. After dissection, tissues can be immediately frozen and sectioned without any fixation step. Therefore, the physiological state of biomolecules can be snapshotted and preserved as much as possible. In the cases of some in situ capturing based spatial transcriptomics[4,5], where the transfer of endogenous mRNA from the tissue to the barcoded matrix occurs, and the cases of some imaging mass spectrometry based spatial metabolomics[6,7], where the desorption and mass spec measurement of metabolites occurs, frozen sections or very lightly fixed tissues are chosen because of their lower level of chemical modification. Despite the advantages, tissues processed through non-fixation methods have poor mechanical stability and limited scalability to volumetric sampling.

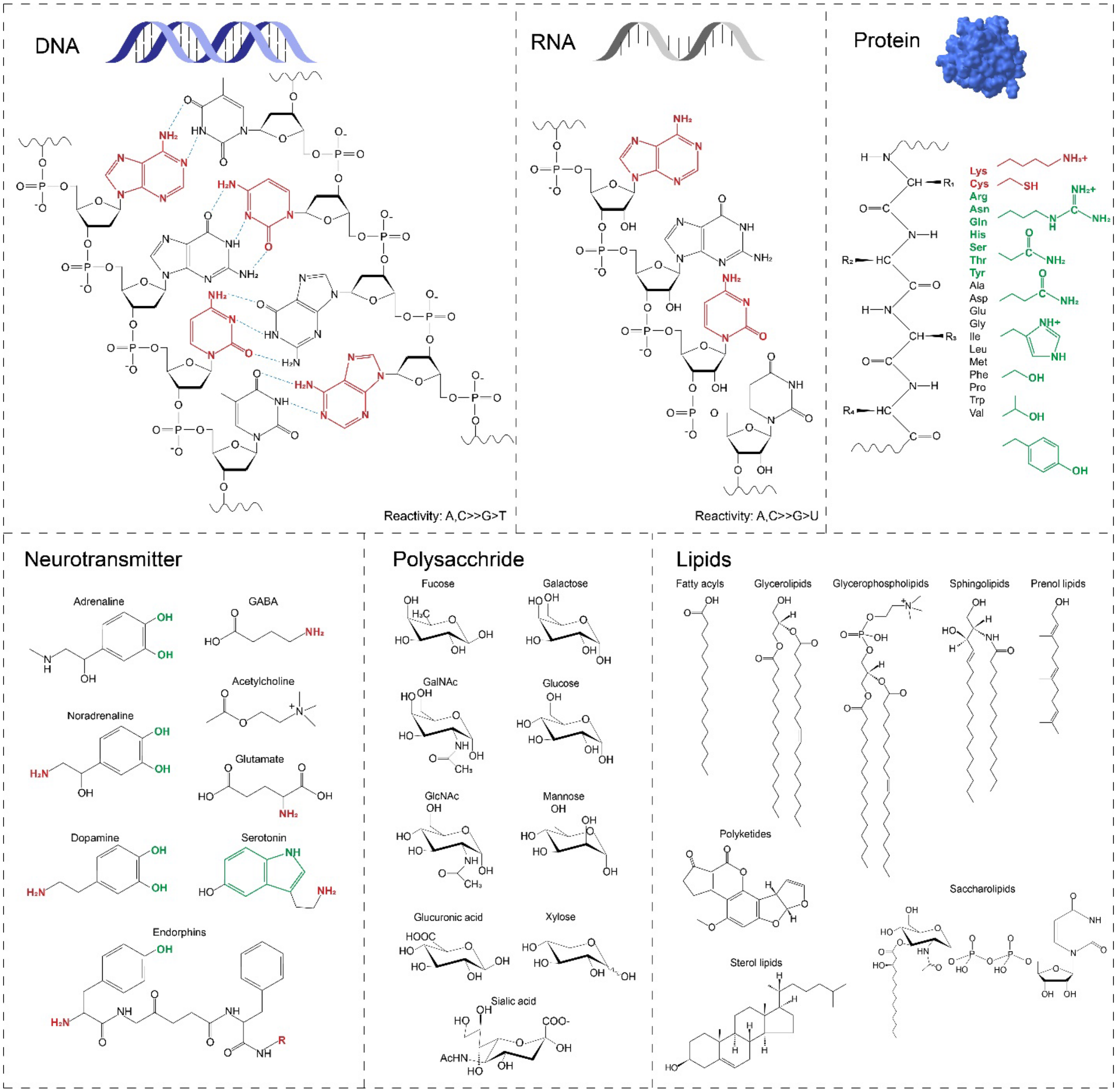

Figure 1-2. Chemical structures of major categories of biomolecules in brain. Functional groups that can be directly modified through aldehyde fixation chemistry are labeled red. Functional groups that can be crosslinked by methylene bridges are labeled green.

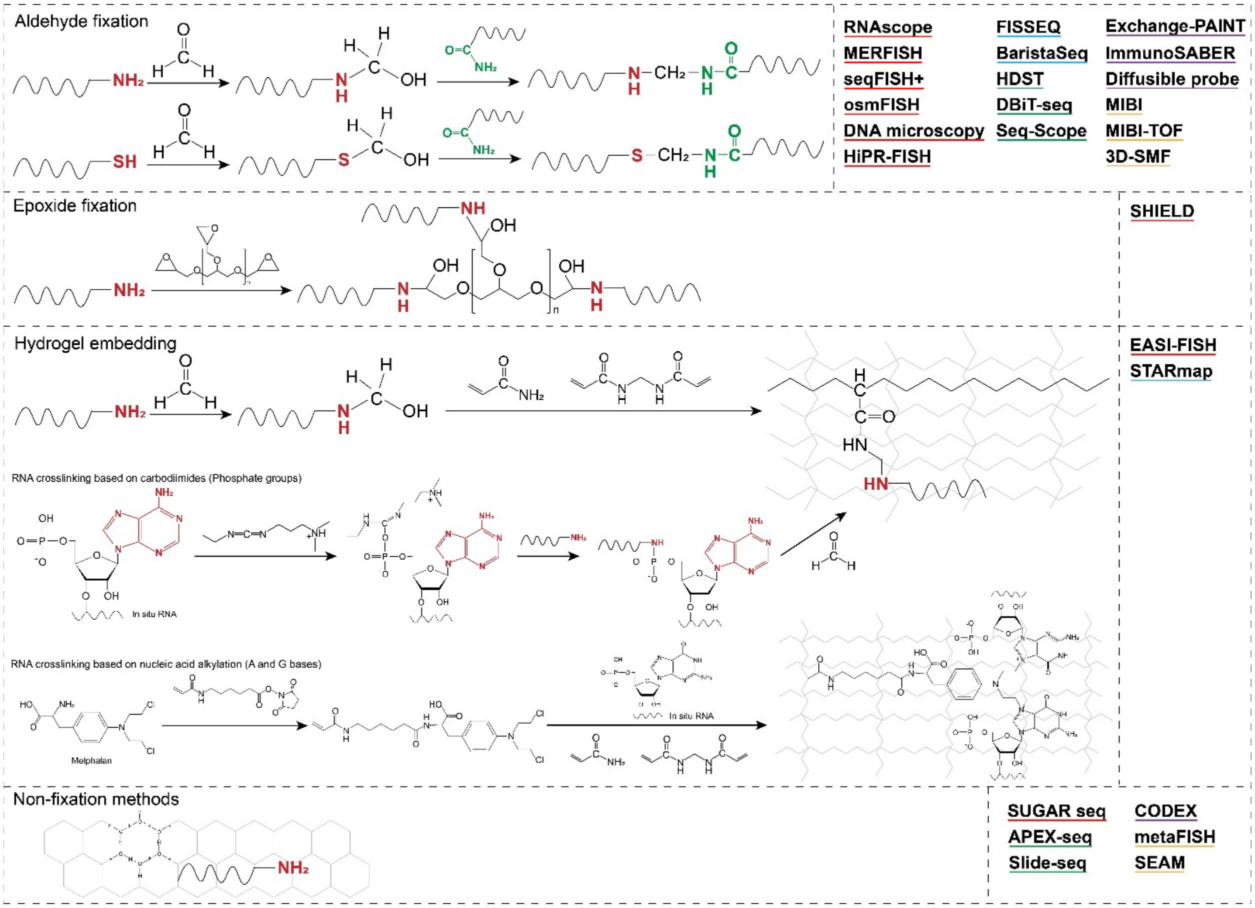

Figure 1-3. Chemical mechanisms of tissue preservation techniques. Functional groups that can be directly modified through aldehyde fixation chemistry are labeled red. Functional groups that can be crosslinked by methylene bridges are labeled green. Representative spatial omics technologies that adopt each preservation method are noted on the right of the table.

1.3 Tissue hydrogel hybridization

Over the last decade, the development of optical tissue clearing methods and hydrogel-based tissue transformation technologies were developed for three dimensional molecular and cellular phenotyping of various tissues[8]. Through hydrogel embedding, tissues from various sources can be transformed into tissue-hydrogel matrix that is perfect for fluorescent labeling and imaging in terms of optical transparency, molecular permeability and mechanical stability. Paraformaldehyde fixation is involved in most of the hydrogel based tissue transformation technologies, serving as a bridge to chemically hybridize the biomolecules from tissue with synthetic hydrogel mesh (**Figure 1-3**). Amine and thiol containing biomolecules (e.g. proteins, nucleic acids, metabolites, etc.) covalently react with PFA to form hydroxymethyl groups. Methylene bridges are further generated between these biomolecules with hydroxymethyl groups and nearby amide groups, which is abundant in the solution full of acrylamide monomers. After the free radical initiation, a crosslinked mesh of polyacrylamide is synthesized in situ with biomolecules anchored to it. Tuning the concentrations of the compounds in the hydrogel varies the resultant physical properties; this includes permeability (pore size), mechanical toughness, and elasticity[8]. Such tissue hydrogel hybrid crosslinked by polyacrylamide mesh is able to effectively prevent the loss biomolecules, especially proteins, in the subsequent step of delipidation, but the preservation of the integrity of RNA turns out to be not as ideal as that of proteins. Therefore, multiple chemistries are supplemented to the system of tissue hydrogel hybrid for the preservation of the transcriptome (**Figure 1-3**). For example, carbodiimide compounds (e.g. EDC) are able to activate the phosphate group in RNAs, generating a highly reactive intermediate that can be crosslinked to neighboring amine groups[9]. Maleimide-and-isocyanate crosslinkers (e.g. PMPI) are able to react with 2’ hydroxyl group on the ribose, and crosslink it to neighboring thiol groups. Alkylating agents with multiple alkylating moieties (e.g. Melphalan) are able to react with adenosines and guanosines in RNAs, and further get incorporated into the hydrogel mesh[10]. In summary, different structural components of RNA molecules have been targeted and modified for the purpose of a better incorporation into the hydrogel mesh and thus a higher level of RNA retention.

1.4 Spatial omics and spatially resolved multi-omics

Since the success of smFISH, the importance of transcriptomic mapping has been well acknowledged, and an increasing number of platforms were developed for high throughput transcriptomic detection without losing spatial information, therefore known as “spatial transcriptomics”. Multiple approaches have been developed based on FISH related technologies to significantly increase the multiplexing capacity (**Figure 1-4 a**). The first category, in situ hybridization based spatial transcriptomics[10–16], introduces barcoding system to FISH probes. The molecular identity is determined by the combination of signals across multiple rounds of imaging, and can be decoded based on pre-defined barcode table. The second category, in situ sequencing based spatial transcriptomics[17–20], assigns a unique fragment of oligonucleotide to each probes. The unique sequence will be amplified and read out in situ through ligation or synthesis, reflecting the identity of the transcript it binds to. The third category, in situ capturing based spatial transcriptomics[4,5,21–24], transfers the endogenous transcripts from tissues to a spatially barcoded matrix. The identity of transcripts can be correlated to their spatial coordinates based on the subsequent sequencing of the subareas of the matrix.

At the same time, the idea of barcoding with oligonucleotide was also adapted in the field of spatial proteomics. In antibody-oligo based spatial proteomics, fragments of oligonucleotide carrying the information of the antigen are conjugated to antibodies[25–28]. Since such antibody-oligo conjugates can be visualized through multiple DNA based signal amplification methods, the limitations of host species matching brought by indirect immunofluorescence can be mitigated.

Specialized to sensitively detecting changed molecules, imaging mass spectrometry[29] emerged as a powerful alternative to all of the technologies based on fluorescent imaging. Without the restriction of fluorescence spectral overlap, imaging mass spectrometry is naturally more suitable for spatially mapping biomolecules in a highly multiplexed manner. So far, there have been attempts from the field of spatial proteomics and spatial metabolomics that take advantage of the potential of the high multiplexing capacity of imaging mass spectrometry[6,7,30,31]. Metal isotopes can be conjugated to antibodies to generate unique signal for mass spectrometry readings, whereas multiple types of metabolites (lipid fragments, neurotransmitters, glycans, etc.) can be directly captured based on the signal of their ions.

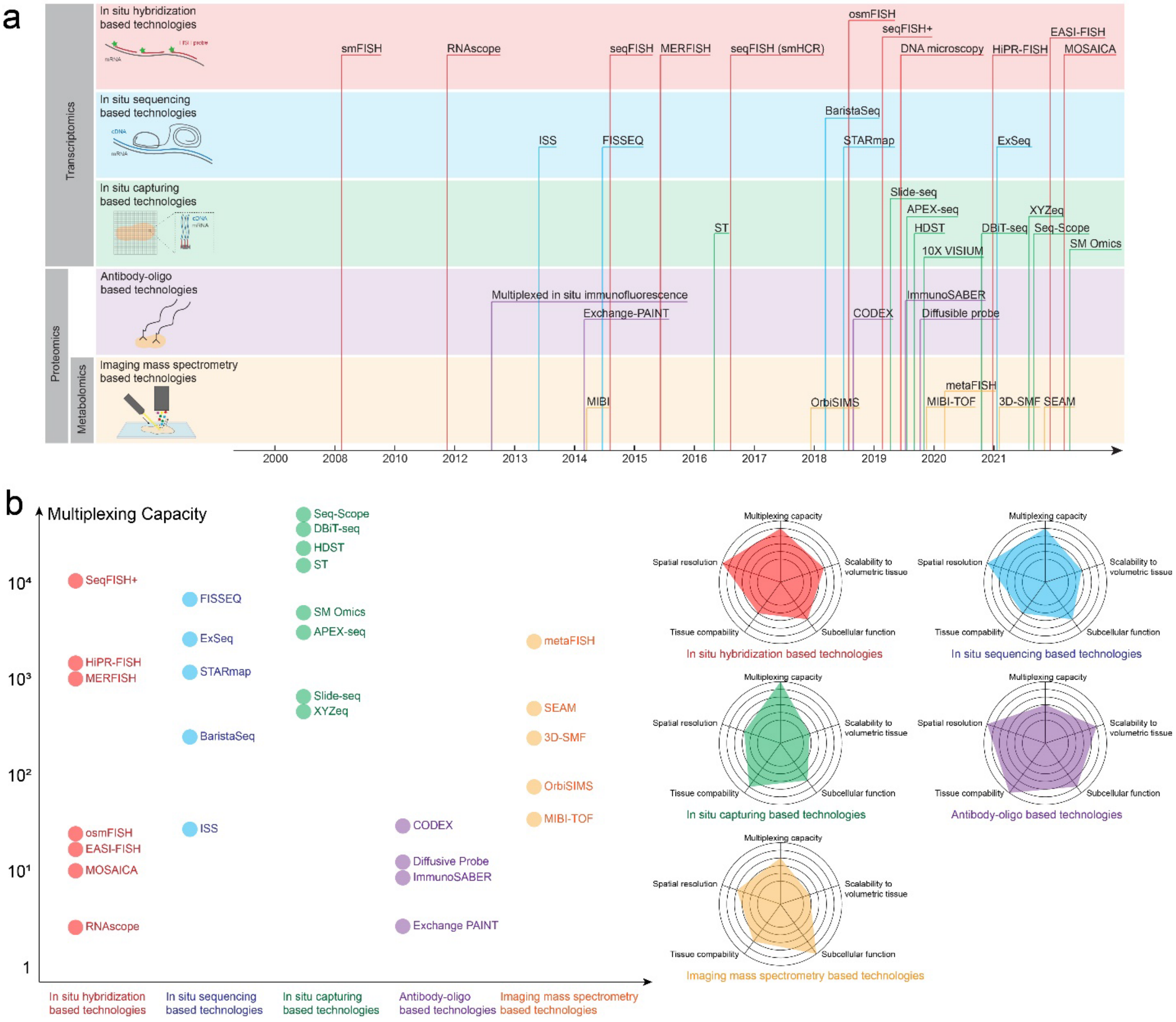

Figure 1-4. Timeline and multiplexing scalability of spatial omics technologies. (**a**) Timeline of the development of spatial omics technologies. (**b**) Comparative analysis of the advantages of spatial omics technologies.

1.5 Combinatorial barcoding strategy and multiplexing capacity

In order to characterize complex biological tissues systematically and efficiently, methods that are scalable to large number of target biomolecules are preferable. **Figure 1-4 b** illustrates the multiplexing scalability of the aforementioned categories of spatial omics technologies. In situ hybridization based methods can be divided between schemes that implement serial target detection and those that implement combinatorial barcoding methods. Methods such as osmFISH[14] and EASI-FISH[10] use cycles of repeated probe hybridization and stripping to detect targets; and have been applied in tissue sections several hundred microns thick. However, their linear nature limits time efficiency, and so they have only been used to detect a comparatively modest number of genes (less than 50). Combinatorial barcoding strategies increase multiplexing capacity to thousands (merFISH[13]) or ten-thousand genes (seqFISH+[12]); yet these schemes are limited to thin tissue sections or single cells in the case of the latter.

In situ sequencing technologies also offer high multiplexing capacity, yet their scalability is somewhat more limited; these technologies have only been applied to tissues several micrometers thick. In situ capturing relies on high throughput next generation sequencing of transcripts, and thus has the highest multiplexing capacity of the three branches of transcript detection. Capturing methods also require minimal chemical modification of the sample, compared to the other two categories (which require processes such as specialized RNA fixation or hydrogel embedding). Conversely, spatial resolution is more limited than in situ hybridization and sequencing.

Antibody-oligo hybridization schemes score highly on spatial and subcellular resolution, have been successfully scaled to tissue sections on the millimeter thickness, and are applicable to a wide spectrum of tissue fixation methods. So far, their multiplexing capacity has been modest, only comparable to serial target detection methods for FISH. Finally, mass-spectrometry provides excellent insight into subcellular metabolic function, despite only ranking moderately in multiplexing, scalability, and spatial resolution.

Aside from barcoding biomolecules with combinatorial barcoding strategy, another possible approach to increase the multiplexing capacity with limited number of fluorescent channels is to combinatorially barcode fluorescent channels/dyes. With CLASI-FISH[32], the spectrum of 6 individual fluorophores was distinguished into 15 channels by defining combinatorial channels with the combinations of two fluorophores. With iceFISH[33], 20 distinguishable pseudocolors were combined from 5 base colors, enabling the simultaneous characterization of gene expression and chromosome structure.

1.6 Alzheimer’s Disease

Alzheimer’s Disease (AD) is one of the most commonly diagnosed neurodegenerative disorders that features irreversible, progressive loss of brain functions with various levels of amnestic cognitive impairment, contributing to 60-80% of dementia cases[34]. It’s a slowly progressive disease which starts many years before any symptoms are manifested, and the duration of the development of cognitive symptoms varies individually based on age, genetics and sex. According to Alzheimer’s Association[35], the number of Americans living with Alzheimer’s Disease with age of 65 and above exceeds 6 million, and the same number is predicted to be about 13.8 million by 2060.

Alzheimer’s Disease is biologically defined by the presence of amyloid-beta-containing extracellular plaques and tau-containing intracellular neurofibrillary tangles[36]. Extracellular amyloid-beta plaques are widely found in most subregions of cerebral cortex. Derived from the cleavage of amyloid precursor protein (APP, a transmembrane protein enriched in synapses of neurons)[37], amyloid beta peptides are secreted into extracellular space as monomer, and exhibit high tendency to aggregate due to their peptide sequence. Aggregated amyloid beta oligomers exhibit neurotoxicity, impairing dendritic spines and synaptic efficiency. On the other hand, Tau is a microtubule-associated protein located in the cytoplasm of axons, and pre-synaptic and post-synaptic compartments, whose main function is to stabilize microtubules[38–40]. Different post translational modifications of Tau influence the way in which they are internalized, processed or aggregated. In the scenario of Alzheimer’s disease, aggregated Tau proteins can be observed in the forms of neurofibrillary tangles, neuropil threads, and dystrophic neurites, as an indicator of cognitive deficit.

1.7 Protein functional detection

Another important aspect of proteomics which was neglected by existing technologies is protein functionality. As the participants of various biological processes, proteins and other small biomolecules (glycans, neurotransmitters, lipids, etc.) carry out most functionality necessary for cells, and therefore contain much more functionality information than their spatial distribution only. For example, in the field of cancer diagnostics, the dysregulation of protease activity is considered to be an important hallmark and a potential therapeutic target of cancer. Activity-based diagnostics and therapeutics have shown promising results[41], however, there has been limitations on systematically designing probes due to the absence of approaches to visualize protease activity directly within the tissue context.

Current IHC or imaging mass spectrometry are able to reveal the spatial location of proteins, but not a direct reflection of their functions. In practice, almost all spatial proteomics technologies require chemical fixation to permanently preserve proteins, where functional detection of proteins is not possible due to inability to undergo protein conformational change and chemical modification of binding sites (**Figure 1-5**). Therefore, a new tissue preservation technology should be incorporated into the current scheme of spatial omic platforms enabling functional detection.

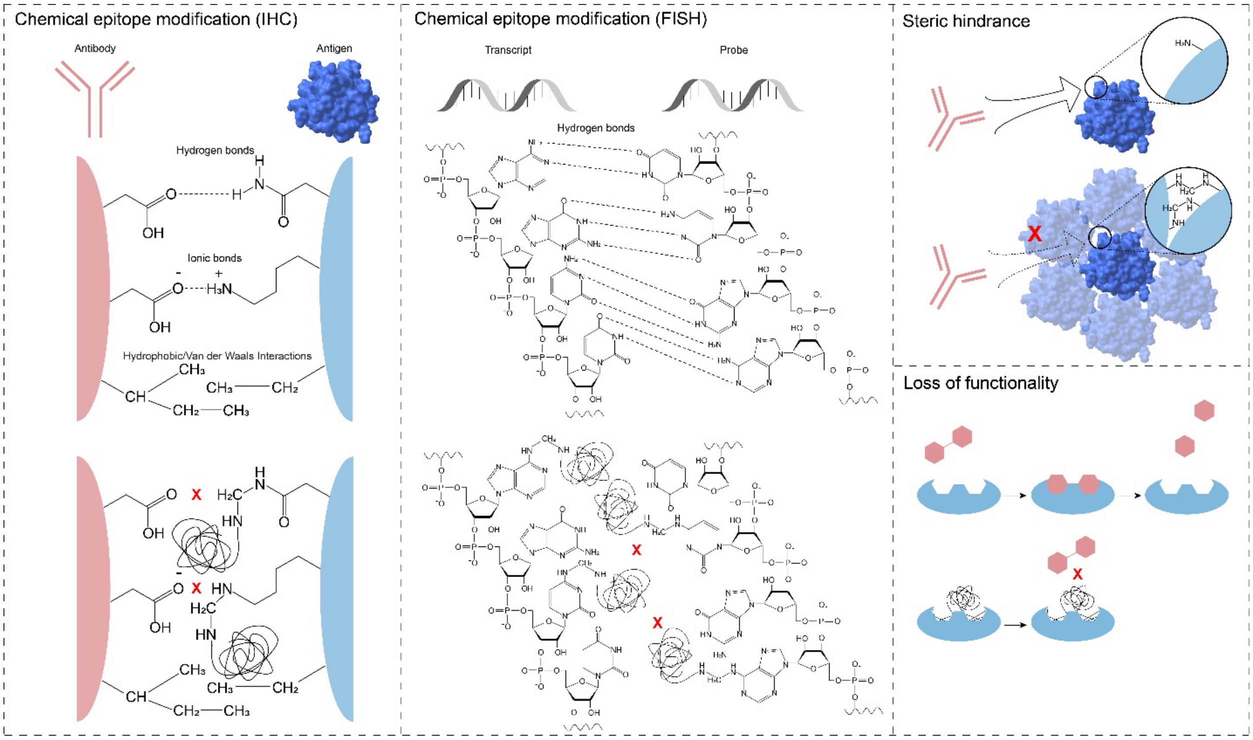

Figure 1-5. Potential limitations of spatial omic platforms due to chemical fixation.

1.8 Thesis aims

Aim 1: Develop computational models of the modulation of antibody binding kinetics for controlled delivery

Although spatial proteomics serves as a powerful tool for interrogating protein networks, its widespread application is often hindered by the limited volumetric scalability and multiplexing capability inherent in the methods of current platforms. As the first step to develop our spatial proteomic platform, we aim to perform theoretical investigation of the optimal mode for 3D proteomic mapping. To specifically address existing limitations, we aim to build computation models to simulate the reaction-diffusion process of probes, and to further design multiple antibody labeling modulations for better volumetric and multiplexing scalability.

Aim 2: Validate different model-inspired spatial proteomic mapping modulations for enhanced volumetric and multiplexing scalability

In order to validate the predictions of our theoretical and computational models, and to practically implement the model-inspired modalities, we aim to design particular antibody labeling environments that satisfy the demands of volumetric and multiplexing scalability. We plan to experimentally facilitate the ideas with systems of DNA oligo conjugated antibodies, photo-stable imagers and optimized optical imaging techniques. With everything integrated as a pipeline, our goal is to demonstrate the spatial proteomic mapping in mouse brain with better volumetric scalability and multiplexing capacity.

Aim 3: Perform comparative cell profiling and pathological characterization of human brains diagnosed with Alzheimer's Disease with our spatial proteomic mapping platform

To showcase the performance of our spatial proteomic mapping platform, we performed proteomic characterization on human brain samples of Alzheimer’s Disease and control. We aim to conduct comparative characterization of cells, Alzheimer’s Disease related pathological hallmarks, and the spatial interactions between them. We expect some unique patterns on how Alzheimer’s Disease pathology affects patients’ brains could be revealed at cellular resolution enabled by our platform.

Aim 4: Develop mechanical interlocking based platform for 3D in situ protein functional detection

Proteins play a critical role in supporting cell structures, regulating biochemical reactions, and transducing signals in biological systems. Despite the fact that many spatial proteomic platforms enable mapping spatial distribution, few of them support in situ functional detection of proteins in 3D sample volumes. In this session, we aim to develop a method for 3D in situ protein functional detection, using mechanical interlocking of biomolecules by dense hydrogel meshes. Without chemical fixation, we expect that the functions of proteins (e.g. enzymatic activity) are preserved after the mechanical interlocking pipeline. Finally, we aim to demonstrate the potential of our method by spatially profiling protease activity in mouse colon tissues.

Chapter 2. Theoretical study and computational modeling of multiple spatial proteomics modalities enabled by antibody binding kinetics modulation

2.1 Introduction

Characterization of cellular and molecular landscapes in their cognate spatial context is key to advance our understanding of complex biological systems. Leveraging advances in imaging and molecular profiling tools, the field of spatial omics has developed rapidly, with emerging technologies designed to capture different biomolecules at different scales. Due to its multiplexing scalability, spatial transcriptomics via a variety of *in situ* RNA profiling technologies[5,10,12–14,17–19,21,42], is redefining the way tissues are studied by providing an unprecedented insight into transcriptional activity and its association to tissue architecture and functionality. However, multiple aspects of protein expression and regulation (post-transcriptional, translational, chemical modifications, subcellular localization, etc.), which are not fully reflected by transcriptomic analysis, limit RNA-based inferences to predictions about the dynamics and the function of their corresponding protein counterparts. To address this need, several spatial proteomics technologies have been developed to directly depict the protein landscape within tissues[26–29,43–45].

While current spatial proteomics have enabled unique insights into the relationship between tissue architecture and protein distribution and dynamics, their applications have been focused on ultra-thin (<40 um thick) tissue sections and have displayed limited multiplexity compared to spatial transcriptomics. In spatial transcriptomic techniques, combinatorically barcoded labeling can achieve exponential growth in multiplexity (e.g., MERFISH: 2^H-1, seqFISH: R^H, R-number of reporters; H-number of hybridization rounds).

In contrast, compared to mRNAs, proteins pose inherent challenges for barcoding-based approaches due to their significantly higher expression levels and greater abundance variability[46,47]. The high expression levels of proteins render standard diffraction-limited fluorescent microscopy incapable of resolving individual proteins or protein complexes as single molecule dots, making combinatorial barcoding strategies inapplicable (**Figure 2-1**). Consequently, in current spatial proteomics platforms utilizing barcoded antibodies, the multiplexing capacity scales linearly, due to sequential imaging scheme (R x H)[48]. Furthermore, existing spatial proteomic platforms are constrained to ultra-thin sections due to the difficulties in uniformly labeling thick tissue with a large library of barcoded antibodies, attributed to the high expression levels of proteins and their copy number variabilities. Therefore, scaling of volumetric applicability and multiplexing capacity in spatial proteomics remains an unmet need to fully unlock the potential of spatial proteomic characterization.

To overcome this challenge, here we introduce a robust, easy to implement, 3D proteomic mapping platform with both volumetric and multiplexing scalability. Using theoretical study and computational modeling, we predicted that slowing down the kinetics of the antibody-antigen binding reaction while maintaining high antibody-antigen binding equilibrium results in uniform volumetric labeling of thick tissue with highly controllable labeling density. In this unique condition, a simple modulation of the amount of antibody that’s used in the reaction can control labeling density tissue-wide. Here we showcase two modalities for 3D proteomics analysis with our platform: dense labeling and stochastic sparse labelling (**Figure 2-2**).

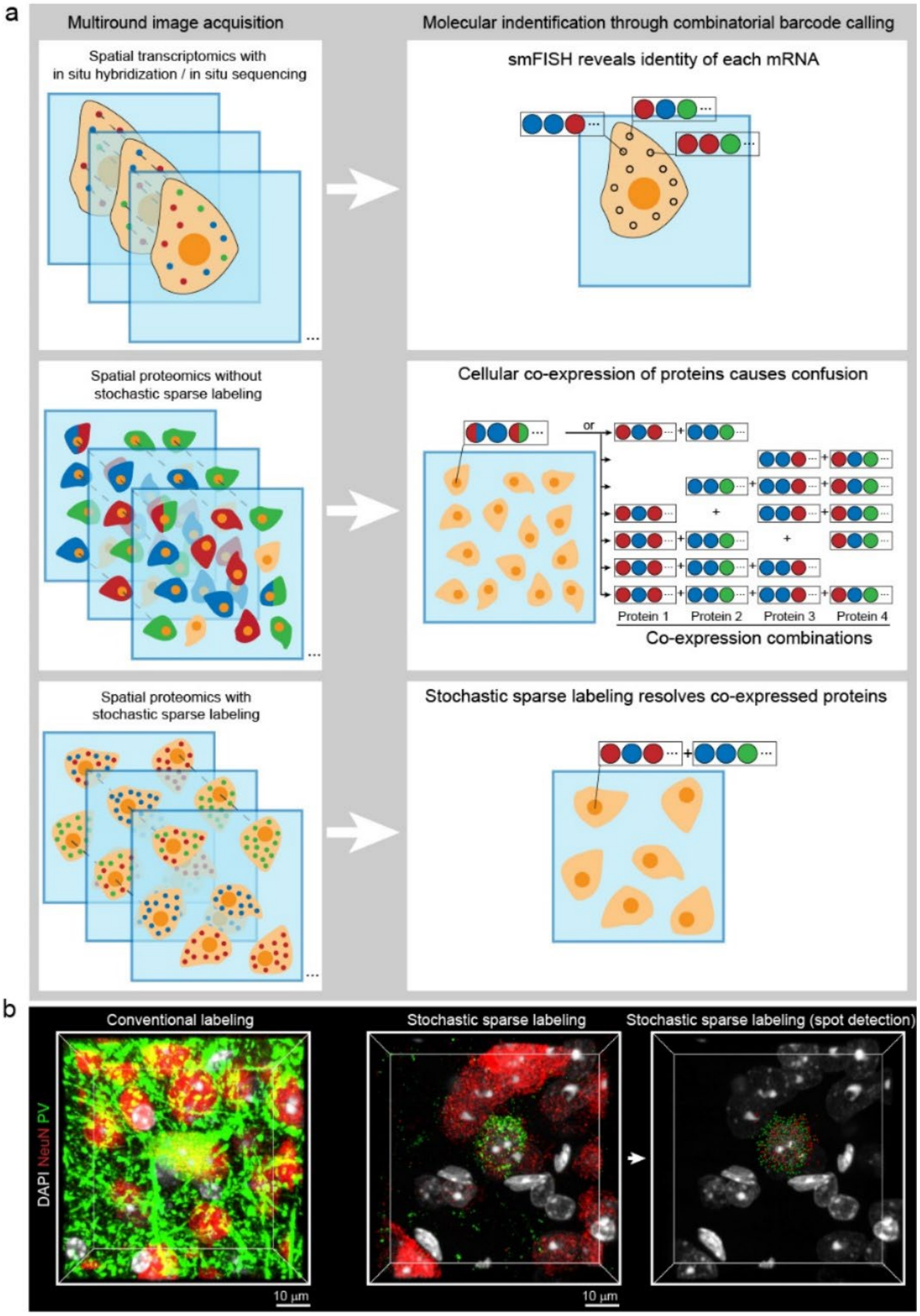

Figure 2-1. Modalities of molecular identification with and without combinatorial barcode calling. (**a**) Typical methods of molecular identification adapted by spatial transcriptomics and spatial proteomics. For spatial proteomics without stochastic sparse labeling, combinatorial barcoding strategy cannot be applied for enhanced multiplexing capacity due to the confusion of protein co-expression. (**b**) An example of protein co-expression (NeuN, PV) in the same cell. Stochastic sparse labeling is necessary to resolve respective patterns of NeuN and PV to avoid confusion.

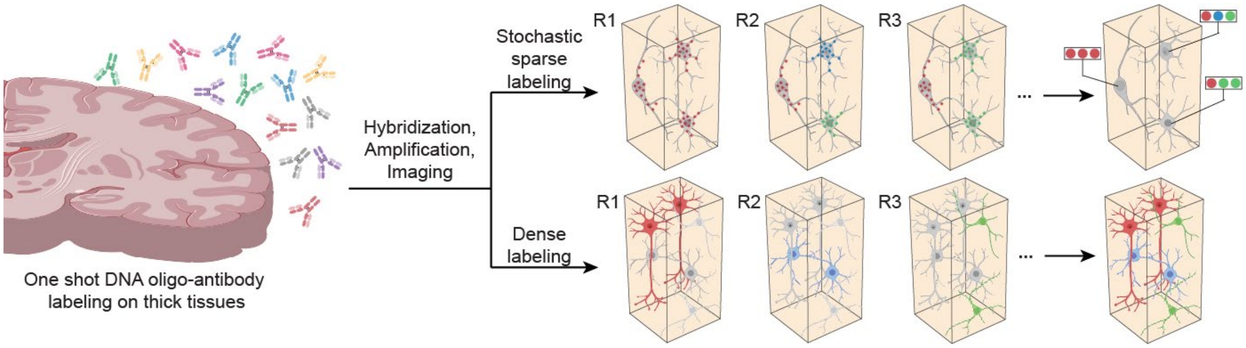

Figure 2-2. Overview of the workflow of spatial proteomic mapping platform, and the labeling modalities. Two labeling modalities facilitated with spatial proteomic mapping platform. Tissues are labeled with all relevant DNA-oligo conjugated antibodies in one shot. The density of labeling is controlled by adjusting the amount of antibodies: stochastic sparse labeling for implementation of combinatorial protein barcoding strategies, or dense labeling for better presenting tissue architecture and cellular morphology.

2.2 Results

2.2.1 Theoretical analysis of the reaction-diffusion process of antibody

To determine the labeling conditions required to establish a 3D spatial proteomic platform with uniform staining a theoretical study of the forces affecting labeling distribution was performed. We started by modeling the binding between unbound antigen (Ag) and unbound antibody (Ab) as a reversible reaction that generates antibody-antigen complex (C)[49], $\mathrm{Ag} + n\mathrm{Ab} \rightleftharpoons \mathrm{C}$, where n is the average number of bound antibodies per antigen. Dynamically in this system, the forward reaction has an association rate constant k_{f}, which is directly associated to the speed of antibody binding kinetics, and the reverse reaction has a dissociation constant k_{r}, with which an equilibrium constant can be expressed as $K_{\mathrm{cq}} = \frac{k_{\mathrm{f}}}{k_{\mathrm{r}}}$. For specific and robust labelling, it is critical to maintain a high ratio for this parameter.

If we assume the reaction orders of unbound antigen, antibody and complex are m_1, m_2, and m_3, and both forward and reverse reactions follow differential rate laws, the system can be described using a classic mass conservation equation (1). In this framework the variation in concentration of species in the system can be explained by three contributing factors (equation terms): convection ($\boldsymbol{v} \cdot \nabla C_i$), diffusion ($D_i \nabla^2 C_i$), and reaction ($R_i$) respectively. Due to intrinsic properties of biological tissues and chemical fixation[50–52], convection and diffusion for antigen and antibody-antigen complex can be neglected, yielding a set of simplified equations (2–4) describing the behavior of the species in the system.

$$\frac{\partial C_i}{\partial t} = -v \cdot \nabla C_i + D_i \nabla^2 C_i + R_i \tag{1}$$

$$\frac{\partial [\mathrm{Ag}](z,t)}{\partial t} = -\Big(k_{\mathrm{f}}([\mathrm{Ag}](z,t))^{m_1}([\mathrm{Ab}](z,t))^{m_2} - k_{\mathrm{r}}([\mathrm{C}](z,t))^{m_3} \Big) \tag{2}$$

$$\frac{\partial [\mathrm{Ab}](z,t)}{\partial t} = D \frac{\partial^2 [\mathrm{Ab}](z,t)}{\partial z^2} - n\Big(k_{\mathrm{f}}([\mathrm{Ag}](z,t))^{m_1}([\mathrm{Ab}](z,t))^{m_2} - k_{\mathrm{r}}([\mathrm{C}](z,t))^{m_3} \Big) \tag{3}$$

$$\frac{\partial [\mathrm{C}](z,t)}{\partial t} = k_{\mathrm{f}}([\mathrm{Ag}](z,t))^{m_1}([\mathrm{Ab}](z,t))^{m_2} - k_{\mathrm{r}}([\mathrm{C}](z,t))^{m_3} \tag{4}$$

Since Ag is chemically fixed in place, uniform labelling, which corresponds to an even distribution of C in z, can only be experimentally manipulated by controlling the diffusion and binding of Ab. Therefore, focusing on Ab distribution, we consider that following finite time (T) incubation, the reaction-diffusion system approaches its equilibrium, where, $\left.\frac{\partial [\mathrm{Ag}](z,t)}{\partial t}\right|_{\mathrm{t=T}} \approx 0,\ \left.\frac{\partial [\mathrm{Ab}](z,t)}{\partial t}\right|_{\mathrm{t=T}} \approx 0,\ \left.\frac{\partial [\mathrm{C}](z,t)}{\partial t}\right|_{\mathrm{t=T}} \approx 0$. In this regime, equation (3) can be solved as shown in (5).

$$\frac{d^2[\mathrm{Ab}](z,\mathrm{T})}{dz^2} - \frac{nk_{\mathrm{f}}}{D}\left(([\mathrm{Ag}](z,\mathrm{T}))^{m_1}([\mathrm{Ab}](z,\mathrm{T}))^{m_2} - \frac{1}{K_{\mathrm{eq}}}([\mathrm{C}](z,\mathrm{T}))^{m_3} \right) = 0 \tag{5}$$

Based on what we consider common experimental conditions, where (i) total antigen concentration is much higher than initial antibody concentration, resulting in the majority of antigen remain unsaturated at equilibrium $[\mathrm{Ag}](z,\mathrm{T}) \approx [\mathrm{Ag}]_0$ and (ii) the requirement that equilibrium constant (K_{eq}) for the binding reaction is sufficiently large to ensure specific labeling, we can neglect the reverse reaction in the reaction term. Equation (5) can be further simplified to produce a general governing equation (6), whose solutions can be specified by geometric and experimental boundary conditions, such as a tissue slab that is symmetric with respect to middle plane with given total amounts of Ab.

$$\frac{d^2[\mathrm{Ab}](z,\mathrm{T})}{dz^2} - \frac{nk_{\mathrm{f}}}{D}[\mathrm{Ag}]_0^{\ m_1}([\mathrm{Ab}](z,\mathrm{T}))^{m_2} = 0 \tag{6}$$

$$\text{Boundary Conditions:} \quad \left.\frac{d[\mathrm{Ab}](z,\mathrm{T})}{dz}\right|_{z=\frac{\mathrm{Z}}{2}} = 0\ , \quad \int_0^{\mathrm{Z}} ([\mathrm{Ab}](z,\mathrm{T}) + n[\mathrm{C}](z,\mathrm{T}))\, dz = \mathrm{const.}$$

Inspection of equation (6) reveals that the distribution of unbound antibodies is determined by two independent parameters: the reaction order m_2, which is specific to the type of antibody and binding modality[53–55] and a lumped-in coefficient $\frac{nk_{\mathrm{f}}[\mathrm{Ag}]_0^{m_1}}{D}$, that aggregates factors including association rate constant for the forward reaction, initial antigen concentration and diffusion. Evaluating the uniformity of labeling across the combinations of these two parameters revealed that $\frac{nk_{\mathrm{f}}[\mathrm{Ag}]_0^{m_1}}{D}$ is the main contributing factor to the variation in labeling compared to reaction order (**Figure 2-3**). Among the parameters in the lumped-in coefficient, the antigen distribution and diffusion coefficient are dependent on biological properties of antigen and tissue on a case-by-case basis. Therefore, we proposed that decreasing k_{f} of antibody binding reaction, while maintaining a high K_{eq} ratio is a universally applicable strategy to achieve uniform antibody labeling in thick tissues. Notably, decreasing k_{f} also shift the systems towards conditions where the reaction order has a negligible effect on labelling uniformity, which suggest this approach is extendable to different types of antibodies and binding modalities.

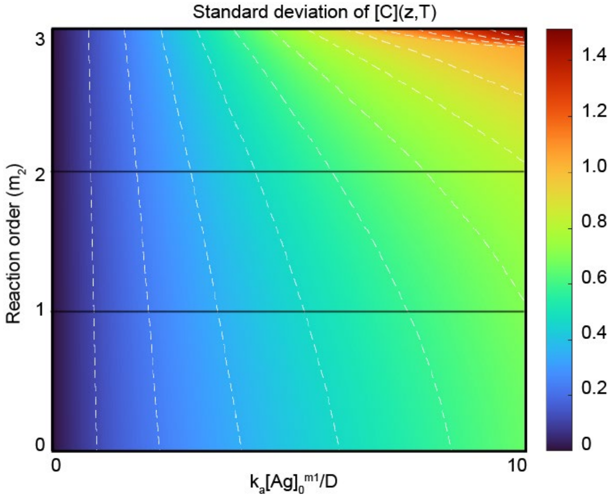

Figure 2-3. Standard deviations of antibody labeling profile with respect to different combinations of kinetics and binding reaction order.

2.2.2 Computational modeling of spatial proteomics modalities

Using this mathematical framework, the issues with labeling uniformity observed when conventional labeling conditions are applied to thick tissues[56–62] can easily be evaluated. Since conventional methods have been optimized for thin slices where volumetric uniformity is not a concern, they generally feature high k_{f}, which can be described as fast kinetics for the antigen-antibody binding reaction (**Figure 2-4 a, b**, case 1). These conditions are not compatible with thick tissues, as antibodies are rapidly depleted before reaching inner regions. However, slowing down the binding kinetics (lowering k_{f}) while maintaining high equilibrium constant K_{eq} results in conditions where the antibodies are effectively dispersed uniformly across tissues with no loss on specificity (**Figure 2-4 a, b**, case 3 and 4). In particular, the initial antibody concentration becomes the determinant for labeling density and can be used as a modulator independent of the expression level of antigens.

The ability to modulate the labeling density has profound implications in the type of proteomic imaging applications that can be pursued using a large library of barcoded antibodies. Levering this capacity, two 3D spatial proteomic systems were developed: 1) uniform, dense protein labeling (**Figure 2-4 b**, case 3); and 2) uniform, stochastic sparse protein labeling (**Figure 2-4 b**, case 4). When slow binding kinetics and high K_{eq} conditions are enforced, the dense labeling modality, facilitated by high initial antibody concentration, can be used for low magnification cell profiling, determination of tissue architecture or high magnification morphological evaluation. Alternatively, stochastic sparse labeling, with a decreased initial antibody concentration, can be used to transform clustered protein signal into sparse, resolvable pattern, enabling the implementation of combinatorial protein barcoding.

The ability to modulate the labeling density uniformly in thick tissue solely by adjusting the quantity of antibody used holds significant implications for proteomic imaging applications. Irrespective of the high expression levels of proteins and their copy number variations, we can achieve uniform labeling of thick tissue with a large library of barcoded antibodies, enabling scaling spatial proteomics to thick 3D volume. Moreover, by modulating labeling density to a degree where standard diffraction-limited fluorescent microscopy can resolve individual proteins or protein complexes as single molecule dots, combinatorial barcoding strategies become applicable. Levering this capacity, two distinct 3D spatial proteomic systems were developed: 1) uniform, dense protein labeling (**Figure 2-4 b**, case 3); and 2) uniform, stochastic sparse protein labeling (**Figure 2-4 b**, case 4). The dense labeling modality, facilitated by high initial antibody concentration, can be used for low magnification cell profiling, determination of tissue architecture or high magnification morphological evaluation. Alternatively, stochastic sparse labeling, employing a low initial antibody concentration, can be used to transform clustered protein signal into sparse, resolvable pattern, enabling the implementation of combinatorial protein barcoding.

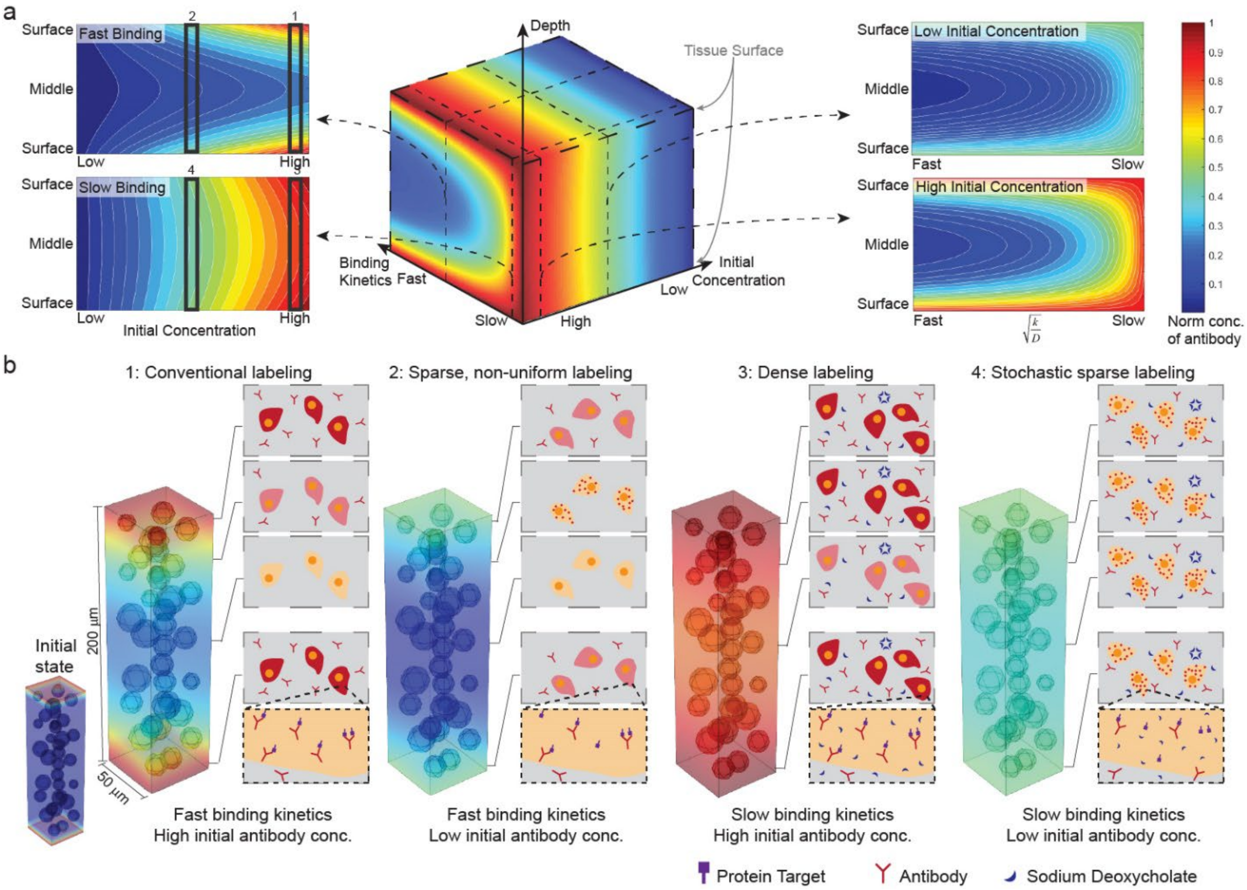

Figure 2-4. Computational modeling of the modalities facilitated by slowing down binding reaction kinetics. (**a**) The computational modeling of the antibody labeling process as a reaction-diffusion system. Slowed kinetics of antigen-antibody binding reaction ensures the uniformity of labeling, enabling the modulation of labeling density by varying initial antibody concentration. (**b**) Representative combinations of binding kinetics and initial antibody concentration result in different labeling patterns with pseudo tissue architecture. Case 1: conventional labeling conditions applied on ultra-thin slices. Rates of diffusion and reaction are not matched for volumetric scalability. Case 3,4: two labeling modalities applied in spatial proteomic mapping platform. Reduced binding reaction kinetics ensures labeling uniformity while varying labeling density.

2.2.3 Experimental evidence of the modulation of binding kinetics and labeling density

To experimentally implement the scalable 3D proteomic platform described above, an antibody conjugation strategy for improved multiplexity and a custom buffer system aimed to universally enforced slow antibody binding kinetics with high equilibrium constants were developed. To slow antigen binding reaction rate while maintaining high equilibrium constants, we developed a novel buffer system containing 1% sodium deoxycholate (NaDC) in Tris-glycine buffer adjusted to pH 9[63]. To demonstrate modulation of the kinetics of the antibody-antigen binding reaction, 200um-thick mouse brain slices were independently incubated with 8 primary antibodies commonly used in neuroscience studies (CB, ChAT, NeuN, NPY, PV, S100B, SST, VIP), for varying amounts of time (1hr, 3hr, 12hr or 24hr) in either Tris-glycine NaDC buffer or standard conditions (PBST) (**Figure 2-5 a and b**). For all cases, contrary to PBST where the signal intensity rose sharply and plateaued after 3hr, a steady increase throughout the entire incubation time was observed in the NaDC-containing buffer treatment. At 24h time point, the observed signal level was robust and had reached on average ~60% of the intensity observed in PBST, suggesting that the equilibrium constant remained relatively high. No differences were observed in cellular and subcellular signal distribution between treatments for all cases, indicating the labeling specificity was maintained. Together, these results confirmed both reduced binding kinetics and high equilibrium constant, the two critical features required to implement our proposed 3D spatial proteomic platforms.

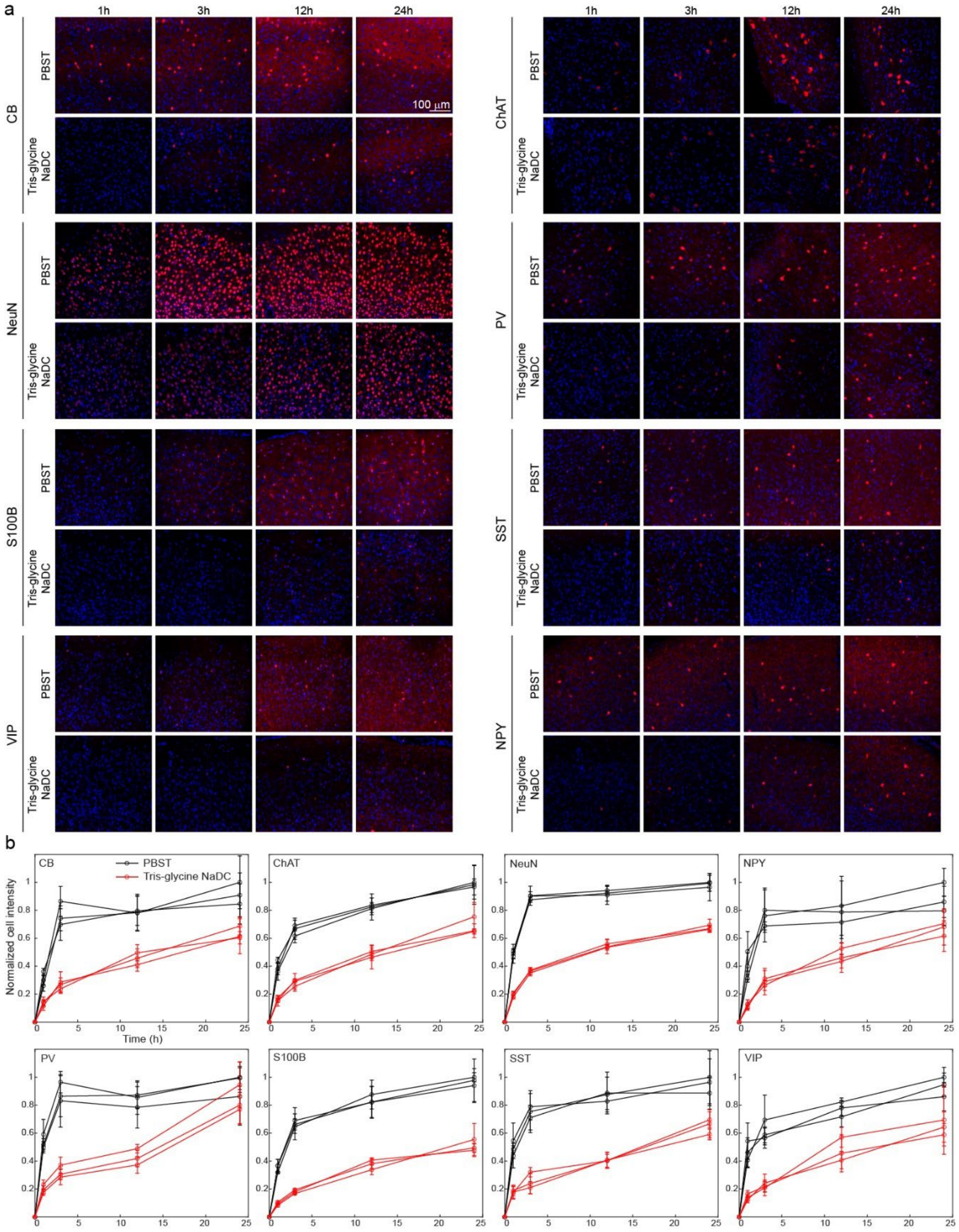

Figure 2-5. Experimental evidence of the effective reduction of binding reaction kinetics while maintaining high equilibrium constant. (**a**) Example images of commonly used antibodies. Each antibody was labeled in PBST and Tris-glycine NaDC conditions respectively for certain amount of time. (**b**) Measurements of the fluorescent intensity of labeled soma.

2.3 Methods

2.3.1 Theory of uniform labeling on thick tissues (first order reaction)

If we assume both forward and reverse reactions follow first-order differential rate laws, the system can be described using a classic mass conservation equation (1). Due to intrinsic properties of biological tissues and chemical fixation[50–52], convection and diffusion for antigen and antibody-antigen complex can be neglected, yielding a set of simplified equations (2–4) describing the behavior of the species in the system, where D is the diffusion coefficient of antibody in tissue.

$$\frac{\partial C_i}{\partial t} = -v \cdot \nabla C_i + D_i \nabla^2 C_i + R_i \tag{1}$$

$$\frac{\partial [\mathrm{Ag}](z,t)}{\partial t} = -\left(k_\mathrm{a}[\mathrm{Ag}](z,t)\,[\mathrm{Ab}](z,t) - k_\mathrm{d}[\mathrm{C}](z,t)\right) \tag{2}$$

$$\frac{\partial [\mathrm{Ab}](z,t)}{\partial t} = D\frac{\partial^2 [\mathrm{Ab}](z,t)}{\partial z^2} - \left(k_\mathrm{a}[\mathrm{Ag}](z,t)\,[\mathrm{Ab}](z,t) - k_\mathrm{d}[\mathrm{C}](z,t)\right) \tag{3}$$

$$\frac{\partial [\mathrm{C}](z,t)}{\partial t} = k_\mathrm{a}[\mathrm{Ag}](z,t)\,[\mathrm{Ab}](z,t) - k_\mathrm{d}[\mathrm{C}](z,t) \tag{4}$$

Focusing on the antibody distribution, we consider that the reaction-diffusion system approaches its equilibrium following finite incubation time (T), where $\left.\frac{\partial [\mathrm{Ag}](z,t)}{\partial t}\right|_{\mathrm{t=T}} \approx 0,\ \left.\frac{\partial [\mathrm{Ab}](z,t)}{\partial t}\right|_{\mathrm{t=T}} \approx 0,\ \left.\frac{\partial [\mathrm{C}](z,t)}{\partial t}\right|_{\mathrm{t=T}} \approx 0$. Based on what we consider common experimental conditions, where (i) total antigen concentration is much higher than initial antibody concentration, resulting in the majority of antigen remain unbound at equilibrium $[\mathrm{Ag}](z,\mathrm{T}) \approx [\mathrm{Ag}]_0$, and (ii) the equilibrium constant (K_eq) for the binding reaction is sufficiently large to ensure specific labeling, resulting in the neglection of the reverse reaction term, we can further simplify equation (3) to produce specific governing equation (5). With geometric and experimental boundary conditions, such as symmetry with respect to middle plane with given total amounts of Ab (m_0), the antibody distribution can be solved as in equation (6-7).

$$\frac{d^2[\mathrm{Ab}](z,\mathrm{T})}{dz^2} - \frac{k_\mathrm{a}[\mathrm{Ag}]_0}{D}[\mathrm{Ab}](z,\mathrm{T}) = 0 \tag{5}$$

$$\text{Boundary Conditions:} \quad \left.\frac{d[\mathrm{Ab}](z,\mathrm{T})}{dz}\right|_{z=0} = 0 \;, \quad \int_{-\frac{Z}{2}}^{\frac{Z}{2}} \left([\mathrm{Ab}](z,\mathrm{T}) + [\mathrm{C}](z,\mathrm{T}) \right) dz = m_0$$

$$\text{Solution:} \quad [\mathrm{Ab}](z,\mathrm{T}) = A \cosh\left(\sqrt{\frac{k_\mathrm{a}[\mathrm{Ag}]_0}{D}}\, z \right) \tag{6}$$

$$[\mathrm{C}](z,\mathrm{T}) = A K_\mathrm{eq}[\mathrm{Ag}]_0 \cosh\left(\sqrt{\frac{k_\mathrm{a}[\mathrm{Ag}]_0}{D}}\, z \right) \tag{7}$$

$$\text{where } A = \frac{m_0}{2\left(1 + K_\mathrm{eq}[\mathrm{Ag}]_0\right)} \sqrt{\frac{k_\mathrm{a}[\mathrm{Ag}]_0}{D}} \left(\sinh\left(\sqrt{\frac{k_\mathrm{a}[\mathrm{Ag}]_0}{D}}\, \frac{Z}{2} \right) \right)^{-1}$$

Inspection of the solution (7) reveals that the distribution of antibody-antigen complex is determined by parameters k_a, K_eq, $[\mathrm{Ag}]_0$, D. Among these parameters, the antigen distribution and diffusion coefficient are dependent on biological properties of antigen and tissue on a case-by-case basis. Focusing on k_a and K_eq, we evaluated and confirmed the negative correlation between association constant and the uniformity of labeling. In particular, the initial amount of antibody (m_0) becomes the only determinant for labeling density and can be used as a modulator independent of the expression level of antigens.

$$[\mathrm{C}](z,\mathrm{T}) = \frac{m_0}{2} \left(\frac{K_\mathrm{eq}[\mathrm{Ag}]_0}{1 + K_\mathrm{eq}[\mathrm{Ag}]_0} \right) \left(\frac{\sqrt{\frac{k_\mathrm{a}[\mathrm{Ag}]_0}{D}}}{\sinh\left(\sqrt{\frac{k_\mathrm{a}[\mathrm{Ag}]_0}{D}}\, \frac{Z}{2} \right)} \right) \cosh\left(\sqrt{\frac{k_\mathrm{a}[\mathrm{Ag}]_0}{D}}\, z \right)$$

$$\left(\frac{K_\mathrm{eq}[\mathrm{Ag}]_0}{1 + K_\mathrm{eq}[\mathrm{Ag}]_0} \right) \rightarrow 1 \quad \text{when } K_\mathrm{eq} \rightarrow \infty$$

$$\left(\frac{\sqrt{\frac{k_\mathrm{a}[\mathrm{Ag}]_0}{D}}}{\sinh\left(\sqrt{\frac{k_\mathrm{a}[\mathrm{Ag}]_0}{D}}\, \frac{Z}{2} \right)} \right) \rightarrow 1 \quad \text{when } k_\mathrm{a} \rightarrow 0$$

$$\cosh\left(\sqrt{\frac{k_\mathrm{a}[\mathrm{Ag}]_0}{D}}\, z \right) \rightarrow 1 \quad \text{when } k_\mathrm{a} \rightarrow 0$$

2.3.2 Computational simulation with COMSOL

The computational simulation of reaction-diffusion process of antibody was performed using COMSOL Multiphysics (COMSOL, Inc., Burlington, MA, USA). The reaction-diffusion of antibody was modeled using the physics of “Reacting Flow in Porous Media”. A representative volume with rectangular geometry between the top and bottom surfaces of the tissue was studied, and a set of spheres were drawn to represent cells with particular antigens. Inflow of the antibody was set to be through the top and bottom surface. The binding reaction of antibody and antigen was assumed to follow first order kinetics, and only occurred inside spheres. There was a 10-fold difference between the rate constants of the “Fast binding kinetics” and “Slow binding kinetics” conditions, and a 10-fold difference between the initial antibody concentrations of the “High initial concentration” and “Low initial concentration” conditions.

2.4 Conclusion and discussion

Leveraging principles of chemistry, mathematical modeling, and experimental validation using mouse and human brain tissues, we designed a theoretical model guiding us to tackle two important limitations in the field of spatial proteomics: limited scalability in 1) volumetric and 2) multiplexing capabilities. Labeling uniformity has not been a problem on ultra-thin sections where target proteins can be saturated[26,27], yet this strategy becomes cost-prohibitive and highly empirical when applied to volumetric analysis. In order to saturate proteins with high expression levels, an extremely large amount of antibodies would need to be used. Due to high variation in copy number and number of epitopes per antigen, even estimating the precise amount of antibodies necessary for saturation is a challenge, therefore not a broadly applicable solution. Instead, after detailed examination of the processes associated to probe and labelling distribution, we propose a clever solution to prevent antibody depletion by slowing down their binding kinetics, while maintaining a high binding equilibrium constant, allowing antibodies to diffuse across the tissue, resulting in specific and uniform volumetric labelling. While here we present data showing uniform labelling in up to 1mm thick tissues, we expect our method to be expandable to thicker tissues if the re-balancing between diffusion and binding reaction is maintained. In this regime, the only consideration is incubation time which increases with respect to the square of tissue thickness.

Evaluation of the modelling data in the regime where slow antibody binding kinetics and high equilibrium constant are enforced resulted in two additional insights: 1) labeling uniformity was minimally affected by binding reaction order, suggesting that this platform is extendable to various types of molecular probes, such as isotypes other than IgG, single domain antibodies, Fab fragments, bispecific antibodies, and various antibody conjugation chemistries; 2) the labeling density is tunable and depends only on the starting antibody amount.

Chapter 3. Model-inspired spatial proteomic mapping platform with enhanced volumetric and multiplexing scalability

3.1 Introduction

In order to systematically analyze the complex dynamic network of biomolecules, successive efforts have been devoted to technological advancement for biomolecular detection with higher precision, robustness and throughput. For example, the development and popularization of high throughput single cell / single nuclei RNA sequencing (scRNA-seq/snRNA-seq)[64–68] have revolutionized the way of cell type characterization by profiling their gene expression atlas. Then, able to simultaneously capture transcriptomic and spatial information, spatial transcriptomic technologies emerged as powerful tools for in situ mapping of RNA composition. In terms of multiplexing scalability, both single cell sequencing and spatial transcriptomics are able to detect above 10^4-10^5 genes/transcripts due to barcoding of nucleic acid signals. In particular, barcoded in situ RNA hybridization platforms (e.g., MERFISH, seqFISH+, osmFISH, EASI-FISH, etc.)[10,12–14], in situ RNA sequencing platforms (e.g., FISSEQ, BaristaSeq, STARmap, etc.)[17–19], as well as in situ RNA capturing platforms (e.g., Slide-seq, HDST, DBiT-seq, etc.)[5,21,22,42], adapted combinatorial barcoding strategy that significantly increases the throughput of RNA detection.

As a unique alternative to transcriptomic analysis, immunolabeling of proteins in situ has been a well acknowledged approach for cellular characterization. Compared with spatial transcriptomics, proteomic mapping provides unique information of protein expression, cellular functioning, connectivity and post-translational modification[69–71]. During the past decade, we and others have been developing new strategies to improve the multiplexing scalability of spatial proteomic detection (e.g., CODEX, ImmunoSABER, Diffusible probe, etc.)[26–28]. However, we still lack a spatial proteomic platform with the applicability on volumetric 3D tissues and compatibility to combinatorial barcoding strategy.

In the previous chapter, we introduced theory and computational model with detailed reasoning to modulate antibody binding kinetics. Here in this chapter, we develop an entire pipeline of spatial proteomic mapping platform guided by the principles involved in the modeling. We verified the volumetric scalability of protein labeling using a large number of barcoded antibodies in up to 1mm-thick brain tissues and provided evidence for tunable labeling density. Leveraging this capacity, we demonstrated the compatibility with combinatorial labelling methods for enhanced multiplexing scalability in 3D proteomic characterization.

3.2 Results

3.2.1 Preparation of DNA oligo conjugated antibody library via site-specific chemistry

To minimize interference with the antibody binding affinity, the conjugation of DNA oligos to primary antibodies was targeted to a limited number (~4 in most cases) of intramolecular disulfide bonds present at the junction of the Fc and Fab regions of the antibodies (**Figure 3-1**), as previously described[72]. Antibodies were modified by bis-alkylating reagent, bis-sulfone methyltetrazine, for the trans–cyclooctene–methyltetrazine (TCO-metet) ligation reaction. Using this strategy, a library of 46 conjugated antibodies targeting various cell type markers from different tissue sources was constructed and validated (**Figure 3-2**).

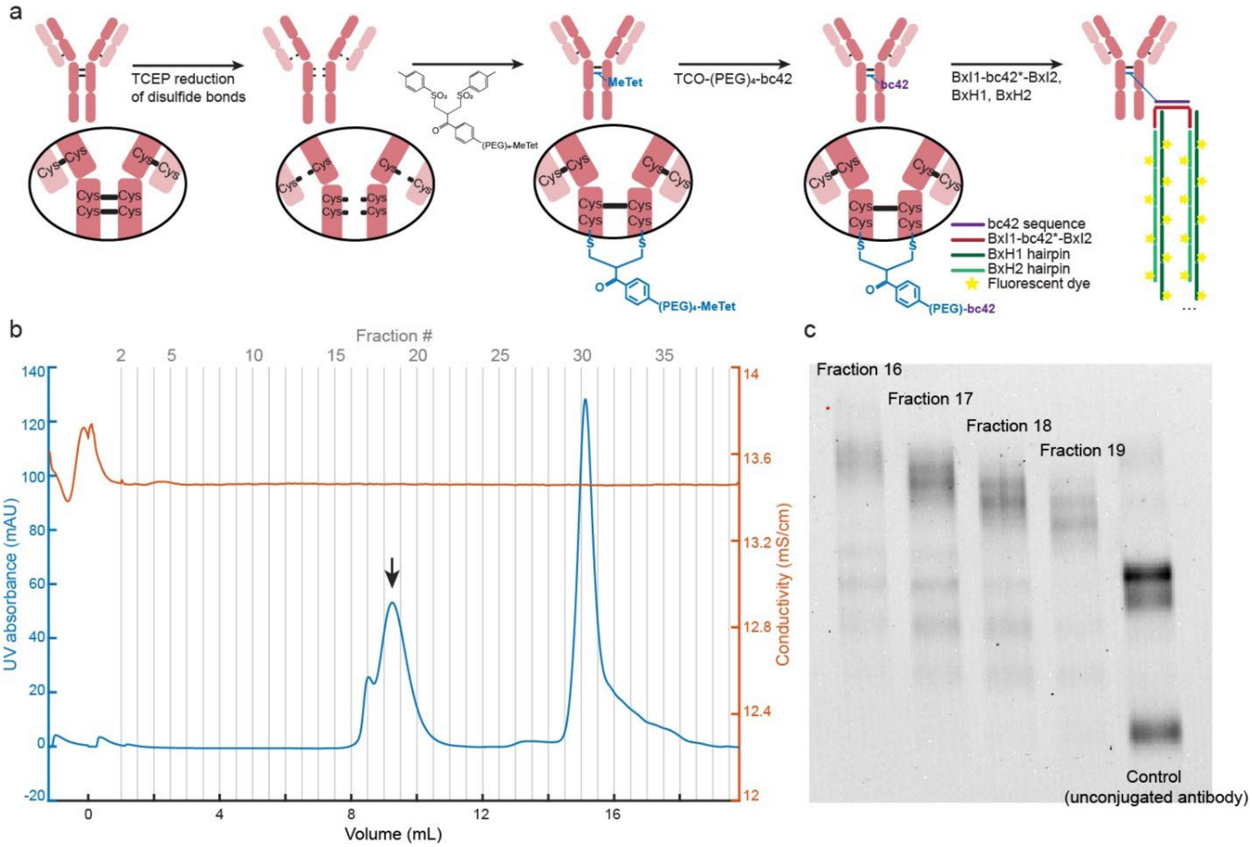

Figure 3-1. The workflow of covalently conjugating DNA oligomer to IgGs. (**a**) Disulfide bonds in antibodies are reduced, and subsequently modified by bis-sulfone-methyltetrazine. Antigen barcode (bc42) is labeled to the antibody through the rapid Click reaction between methyltetrazine and trans–cyclooctene (TCO). (**b**) Example of chromatogram from FPLC to purify DNA oligo conjugated antibody from the reaction mixture. The peak of conjugated antibody is pointed out by arrow. (**c**) SDS-PAGE of relevant fractions collected from FPLC.

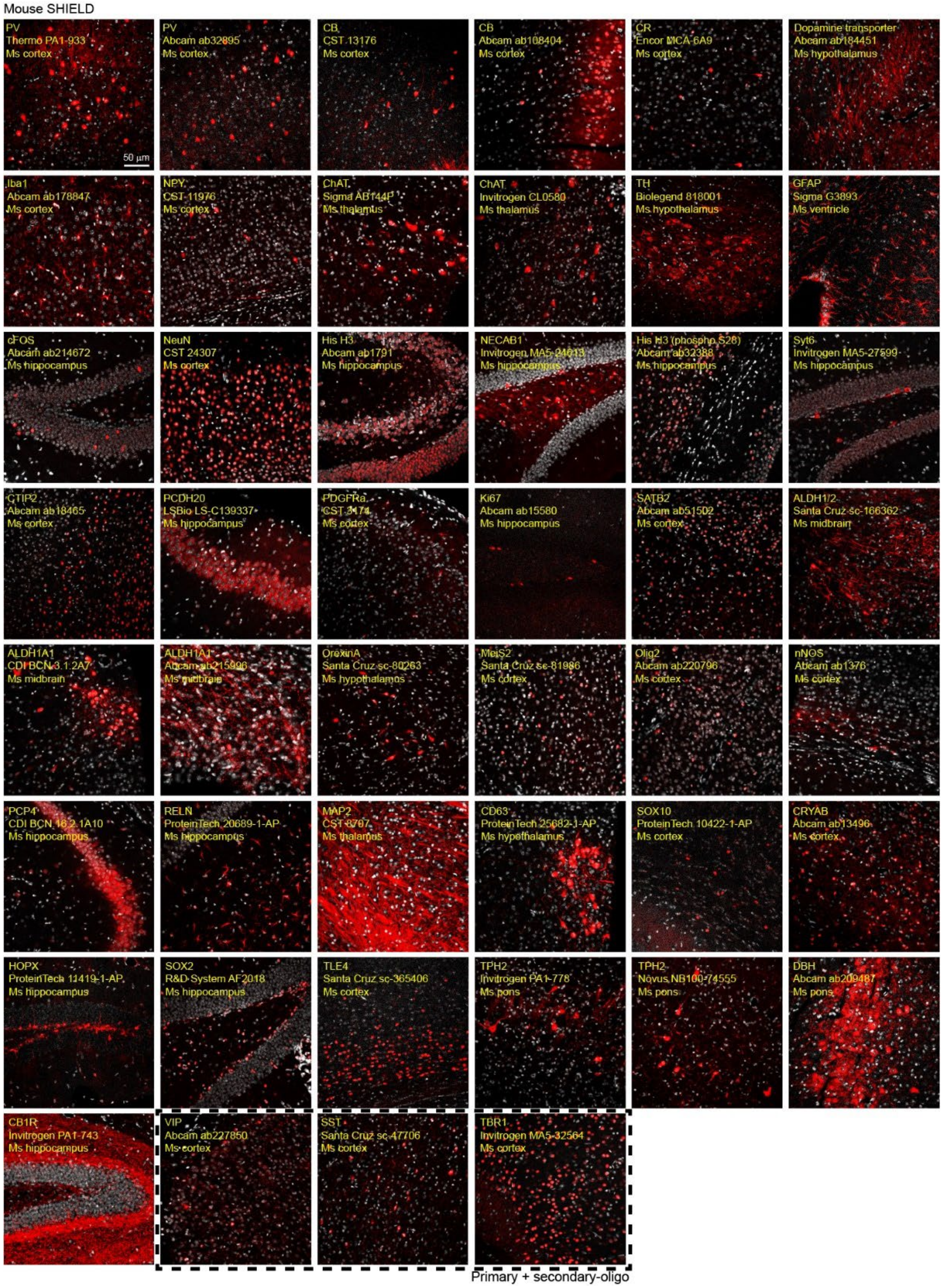

Figure 3-2. Representative staining images of DNA oligo conjugated antibodies of multiple sources of tissue. Corresponding tissue slices are labeled with barcoded antibodies, fixed, hybridized, and amplified by HCR. DAPI staining is conducted as counterstain (white). Images are acquired via confocal microscope (Leica TCS SP8 X) with 25x objective (Leica HCX IRAPO L 25x/0.95 W). Information of catalog of antibodies and tissue regions is listed on the top left of every image.

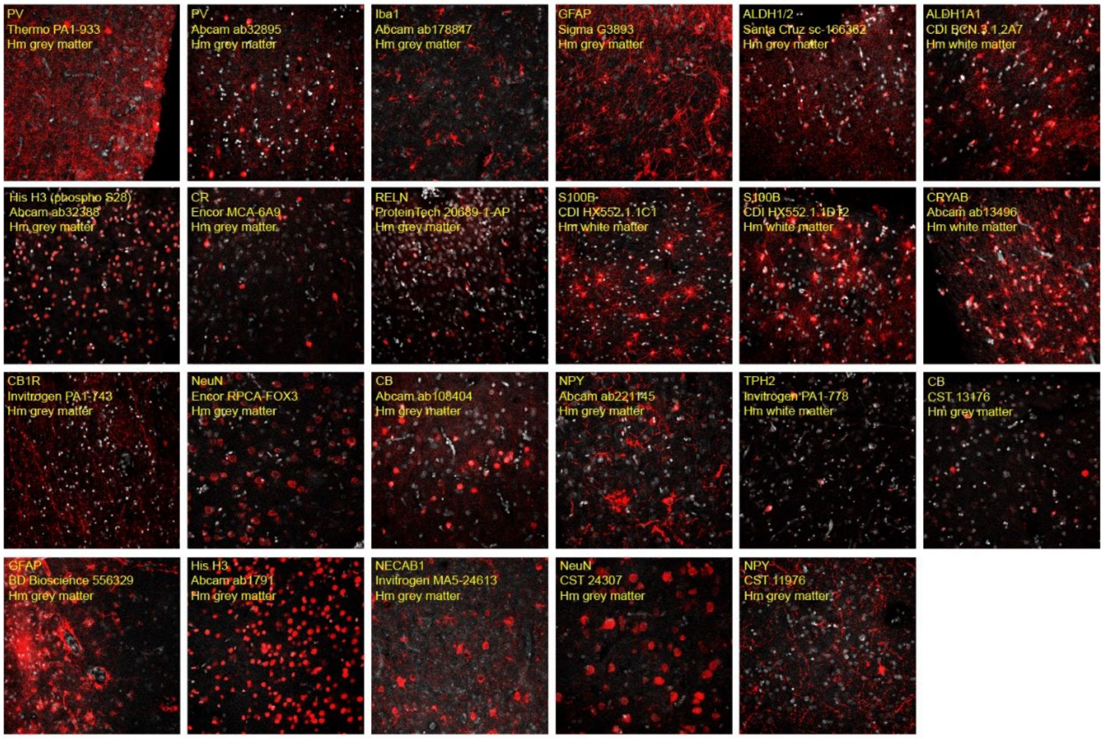

Human SHIELD

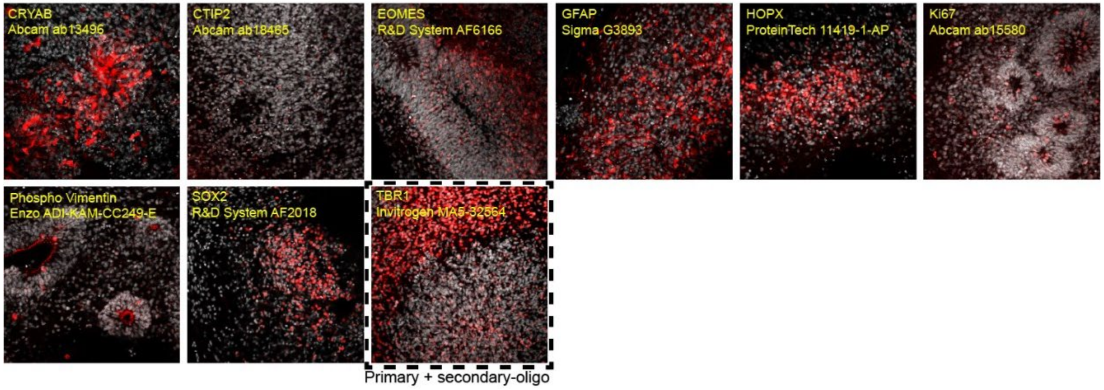

Human Cerebral Organoid SHIELD

Figure 3-2. Representative staining images of DNA oligo conjugated antibodies of multiple sources of tissue (continued).

3.2.2 Preparation of photo-stable hybridization chain reaction (HCR) hairpins

Apart from constructing the DNA oligo conjugated antibody library, another practical challenge for imaging 3D tissues is the photo-bleaching of fluorophores during volumetric imaging. Popular options of fluorophores (e.g., Alexa Fluors) turned out photo-unstable during the long laser emission of confocal microscopy. Therefore, we found alternative fluorophores from SETA Biomedicals for channels of 647, 555, and 488 nm with outstanding photostability (**Figure 3-3 a**). Together with Alexa Fluor 790, a set of photo-stable HCR hairpins were prepared for simultaneous five channel image acquisition across UV-Vis-NIR wavelengths (**Figure 3-3 b**).

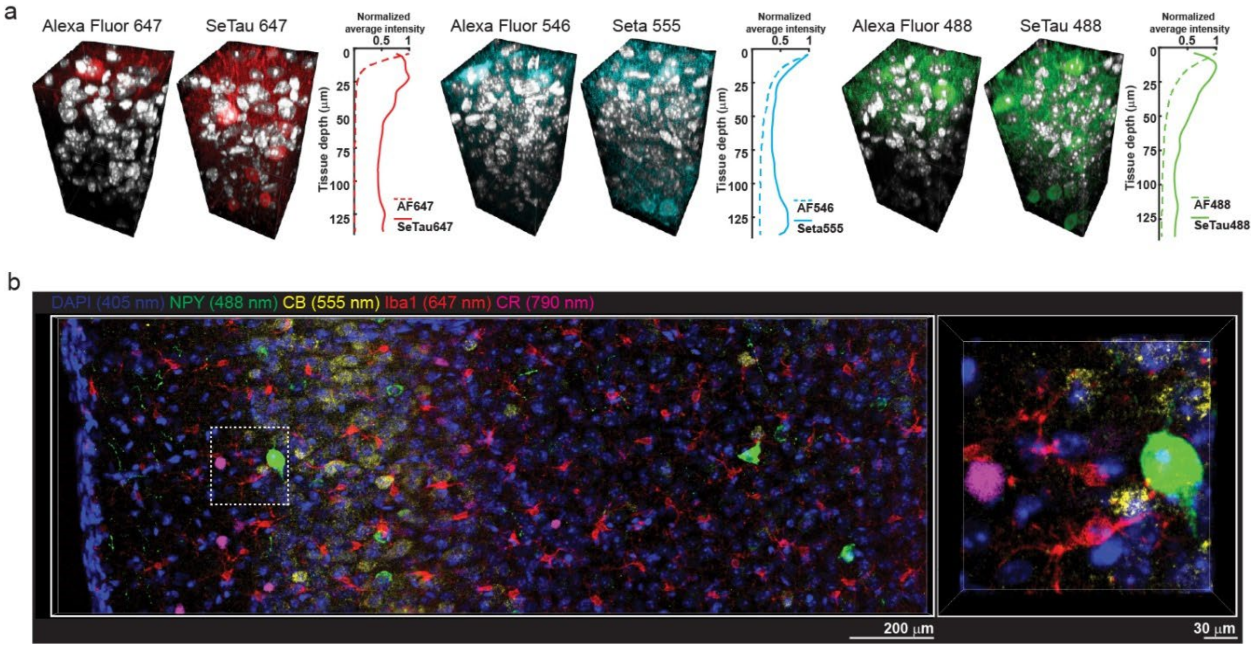

Figure 3-3. Homemade HCR hairpins optimized for fluorescent imaging of volumetric tissue samples. (**a**) Selected dyes with great photostability ensure the quality of deep imaging. (**b**) Five channel imaging is realized with homemade HCR hairpin set. Images are acquired via Andor Dragonfly Spinning Disk Microscope with 25x objective (Leica HCX IRAPO L 25x/0.95 W).

3.2.3 Validation of uniformity and controllability of antibody labeling on volumetric tissues

Volumetric staining uniformity was evaluated using 1 mm thick SHIELD-processed[3] mouse brain coronal slabs. We confirmed clear and strong signals across the tissue volume with minimal differences in intensity for all antibodies tested (**Figure 3-4 a)**, indicating the effectiveness of our strategy to slow down antibody binding kinetics and consequently achieve uniform staining. We repeated the experiment with a reduced amount of DNA oligo conjugated antibodies to validate the proposed stochastic sparse labeling regime and successfully observed a sparse, dot-like signal distribution for all markers (**Figure 3-4 b**). To confirm the specificity, the tissues were re-stained using orthogonal primary and secondary antibodies. The resulting co-localization patterns confirmed the labeling specificity of stochastic sparse labeling, and thus verified the predicted capability to modulate labeling density for controllable proteomic labeling on thick tissues by simply adjusting the amount of antibody used.

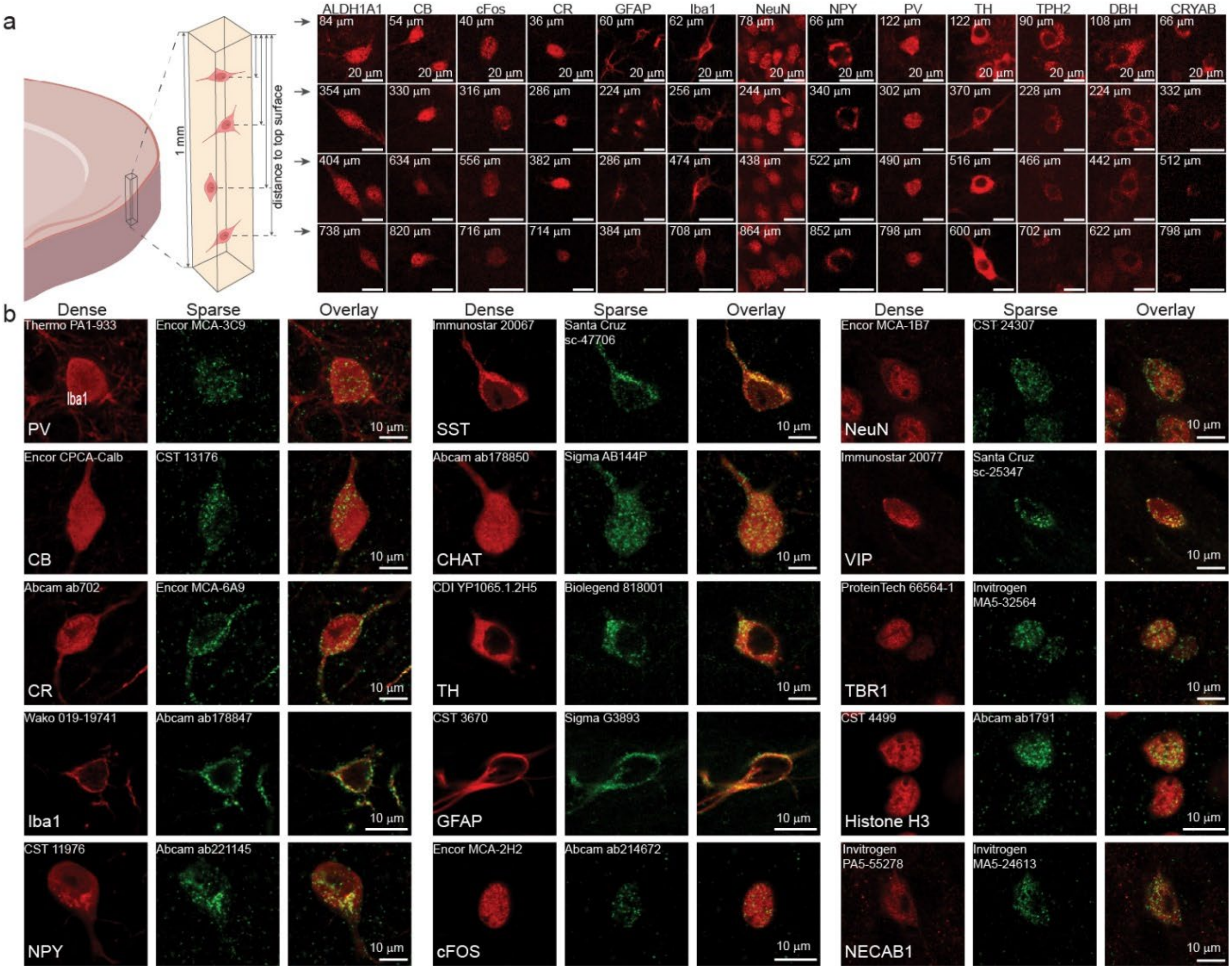

Figure 3-4. Both labeling modalities of spatial proteomic mapping platform are validated with barcoded antibodies. (**a**) Uniform labeling of various cell-type specific antigens is observed on millimeter-scaled tissues. SHIELD processed mouse brain tissue is sliced into 1 mm thick tissue slabs, and incubated with DNA oligo conjugated antibodies under dense labeling condition. Images are acquired via confocal microscope (Leica TCS SP8 X) with 25x objective (Leica HCX IRAPO L 25x/0.95 W). The numbers on the top left corner of each image indicate the distances to the upper surface of the 1 mm slab. (**b**) Protein signals are transformed into sparse, resolvable dot-like patterns without losing specificity. Multiple cell-type specific antigens are labeled with DNA oligo conjugated antibodies under stochastic sparse labeling condition. The signals of DNA oligo conjugated antibodies are colocalized with signals of subsequent indirect IHC from a different antibody as control (catalog information on the top left corner of each image). Control antibodies from different host species are chosen to avoid cross reaction of IHC to DNA oligo conjugated antibodies. Images are acquired via confocal microscope (Leica TCS SP8 X) with 63x objective (Leica HC PL APO 63x/1.30 GLYC CORR CS2).

The uniformity of stochastic sparse labeling was assessed using 200 um thick mouse brain coronal slabs incubated with PV, NeuN and cFOS-targeting conjugated antibodies. The three selected targets represented antigens empirically observed to be with varying expression levels, which is a critical consideration as according to our model, the surface bias in labeling intensity can be amplified by antigen density (**Figure 3-5 c**). To demonstrate the effectiveness of our proposed chemical environment (reduced binding reaction rate and high equilibrium constant) for uniform, volumetric stochastic sparse labeling, the intensity profile along the z axis was evaluated for three different cases: 1) fast binding with high antibody concentration (PBST-based conventional labeling condition), 2) fast binding with low antibody concentration and 3) slow binding with low antibody concentration (NaDC-containing buffer environment, see **Table 1** for corresponding antibody amounts). When the binding reaction rate was not controlled (cases 1 and 2), a strong signal bias towards the tissue surfaces was observed for antigens with high to medium expression levels, while uniform sparse labeling was observed in our novel NaDC-containing labeling environment (**Figure 3-5 a**). To quantify the variation of the volumetric labeling intensity, the soma of sparsely labeled cells at 10um intervals throughout the tissue volume was manually segmented and the average signal intensity was measured (**Figure 3-5 b**). Compared to PBST-based conventional methods, a 33-62% reduction in the magnitude of the standard deviation for signal intensity was observed (**Figure 3-6**), confirming the previous observations on uniformity of stochastic sparse labeling. As predicted by our model, surface bias is less of an issue for low density antigens, yet it is noteworthy to mention that the signal specificity and sensitivity are maintained in the NaDC-containing buffer environment, demonstrating broad range of applicability of this strategy.

The evaluation of the intensity profile across antigens with varying expression levels highlights an additional benefit of implementing reduced binding kinetics: a narrowed range of labeling density among different antigens (**Figure 3-5 b,c**). This feature becomes particularly relevant when large differences in protein abundance are expected among target protein sets. Moreover, to validate the ability to control labeling density for each individual antigen, we quantified the number of sparsely labeled protein dots per cell soma with varying amount of calbindin (CB) targeting DNA oligo conjugated antibody

(**Figure 3-5 d)**. The quantification of the number of dots per cell soma showed a positive correlation ($R = 0.9479$, $p \leq 0.05$) to the amount of antibody (**Figure 3-5 e),** substantiating our model's predictions. Therefore, through narrowing the range of labeling densities among all antigens with each of them tunable, our platform greatly facilitates the implementation of spatial proteomics for a broad range of targets and applications.

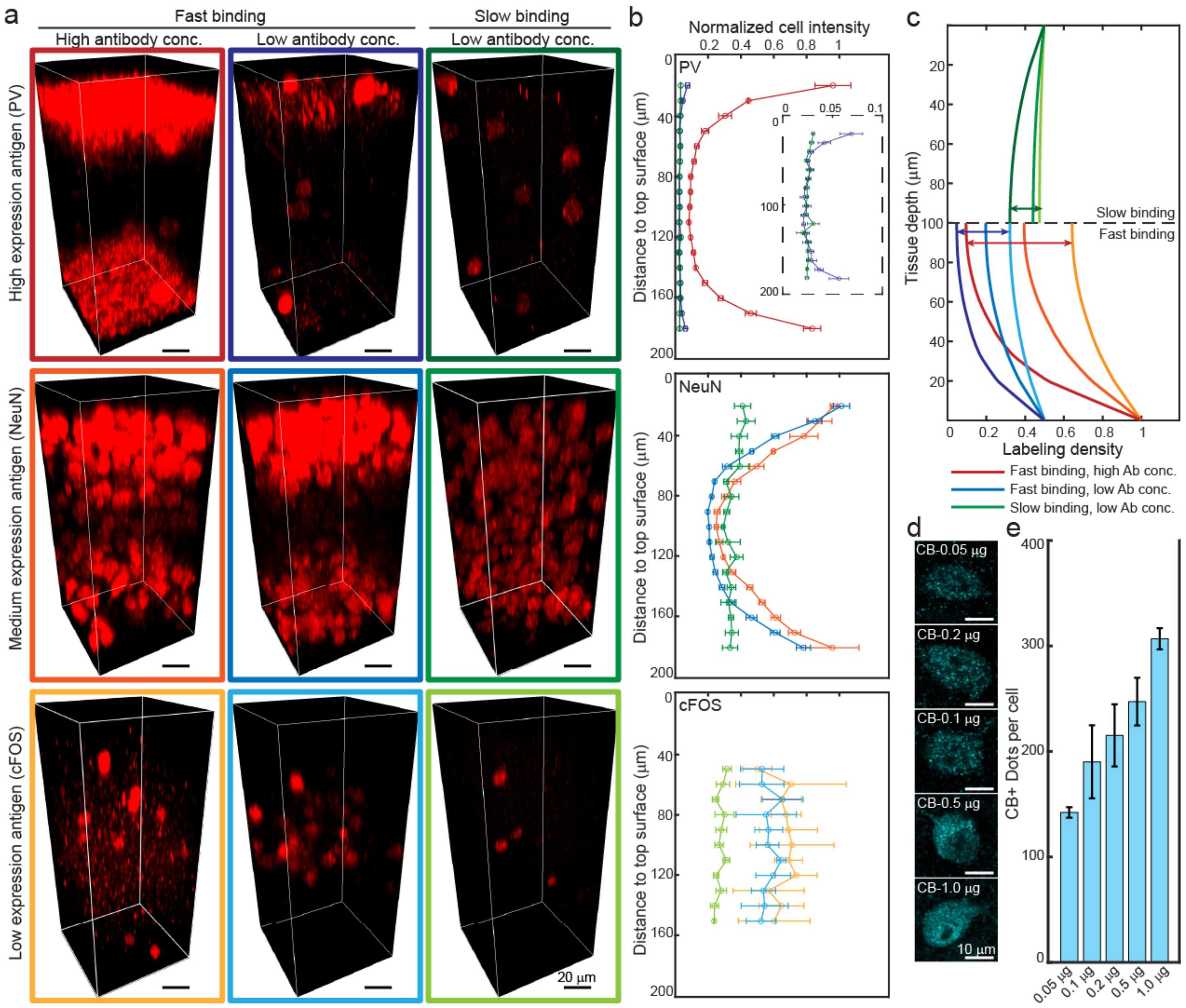

Figure 3-5. Stochastic sparse labeling enables uniform, antigen-independent, and easy-to-practice transformation of protein signals into resolvable pattern. (**a-b**) Comparison of uniformity between conventional labeling, conventional labeling with less amount of antibodies and stochastic sparse labeling conditions on thick tissues. (**a**) 3D display of signal gradients of PV, NeuN and cFOS labeling in SHIELD processed mouse brain tissues. Representative cells are selected from multiple depths for evaluating signal intensity. (**b**) Quantitative measurement of average fluorescent intensity of cells at certain depths in tissue volume. The somas of PV, NeuN and cFOS cells labeled were circled with ImageJ. The average signal intensity of circled area was measured. (**c**) Stochastic sparse labeling narrows the range of signal intensity among antigens with different expression levels. Signals from proteins with significantly different copy numbers can be evened to avoid overlapping signal dominance. (**d-e**) Labeling density of proteins is controlled by adjusting the amount of DNA oligo conjugated antibody. (**d**) Representative cell images of stochastic sparse labeling with a gradient amount of calbindin (CB) antibody. (**e**) Number of detected CB+ dots across increased amount of antibody. A positive

correlation between antibody amount and number of dots is observed (R = 0.9479, $P < 0.05$).

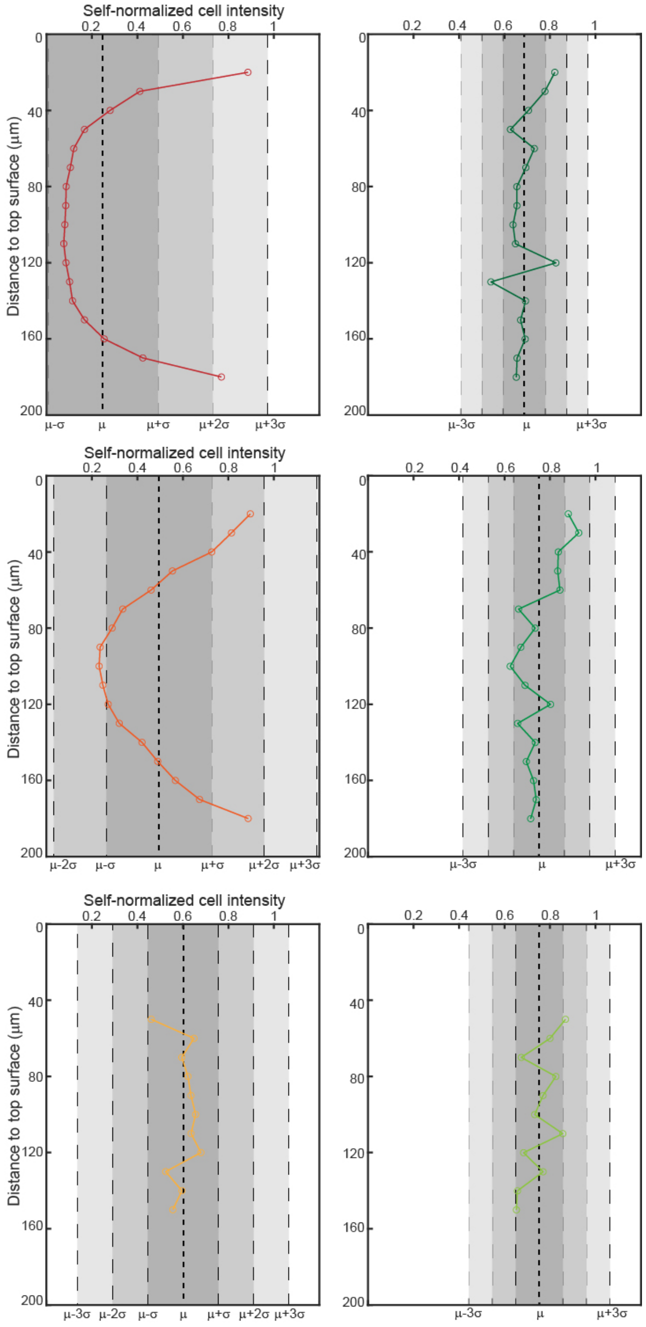

Figure 3-6. Mean and standard deviation of signal intensity under stochastic sparse labeling and conventional labeling conditions.

Table 1. Primary antibodies used for stochastic sparse labeling.

Mouse brain, sagittal slice

Antibody	Catalog #	Vendor	Host	Clonality	Amount used
Anti-Parvalbumin	MCA-3C9	Encor	Rabbit	Monoclonal	2 ug
Anti-Calbindin	13176	CST	Rabbit	Monoclonal	0.1 ug
Anti-Calretinin	MCA-6A9	Encor	Mouse	Monoclonal	0.5 ug
Anti-Iba1	ab178847	Abcam	Rabbit	Monoclonal	0.3 ug
Anti-Neuropeptide Y	ab221145	Abcam	Rabbit	Monoclonal	0.2 ug
Anti-Somatostatin	sc-47706	Santa Cruz	Rat	Monoclonal	0.004 ug + 0.1 ug Fab
Anti-Choline acetyltranferase	AB144P	Millipore Sigma	Goat	Polyclonal	0.1 uL + 0.2 ug Fab
Anti-Tyrosine hydroxylase	818001	Biolegend	Mouse	Monoclonal	0.005 ug
Anti-GFAP	G3893	Sigma	Mouse	Monoclonal	0.05 ug
Anti-c-Fos	ab214672	Abcam	Rabbit	Monoclonal	0.5 ug
Anti-NeuN	24307	CST	Rabbit	Monoclonal	0.1 ug
Anti- Vasoactive intestinal peptide	sc-25347	Santa Cruz	Mouse	Monoclonal	3 ug + 0.1 ug Fab
Anti-TBR1	MA5-32564	Invitrogen	Rabbit	Monoclonal	0.2 ug + 0.01 ug Fab
Anti-NECAB1	MA5-24613	Invitrogen	Mouse	Monoclonal	0.5 ug

Human brain, grey matter slice

Antibody	Catalog #	Vendor	Host	Clonality	Amount used
Anti-Parvalbumin	PA1-933	Thermo	Rabbit	Polyclonal	0.2 ug
Anti-Calbindin	ab108404	Abcam	Rabbit	Monoclonal	0.2 ug
Anti-Calretinin	MCA-6A9	Encor	Mouse	Monoclonal	0.5 ug
Anti-Iba1	ab178847	Abcam	Rabbit	Monoclonal	0.001 ug
Anti-Neuropeptide Y	11976	CST	Rabbit	Monoclonal	0.2 ug
Anti-Somatostatin	sc-47706	Santa Cruz	Rat	Monoclonal	0.01 ug + 0.1 ug Fab
Anti-GFAP	G3893	Sigma	Mouse	Monoclonal	0.02 ug
Anti-NeuN	24307	CST	Rabbit	Monoclonal	0.5 ug
Anti-NECAB1	MA5-24613	Invitrogen	Mouse	Monoclonal	0.5 ug

Additional antibodies

Antibody	Catalog #	Vendor	Host	Clonality

Anti-Histone H3 (phosphor S28)	ab32388	Abcam	Rabbit	Monoclonal
Anti-Synaptotagmin 6	MA5-27599	Invitrogen	Mouse	Monoclonal
Anti-CTIP2	ab18465	Abcam	Rat	Monoclonal
Anti-CB1 Receptor	93815	CST	Rabbit	Monoclonal
Anti-PCDH20	LS-C139337	LSBio	Mouse	Monoclonal
Anti-PDGFRA	3174	CST	Rabbit	Monoclonal
Anti-Ki67	ab15580	Abcam	Rabbit	Polyclonal
Anti-SATB2	ab51502	Abcam	Mouse	Monoclonal
Anti-ALDH1/2	sc-166362	Santa Cruz	Mouse	Monoclonal
Anti-ALDH1A1	ab215996	Abcam	Rabbit	Monoclonal
Anti-ALDH1A1	BCN.3.1.2A7	CDI	Mouse	Monoclonal
Anti-Orexin A	sc-80263	Santa Cruz	Mouse	Monoclonal
Anti-Meis2	sc-81986	Santa Cruz	Mouse	Monoclonal
Anti-S100B	HX552.1.1C1	CDI	Mouse	Monoclonal
Anti-S100B	HX552.1.1D12	CDI	Mouse	Monoclonal
Anti-Olig2	ab220796	Abcam	Rabbit	Monoclonal
Anti-nNOS	ab1376	Abcam	Goat	Polyclonal
Anti-PCP4	BCN16.2.1A10	CDI	Mouse	Monoclonal
Anti-Reelin	20689-1-AP	ProteinTech	Rabbit	Polyclonal
Anti-MAP2	8707	CST	Rabbit	Monoclonal

3.2.4 Implementation of combinatorial barcoding strategy in spatial proteomics

Stochastic sparse labeling enables the implementation of combinatorial barcoding strategies that display an exponential growth in the number of target proteins. To validate such potential, an N = C^R (C-number of channels; R-number of imaging rounds) multiplexed scheme with combinatorial barcoding of signals was designed to resolve popular neuronal and non-neuronal markers on SHIELD-processed mouse brain sagittal slices. The tissues were simultaneously labeled with a set of fourteen DNA-oligo conjugated antibodies under stochastic sparse labeling conditions (**Figure 3-7 a**, **Table 1**). Following 3 sequential rounds of hybridization chain reaction (HCR) amplification with custom photo-stable hairpins (**Figure 3-3**) and confocal imaging, the barcodes were resolved to identify all 14 protein targets in their corresponding brain regions, including ChAT+ neurons, NeuN+ neurons, Iba1+ microglia, TH+ neurons and VIP+ neurons in thalamus/hypothalamus; SST+ neurons, NECAB1+ neurons, NeuN+ neurons; and PV+ neurons, NPY+ neurons, TBR1+ neurons, CB+ neurons, SST+ neurons, CR+ neurons, and Iba1+ microglia in visual cortex (**Figure 3-7 b**). Similar multiplexed combinatorial barcoding of proteins was repeated on human brain samples (**Figure 3-8, Table 1**), showing the flexibility and applicability of our platform to types of sources and quality.

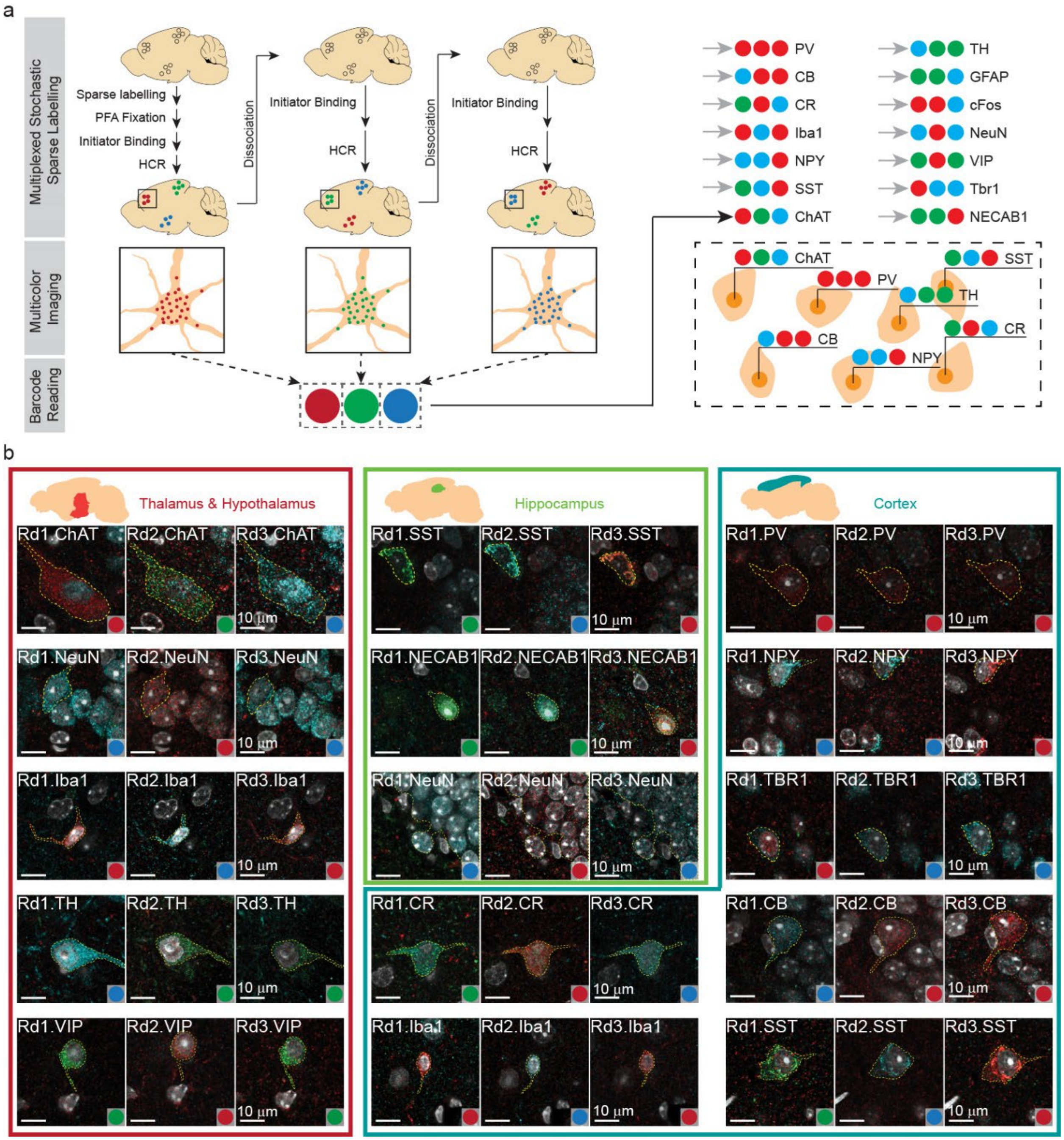

Figure 3-7. Multiplexed cellular characterization is enabled with stochastic sparse labeling implemented with combinatorial protein barcoding scheme. (**a**) The pipeline of multi-channel, multi-round proteomic mapping with combinatorial protein barcoding. Mouse brain samples are SHIELD-processed, delipidated, sagittally sliced, and labeled with all involved DNA oligo conjugated antibodies in one shot. The tissue is subsequently fixed with paraformaldehyde, hybridized with initiator, amplified through HCR, and imaged to read the first barcode for all markers involved. The same sagittal slice is washed off, and then subject to two additional rounds of hybridization, amplification and imaging until all the barcodes are acquired. (**b**) Representative images of selected cells from multiple

brain regions. Images are acquired via confocal microscope (Leica TCS SP8 X) with 63x objective (Leica HC PL APO 63x/1.30 GLYC CORR CS2). Images across three rounds are shown in parallel to present the combinatorial color barcode.

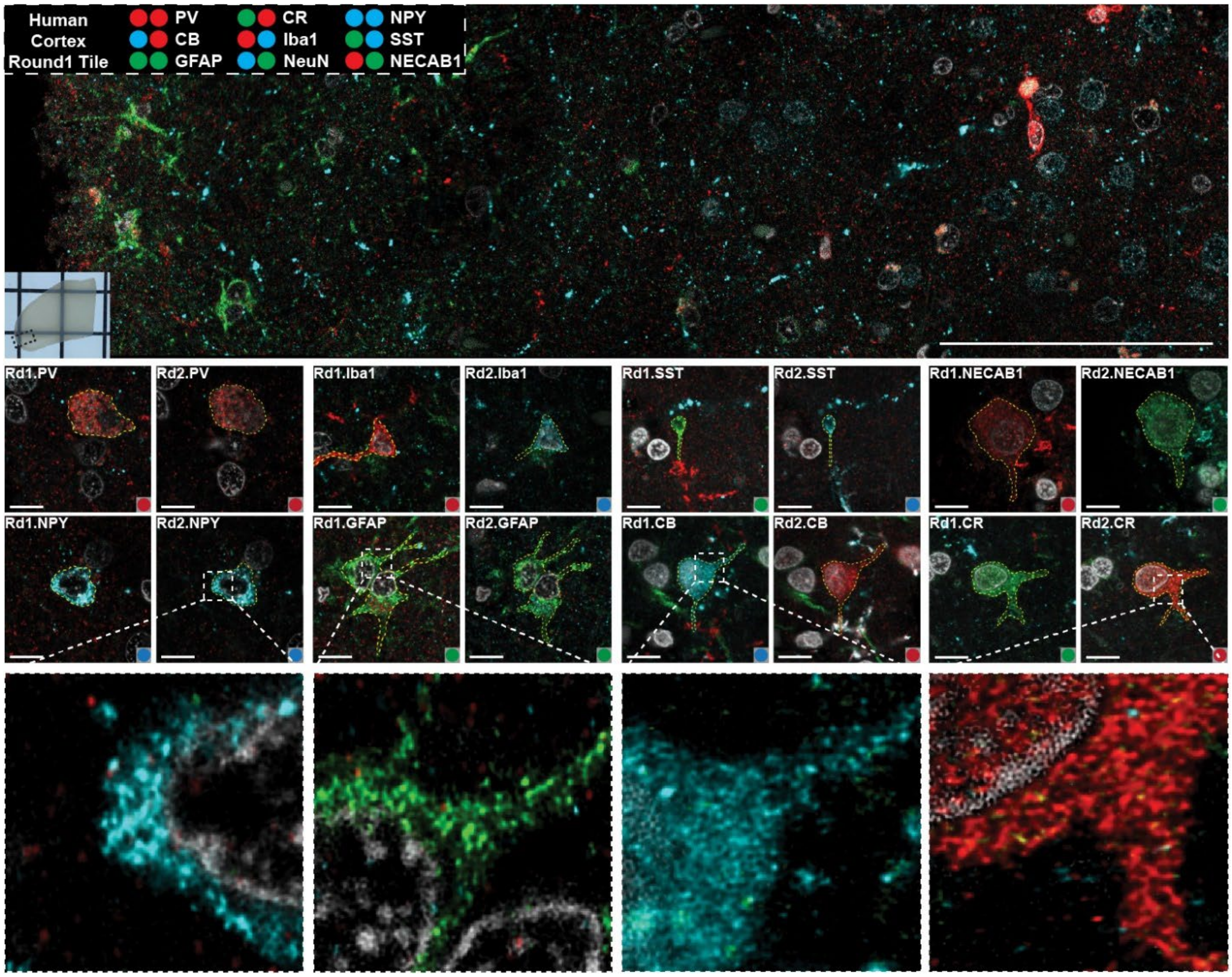

Figure 3-8. Representative images of spatial proteomic mapping with combinatorial barcoding in cortex of human brain. Images of two rounds are shown in parallel to present the combinatorial color barcode. Sparse protein pattern is shown in zoomed in images.

3.3 Methods

3.3.1 Mice

Young adult (2-4 month) C57BL/6 mice were housed in a 12 h light/dark cycle with unrestricted access to food and water. All experimental protocols were approved by the MIT Institutional Animal Care and Use Committee and the Division of Comparative Medicine and were in accordance with guidelines from the National Institute of Health.

3.3.2 SHIELD tissue preparation (Mouse)

The mouse brain tissue slices that were used in this study were preserved according to the lately published SHIELD protocol[3]. C57BL/6 mice were transcardially perfused with ice-cold 1XPBS with 10 U/mL heparin first, and then with SHIELD perfusion solution. The brains were dissected and then incubated in the SHIELD perfusion solution at 4 ^{o}C for 48 h with gentle shaking. The whole mouse brains were cut into hemispheres and transferred to ice-cold SHIELD-OFF solution (20% [w/v] P3PE in 0.1M sodium phosphate, 10mM sodium chloride pH 7.4) and further incubated at 4 ^{o}C for 24 h with gentle shaking. The hemispheres were then transferred to SHIELD-ON solution (0.1M sodium carbonate buffer at pH 10) and incubated at 37 ^{o}C for 24 h with gentle shaking. Afterwards the hemispheres were finally washed in 1XPBS with 0.02% sodium azide before sliced into 200 um slices with a vibratome.

3.3.3 Passive clearing of mouse brain tissues

The SHILED-processed 200 um brain slices were incubated in the clearing buffer (300 mM SDS, 10 mM sodium borate, 100 mM sodium sulfite, pH 9.0) at 37 ^{o}C for 12 h with gentle shaking. Then the cleared slices were thoroughly washed and kept in PBST.

3.3.4 Functionalization of 42nt adaptor sequence

The 42nt adaptor sequence oligos were adopted from ImmunoSABER and summarized in **Table 2**[73]. These 42nt adaptor sequence oligos were synthesized by Integrated DNA Technologies Inc. with 5’ amine modification at a concentration of 100 uM. The adaptor sequence oligos were modified with 200 eq-molar TCO-PEG4-NHS Ester (Click Chemistry Tools, Cat. No. A137) in 0.1 M sodium bicarbonate buffer with 40% (v/v) formamide (Sigma Aldrich) at room temperature for 12 h. Then the mixtures were precipitated by adding 3 volumes of ethanol with a subsequent 30-minute incubation at -20 °C. The modified oligos were pelleted with high-speed centrifugation and washed twice with ice-cold 70% ethanol to remove the excess reagent. Afterwards the modified oligo pellets were dissolved in DI water, and the ethanol precipitation process was repeated for another two rounds in order to completely remove TCO-PEG4-NHS. The purity of the modified 42nt adaptor sequences was determined by running samples on a denatured 15% Urea-TBE PAGE (Bio-Rad Inc. Cat. No. 4566056) followed by SYBR gold staining.

Table 2. bc42*-HCR initiator sequences.

ID	Sequence
B1I1-Bc42-1*-B1I2	GAGGAGGGCAGCAAACGGGAAGAGTCTTCCTTTACGATATATAGGTCGGTTAAGGACACGGAGATTTGGCGGTAGGGATAATATATGCATTCTTTCTTGAGGAGGGCAGCAAACGGGAAGAG
B1I1-Bc42-2*-B1I2	GAGGAGGGCAGCAAACGGGAAGAGTCTTCCTTTACGATATGGAGAGGAATAGGATCGTACAGTGGATAAGGCGGCGATAACGATATGCATTCTTTCTTGAGGAGGGCAGCAAACGGGAAGAG
B3I1-Bc42-2*-B3I2	GTCCCTGCCTCTATATCTCCACTCAACTTTAACCCGATATGGAGAGGAATAGGATCGTACAGTGGATAAGGCGGCGATAACGATATAAAGTCTAATCCGTCCCTGCCTCTATATCTCCACTC
B1I1-Bc42-3*-B1I2	GAGGAGGGCAGCAAACGGGAAGAGTCTTCCTTTACGATATCTGTTGCGCGGGAGAACGACACGGACGCTAAATATAGGAAACATATGCATTCTTTCTTGAGGAGGGCAGCAAACGGGAAGAG
B3I1-Bc42-3*-B3I2	GTCCCTGCCTCTATATCTCCACTCAACTTTAACCCGATATCTGTTGCGCGGGAGAACGACACGGACGCTAAATATAGGAAACATATAAAGTCTAATCCGTCCCTGCCTCTATATCTCCACTC
B4I1-Bc42-3*-B4I2	CCTCAACCTACCTCCAACTCTCACCATATTCGCTTCATATCTGTTGCGCGGGAGAACGACACGGACGCTAAATATAGGAAACATATCACATTTACAGACCTCAACCTACCTCCAACTCTCAC
B1I1-Bc42-4*-B1I2	GAGGAGGGCAGCAAACGGGAAGAGTCTTCCTTTACGATATAACGCAATACCCAGACGAGACAACACGCGAAGACTTAAGATAATATGCATTCTTTCTTGAGGAGGGCAGCAAACGGGAAGAG
B3I1-Bc42-4*-B3I2	GTCCCTGCCTCTATATCTCCACTCAACTTTAACCCGATATAACGCAATACCCAGACGAGACAACACGCGAAGACTTAAGATAATATAAAGTCTAATCCGTCCCTGCCTCTATATCTCCACTC
B1I1-Bc42-5*-B1I2	GAGGAGGGCAGCAAACGGGAAGAGTCTTCCTTTACGATATAGGGTGCGCAGTAACTTTAAGGGTAGGATCGTCGGGACAGGAATATGCATTCTTTCTTGAGGAGGGCAGCAAACGGGAAGAG
B3I1-Bc42-5*-B3I2	GTCCCTGCCTCTATATCTCCACTCAACTTTAACCCGATATAGGGTGCGCAGTAACTTTAAGGGTAGGATCGTCGGGACAGGAATATAAAGTCTAATCCGTCCCTGCCTCTATATCTCCACTC
B1I1-Bc42-6*-B1I2	GAGGAGGGCAGCAAACGGGAAGAGTCTTCCTTTACGATATACGGCTATATAGGAAACGATACGCACGACTCCTACCTCACCGATATGCATTCTTTCTTGAGGAGGGCAGCAAACGGGAAGAG
B3I1-Bc42-6*-B3I2	GTCCCTGCCTCTATATCTCCACTCAACTTTAACCCGATATACGGCTATATAGGAAACGATACGCACGACTCCTACCTCACCGATATAAAGTCTAATCCGTCCCTGCCTCTATATCTCCACTC
B4I1-Bc42-6*-B4I2	CCTCAACCTACCTCCAACTCTCACCATATTCGCTTCATATACGGCTATATAGGAAACGATACGCACGACTCCTACCTCACCGATATCACATTTACAGACCTCAACCTACCTCCAACTCTCAC
B1I1-Bc42-7*-B1I2	GAGGAGGGCAGCAAACGGGAAGAGTCTTCCTTTACGATATGACGGTGAATGTACGACTATGCGACGGGATACTACAGGAACTATATGCATTCTTTCTTGAGGAGGGCAGCAAACGGGAAGAG
B3I1-Bc42-7*-B3I2	GTCCCTGCCTCTATATCTCCACTCAACTTTAACCCGATATGACGGTGAATGTACGACTATGCGACGGGATACTACAGGAACTATATAAAGTCTAATCCGTCCCTGCCTCTATATCTCCACTC
B4I1-Bc42-7*-B4I2	CCTCAACCTACCTCCAACTCTCACCATATTCGCTTCATATGACGGTGAATGTACGACTATGCGACGGGATACTACAGGAACTATATCACATTTACAGACCTCAACCTACCTCCAACTCTCAC
B3I1-Bc42-8*-B3I2	GTCCCTGCCTCTATATCTCCACTCAACTTTAACCCGATATCGATGTTGGCGGTAAGACGGTATAAGGCGGAGCTGAATTGTTATATAAAGTCTAATCCGTCCCTGCCTCTATATCTCCACTC
B4I1-Bc42-8*-B4I2	CCTCAACCTACCTCCAACTCTCACCATATTCGCTTCATATCGATGTTGGCGGTAAGACGGTATAAGGCGGAGCTGAATTGTTATATCACATTTACAGACCTCAACCTACCTCCAACTCTCAC
B3I1-Bc42-9*-B3I2	GTCCCTGCCTCTATATCTCCACTCAACTTTAACCCGATATTACAAGCGGGAACACGAGTTAGACATAGAACGGGCCAAATTCATATAAAGTCTAATCCGTCCCTGCCTCTATATCTCCACTC
B4I1-Bc42-9*-B4I2	CCTCAACCTACCTCCAACTCTCACCATATTCGCTTCATATTACAAGCGGGAACACGAGTTAGACATAGAACGGGCCAAATTCATATCACATTTACAGACCTCAACCTACCTCCAACTCTCAC
B1I1-Bc42-10*-B1I2	GAGGAGGGCAGCAAACGGGAAGAGTCTTCCTTTACGATATTAATACAAAGCGCATACGGGAAAATGCGGAAAGAGCGAGGACATATGCATTCTTTCTTGAGGAGGGCAGCAAACGGGAAGAG
B3I1-Bc42-10*-B3I2	GTCCCTGCCTCTATATCTCCACTCAACTTTAACCCGATATTAATACAAAGCGCATACGGGAAAATGCGGAAAGAGCGAGGACATATAAAGTCTAATCCGTCCCTGCCTCTATATCTCCACTC
B1I1-Bc42-11*-B1I2	GAGGAGGGCAGCAAACGGGAAGAGTCTTCCTTTACGATATATTGTTGGAACGGCGGCATAGGGCGGCATTAGAATTTAGACAATATGCATTCTTTCTTGAGGAGGGCAGCAAACGGGAAGAG
B3I1-Bc42-11*-B3I2	GTCCCTGCCTCTATATCTCCACTCAACTTTAACCCGATATATTGTTGGAACGGCGGCATAGGGCGGCATTAGAATTTAGACAATATAAAGTCTAATCCGTCCCTGCCTCTATATCTCCACTC
B4I1-Bc42-11*-B4I2	CCTCAACCTACCTCCAACTCTCACCATATTCGCTTCATATATTGTTGGAACGGCGGCATAGGGCGGCATTAGAATTTAGACAATATCACATTTACAGACCTCAACCTACCTCCAACTCTCAC
B1I1-Bc42-12*-B1I2	GAGGAGGGCAGCAAACGGGAAGAGTCTTCCTTTACGATATAGGGTCGGGTTGGGCTTCGGGTCAAATTCATACGGCGGAAGGATATGCATTCTTTCTTGAGGAGGGCAGCAAACGGGAAGAG
B4I1-Bc42-12*-B4I2	CCTCAACCTACCTCCAACTCTCACCATATTCGCTTCATATAGGGTCGGGTTGGGCTTCGGGTCAAATTCATACGGCGGAAGGATATCACATTTACAGACCTCAACCTACCTCCAACTCTCAC
B1I1-Bc42-13*-B1I2	GAGGAGGGCAGCAAACGGGAAGAGTCTTCCTTTACGATATGCGAGAGGACAATAACCGATAAGTGACGCGATACAAGAACTGATATGCATTCTTTCTTGAGGAGGGCAGCAAACGGGAAGAG
B3I1-Bc42-13*-B3I2	GTCCCTGCCTCTATATCTCCACTCAACTTTAACCCGATATGCGAGAGGACAATAACCGATAAGTGACGCGATACAAGAACTGATATAAAGTCTAATCCGTCCCTGCCTCTATATCTCCACTC
B1I1-Bc42-16*-B1I2	GAGGAGGGCAGCAAACGGGAAGAGTCTTCCTTTACGATATATGGTGATCTCGGCGAAGACAGCGCATTAAGGGGATAACACTATATGCATTCTTTCTTGAGGAGGGCAGCAAACGGGAAGAG
B4I1-Bc42-16*-B4I2	CCTCAACCTACCTCCAACTCTCACCATATTCGCTTCATATATGGTGATCTCGGCGAAGACAGCGCATTAAGGGGATAACACTATATCACATTTACAGACCTCAACCTACCTCCAACTCTCAC

3.3.5 Antibody oligo conjugation

The information of the primary antibodies used for multiplex staining was summarized in **Table 3**. 100 ug of whole fraction IgG, IgA or Fab fragments were subject to buffer exchange to nitrogen-purged, ice-cold reaction buffer (0.1 M sodium phosphate, 0.15 M sodium chloride, 10 mM EDTA at pH 7.4) with Zeba desalting spin column (ThermoFisher, Cat. No. 89883, 7 kDa) to remove the preservatives. Then the buffer-exchanged antibodies were reduced by 1 mM TCEP at 37 ^oC for 30 minutes with gentle shaking, and the residual TCEP was removed by the buffer exchange to reaction buffer with Zeba desalting spin column. If the concentration of the antibody solution is below 1 mg/mL, the resulting eluent needed to be concentrated by Amicon mass cut-off spin column (Millipore Sigma-Aldrich, 30 kDa, 0.5 mL, Cat. No. UFC503096) so that the concentration reached 1-2 mg/mL. Then bis-sulfone methyltetrazine was added to the antibody solution to reach the final concentration of 0.267 mM and the reaction mixtures were incubated for 15-16 h at room temperature with gentle shaking. The resulting mixtures were subjected to two rounds of buffer exchange to 1XPBS with 0.02% sodium azide with Zeba desalting spin column for the purpose of completely removing residual bis-sulfone methyltetrazine. Then 7.5 eq molar of a corresponding TCO modified 42nt adaptor sequence oligo was added to the antibody and the mixture was incubated for 12 h at room temperature with gentle shaking. The excess TCO modified 42nt adaptor sequence oligo was separated from the antibody-oligo conjugates via size-exclusion column chromatography (GE, Superdex 200 15-300 increase) in Akta pure 25L equipped with the fraction collector, and the relevant fractions were concentrated by Amicon mass cut-off spin column (Millipore Sigma-Aldrich, 30 kDa, 2 mL, Cat. No. UFC203024). The result of the oligo conjugation reaction was determined by applying a partial denaturation to antibody-oligo conjugates by incubating in 1x laemmli sds loading buffer mixture without reducing agent at 60 ^oC for 5 min. Then the samples were analyzed with 4-15% SDS PAGE. The final fractions containing antibody-oligo conjugates of interest were combined and were subject to concentration measurement using microBCA (Thermo). After the exact concentration was measured, preservatives such as 40% glycerol, 0.02%

sodium azide and 0.1% w/v BSA were added to the antibody-oligo conjugates and the product could be stored at 4 °C before use.

Table 3: bc42 oligo adaptor sequences[73].

ID	Bc42 sequences (antibody)	Bc42* sequences (HCR)
bc42-1	ATTATCCCTACCGCCAAATCTCCGTGTCCTTAACCGACCTAT	ATAGGTCGGTTAAGGACACGGAGATTTGGCGGTAGGGATAAT
bc42-2	CGTTATCGCCGCCTTATCCACTGTACGATCCTATTCCTCTCC	GGAGAGGAATAGGATCGTACAGTGGATAAGGCGGCGATAACG
bc42-3	GTTTCCTATATTTAGCGTCCGTGTCGTTCTCCCGCGCAACAG	CTGTTGCGCGGGAGAACGACACGGACGCTAAATATAGGAAAC
bc42-4	TATCTTAAGTCTTCGCGTGTTGTCTCGTCTGGGTATTGCGTT	AACGCAATACCCAGACGAGACAACACGCGAAGACTTAAGATA
bc42-5	TCCTGTCCCGACGATCCTACCCTTAAAGTTACTGCGCACCCT	AGGGTGCGCAGTAACTTTAAGGGTAGGATCGTCGGGACAGGA
bc42-6	CGGTGAGGTAGGAGTCGTGCGTATCGTTTCCTATATAGCCGT	ACGGCTATATAGGAAACGATACGCACGACTCCTACCTCACCG
bc42-7	AGTTCCTGTAGTATCCCGTCGCATAGTCGTACATTCACCGTC	GACGGTGAATGTACGACTATGCGACGGGATACTACAGGAACT
bc42-8	AACAATTCAGCTCCGCCTTATACCGTCTTACCGCCAACATCG	CGATGTTGGCGGTAAGACGGTATAAGGCGGAGCTGAATTGTT
bc42-9	GAATTTGGCCCGTTCTATGTCTAACTCGTGTTCCCGCTTGTA	TACAAGCGGGAACACGAGTTAGACATAGAACGGGCCAAATTC
bc42-10	GTCCTCGCTCTTTCCGCATTTTCCCGTATGCGCTTTGTATTA	TAATACAAAGCGCATACGGGAAAATGCGGAAAGAGCGAGGAC
bc42-11	TGTCTAAATTCTAATGCCGCCCTATGCCGCCGTTCCAACAAT	ATTGTTGGAACGGCGGCATAGGGCGGCATTAGAATTTAGACA
bc42-12	CCTTCCGCCGTATGAATTTGACCCGAAGCCCAACCCGACCCT	AGGGTCGGGTTGGGCTTCGGGTCAAATTCATACGGCGGAAGG
bc42-13	CAGTTCTTGTATCGCGTCACTTATCGGTTATTGTCCTCTCGC	GCGAGAGGACAATAACCGATAAGTGACGCGATACAAGAACTG
bc42-14	CCAACCTCTCGTACCAAATTCCGCCACTCAAGCCGTATCAAA	TTTGATACGGCTTGAGTGGCGGAATTTGGTACGAGAGGTTGG
bc42-15	GTTTCAAGAGTCCGTCGCAAATTCCACTACACGCTACGCCCA	TGGGCGTAGCGTGTAGTGGAATTTGCGACGGACTCTTGAAAC

3.3.6 Photo-stable dye conjugation of HCR hairpin

To functionalize HCR hairpins with 400 eq-molar DBCO, a 500uM solution of the desired hairpin, 1M NaHCO3, formamide, and 0.1M DBCO-PEG5-NHS were added to a clean tube in a 2:1:2:4 ratio and in order listed. The mixture was allowed to shake at room temperature for 2-3 hours. The hairpin samples were precipitated to remove excess DBCO-PEG5-NHS by adding sodium acetate (3M, pH 5.2) to the tube at a volume 1/10 that of the sample. 100% ethanol was also added at a volume 3x the sample volume (calculated after adding sodium acetate). The mixture was incubated at -20C for at least 15 minutes but up to overnight before being centrifuged at 14000g for 30 min at 4 ^{o}C. The supernatant was discarded, and the pellet was rinsed with ethanol. The pellet was centrifuged again, the supernatant was discarded, and the pellet was dissolved in water. The precipitation was repeated 2 more times.

To add dye to the hairpins, the concentration of the DBCO-functionalized hairpin mixture was measured, and then mixed with 3 eq-molar chosen fluorescent dye-PEG35-N_3. The mixture was left in a shaker at room temperature overnight, precipitated once to remove excess dye, and then the concentration was measured. The hairpins were purified by running through a 20cmx22cmx1.5mm 15% denaturing urea polyacrylamide preparatory gel for 3 hours[74]. After running, a UV lamp was used to visualize sample and dark impurity bands, then a clean razor blade was used to cut out sample bands. The excised bands were chopped into small pieces and put into a tube with a filter. About 200µL DI water was added to each tube, or enough to immerse gel pieces. The tubes were incubated at 37C overnight before being spun briefly in a centrifuge to elute sample in water. The volume of the hairpin mixture was reduced using a butanol extraction, then purified by use of 7k Zeba spin columns 2 times. The concentration and volume of the sample was measured, and then 5M NaCl added to make hairpin sample 0.3M in NaCl, and 60ng/µL in hairpins.

3.3.7 Stochastic sparse labeling with DNA oligo conjugated antibodies

200 um thick SHIELD processed brain slices were cleared passively as described above. Slices were firstly incubated in the 50 mM Tris/Glycine pH 9.0, 0.2% (w/v) dextran sulfate 500 kDa, 1% (w/v) sodium deoxycholate buffer for 1 h at room temperature with gentle shaking to remove the Triton X-100 in the tissue. Then the tissue slices were transferred to the stochastic sparse labeling buffer containing the oligo conjugated primary antibody (50 mM Tris/Glycine pH 9.0, 0.2% (w/v) dextran sulfate 500 kDa, 1% (w/v) sodium deoxycholate, 0.2 mg/mL denatured salmon sperm DNA, with appropriate amount of oligo conjugated antibody). The tissue slices were stained overnight at room temperature with gentle shaking. Then the slices were washed for 30 minutes at room temperature for two rounds with 50 mM Tris/Glycine pH 9.0, 0.2% (w/v) dextran sulfate 500 kDa, 1% (w/v) sodium deoxycholate buffer, and were further washed with 1XPBS, 0.1% (w/v) Triton X-100 for 1 h. Afterwards, the tissue slices were subject to chemical fixation to permanently localize antibody-oligo conjugates to withstand harsh formamide treatment for rehybridization and HCR cycles by incubating in 1XPBS, 4% (v/v) paraformaldehyde at 37 ^{o}C for 1 h with gentle shaking. The resulting sparsely labeled brain slices were subsequently hybridized with HCR initiators after complete removal of extra paraformaldehyde.

The hybridization buffer was prepared in accordance with the oligo conjugated antibody we used to stain. The hybridization buffer contained 2XSSC, 0.1% (w/v) Tween 20, 10% (w/v) dextran sulfate 500 kDa, 30% (v/v) formamide, 1 mg/mL denatured salmon sperm DNA, and 1 nM complimentary bc42-HCR initiator oligos. The complimentary bc42-HCR initiator oligos we used in this paper were summarized in Table 4. The sparsely labeled brain slices were incubated in the hybridization buffer that contained corresponding complimentary bc42-HCR initiator oligo to the oligo conjugated antibodies overnight at 37 ^{o}C with gentle shaking. Then the brain slices hybridized with HCR initiators were washed for 1 h in 2XSSC, 0.1% (w/v) Tween 20, 30% (v/v) formamide at 37 ^{o}C with gentle shaking for 3 rounds, and the formamide was further removed by rinsing the slices in 2XSSC, 0.1% (w/v) Tween 20. The sparsely labeled brain slices were hybridized with HCR initiators and were ready to get amplified by hybridization chain reaction.

3.3.8 Multiplex multi-round stochastic sparse labeling

200 um thick SHIELD processed brain slices were firstly stained with four unconjugated primary antibodies with respective oligo conjugated secondary Fab fragments. Slices were firstly incubated in the 50 mM Tris/Glycine pH 9.0, 0.2% (w/v) dextran sulfate 500 kDa, 1% (w/v) sodium deoxycholate buffer for 1 h at room temperature with gentle shaking to remove the Triton X-100 in the tissue. Then the tissue slices were transferred to the stochastic sparse labeling buffer containing the four unconjugated primary antibody (50 mM Tris/Glycine pH 9.0, 0.2% (w/v) dextran sulfate 500 kDa, 1% (w/v) sodium deoxycholate, with appropriate amount of antibody). The tissue slices were stained overnight at room temperature with gentle shaking. Then the slices were washed for 30 minutes at room temperature for two rounds with 50 mM Tris/Glycine pH 9.0, 0.2% (w/v) dextran sulfate 500 kDa, 1% (w/v) sodium deoxycholate buffer, and were further washed with 1XPBS, 0.1% (w/v) Triton X-100 for 1 h. At this point, the slices that were sparsely labeled with four unconjugated antibodies were transferred to 1XPBS, 0.1% (w/v) Triton X-100, 0.02% (w/v) sodium azide, 0.2% (w/v) dextran sulfate, 1 mg/mL denatured salmon sperm DNA with respective oligo conjugated Fab fragments. The tissue slices were incubated with oligo conjugated Fab fragments overnight at room temperature with gentle shaking. The extra Fab fragments were removed by washing the slices in 1XPBS, 0.1% (w/v) Triton X-100, 0.02% (w/v) sodium azide for 1 h for 2 rounds. Afterwards, the tissue slices were subject to chemical fixation by incubating in 1XPBS, 4% (v/v) paraformaldehyde at 37 ^{o}C for 1 h with gentle shaking. The resulting brain slices were subsequently stained with the other 11 oligo conjugated antibodies after complete removal of extra paraformaldehyde.

The slices that had been sparsely labeled with 4 unconjugated primary antibodies and their respective oligo conjugated Fab fragments were incubated in the 50 mM

Tris/Glycine pH 9.0, 0.2% (w/v) dextran sulfate 500 kDa, 1% (w/v) sodium deoxycholate buffer for 1 h at room temperature with gentle shaking to remove the Triton X-100 in the tissue. Then the slices were transferred to the stochastic sparse labeling buffer containing the fourteen oligo conjugated primary antibodies (50 mM Tris/Glycine pH 9.0, 0.2% (w/v) dextran sulfate 500 kDa, 1% (w/v) sodium deoxycholate, 0.2 mg/mL denatured salmon sperm DNA, with appropriate amount of oligo conjugated antibodies). The slices were stained overnight at room temperature with gentle shaking, and then were washed for 30 minutes at room temperature for two rounds with 50 mM Tris/Glycine pH 9.0, 0.2% (w/v) dextran sulfate 500 kDa, 1% (w/v) sodium deoxycholate buffer, and were further washed with 1XPBS, 0.1% (w/v) Triton X-100 for 1 h. Afterwards, the tissue slices were subject to chemical fixation by incubating in 1XPBS, 4% (v/v) paraformaldehyde at 37 ^{o}C for 1 h with gentle shaking. After complete removal of extra paraformaldehyde, the slices had been sparsely labeled by all the oligo conjugated antibodies so far and were ready for HCR initiator hybridization.

The hybridization buffer contained 2XSSC, 0.1% (w/v) Tween 20, 10% (w/v) dextran sulfate 500 kDa, 30% (v/v) formamide, 1 mg/mL denatured salmon sperm DNA, and 1 nM complimentary bc42-HCR initiator oligos for all the 15 antibodies that were sparsely labeled and fixed on the tissue. The sparsely labeled brain slices were incubated in the hybridization buffer overnight at 37 ^{o}C with gentle shaking. Then the brain slices hybridized with HCR initiators were washed for 1 h in 2XSSC, 0.1% (w/v) Tween 20, 30% (v/v) formamide at 37 ^{o}C with gentle shaking for 3 rounds, and the formamide was further removed by rinsing the slices in 2XSSC, 0.1% (w/v) Tween 20. The sparsely labeled brain slices were hybridized with HCR initiators and were ready to get amplified by hybridization chain reaction.

3.3.9 Individual dot segmentation and counting

The images of stochastic sparse labeling were processed and analyzed in ImageJ for dot segmentation and counting. Raw images with sparsely labeled protein dots were firstly transformed from RGB to 16-bit. Gaussian blur filter was applied to the 16-bit images with radius 1.5 and 10 respectively, between which the image with Gaussian blur radius 10 was considered as background. Then the background signal was subtracted from the image with Gaussian blur radius 1.5, and the resulting image was transformed into binary image by applying threshold. Overlapped dot signals were distinguished by applying binary watershed to the subtracted image. Particle analysis was conducted on the watershed processed image.

3.3.10 Refractive index matching for imaging thick tissues

Optical clearing of sparsely labeled, HCR amplified samples was achieved using Protos-based immersion medium[3]. 125 g iohexol, 3 g diatrizoic acid and 5 g N-methyl-d-glucamine were dissolved in 100 mL deionized (DI) water with the refractive index adjusted to 1.458 by adding DI water. Hydrochloric acid (HCl) was added to the solution until pH reached 7.5. Then magnesium acetate was added to the immersion medium with a final concentration of 50 mM Mg^{2+}. 200 um thick SHIELD processed mouse brain slices were incubated in the immersion media until the tissue became completely transparent.

3.4 Conclusion and discussion

Tunable labelling density is a key finding towards solving the challenge associated with high variation in protein copy number, and variable subcellular distribution in the ability to resolve multiple protein complexes without resorting to super-resolution microscopy and/or a very carefully designed targeting strategy[75,76]. Under standard conditions, the crowded signals prevent the implementation of the combinatorial barcoding strategies for increased multiplexity due to the potential confusion in barcode reading brought by overlap from co-expressed targets (**Figure 2-1**). Due to this inherent incompatibility, spatial proteomic techniques have been limited to linear multiplexing capacity thus far. As a pioneering effort to overcome this hurdle, we demonstrated that our novel approach for proteomic mapping enables the implementation of combinatorial barcoding strategies for exponential multiplexing capacity by implementing stochastic sparse labelling of protein targets. While others have attempted sparse protein labelling using nucleic acid tags[77], to our knowledge, this is the first instance of successful stochastic immunolabelling for proteomic mapping.

In addition to improved multiplexity, mapping spatial proteomic distribution using barcoding based methods grants further advantages. All DNA-oligo conjugated antibodies can be labeled at one shot, reducing handling time and effort. Tissue deformation and antigen damage commonly associated to antibody staining-destaining iterations are alleviated since only initiators and HCR hairpins are recycled in each round, which do not require high temperature or strong detergents. The variance in signal abundance between proteins with different expression level is narrowed in the context of stochastic sparse labeling, which avoids signal dominance/crowding when dealing with highly copy number proteins.

Chapter 4. Comparative cellular profiling and pathological analysis of Alzheimer's Disease in human brains enabled by spatial proteomic mapping platform

4.1 Introduction

In order to reveal the underlying molecular and cellular mechanisms driving disease progression, obtaining the spatially resolved proteome of human brains is one of the promising approaches as well as ultimate objectives for medical research. In particular, the therapeutic treatments of Alzheimer’s Disease, most of which aim to reduce the deposition of its hallmark pathological peptides/proteins (amyloid beta and pTau), remained less effective as predicted, potentially suggesting unrecognized mechanisms to be discovered. Since the development and implementation of single cell level spatial genomics technologies, high resolution comparative analysis of complex human brain tissues was enabled between AD and control[78–82]. However, the lack of an integrated technological platform simultaneously allowing 3D capturing of pathological features, tolerance to differently conditioned brain tissues, and high resolution characterization of cellular profiles still limited the comprehensive understanding of AD on molecular level.

In the previous chapter, we verified the feasibility of implementing the model-predicted modulation of antibody binding kinetics in practice. We confirmed the performance of our spatial proteomic mapping platform on volumetric tissues, and for the first time showed the compatibility of proteomic detection to combinatorial barcoding strategy widely used in spatial transcriptomics technologies. In this chapter, we displayed the potential of our spatial proteomic platform by performing detailed cellular profiling, pathological investigation and structural characterization on multiple regions of long banked human brain samples diagnosed with Alzheimer’s Disease.

4.2 Results

4.2.1 Region-specific neuronal loss in Alzheimer's Disease human brain

To demonstrate the potential of our spatial proteomic mapping platform, we performed a comparative analysis of brain samples from patients diagnosed with Alzheimer's Disease and healthy controls. To enable investigation of cell type and morphology, AD-related pathological signs and their association, the dense labeling strategy was selected. Corresponding thick tissue samples from orbitofrontal cortex (OFC) and prefrontal cortex (PFC) were pre-processed and a one-shot labeling strategy was used for all conjugated primary antibodies to obtain spatial profiles of a set of commonly used markers for inhibitory interneurons, microglia and astrocytes, as well as AD-associated pathological markers. High-resolution images were acquired by spinning disk confocal microscopy with a 25X objective (**Figure 4-1**), and co-registered at single cell resolution based on nuclear staining (**Methods**). Consistent with previous reports of atrophy as consequence of AD pathology[83], a significant decrease (35% for OFC, 42% for PFC) in the cortical thickness in the AD-derived samples was observed (**Figure 4-2 b**).

Leveraging our platform capacity for high-resolution multiplexed proteomic characterization, an initial, proof-of-concept cellular level evaluation of the effect of AD on tissue architecture was performed on corresponding sub volumes encompassing comparable cortical regions (pial surface to white matter) in OFC and PFC (**Figure 4-2 a**). Previous efforts have provided region-dependent, inconsistent results for the effect of AD pathology in the abundance and distribution of inhibitory neurons[84–93]. Focusing on major groups of interneurons functionally characterized by the expression of calcium binding proteins, including parvalbumin (PV), calbindin D28k (CB) and calretinin (CR), a 66% (OFC) and 47% (PFC) decrease in the number of detected cells (PV+, CR+, CB+, PV+/CB+, PV+/CR+) was observed. In particular, PV+ and CR+ neurons showed a disproportionate reduction compared to neurons expressing CB), suggesting higher susceptibility to AD pathology (**Figure 4-2 c**). Interestingly, neurons co-expressing PV and CR showed negligible loss in AD samples (**Figure 4-2 c**). Taking advantage of the uniformed, dense cell-body labeling strategy used, we further investigated the effect of AD in cellular architecture by evaluating the cell body volume distribution of PV+ and CR+ cells (**Figure 4-2 d**). Consistent with previous observations[94–98], a significantly reduced distribution of cell body volume was observed in AD-derived samples for both cell types. Finally, the cell density and relative percentage of subpopulations of neurons expressing calcium binding proteins across the cortex layers were compared (**Figure 4-2 e and Figure 4-3**). Consistent cell distribution patterns were observed in both brain subregions: CR+ neurons were mainly located in layer I, II and III; CB+ neurons in layer II and III; PV+ neurons in layer III, IV, and V. While there was no evidence of preferential loss or susceptibility in cortical layers, the decrease in cell density was sharper in the OFC regions, consistent with previous reports[99,100].

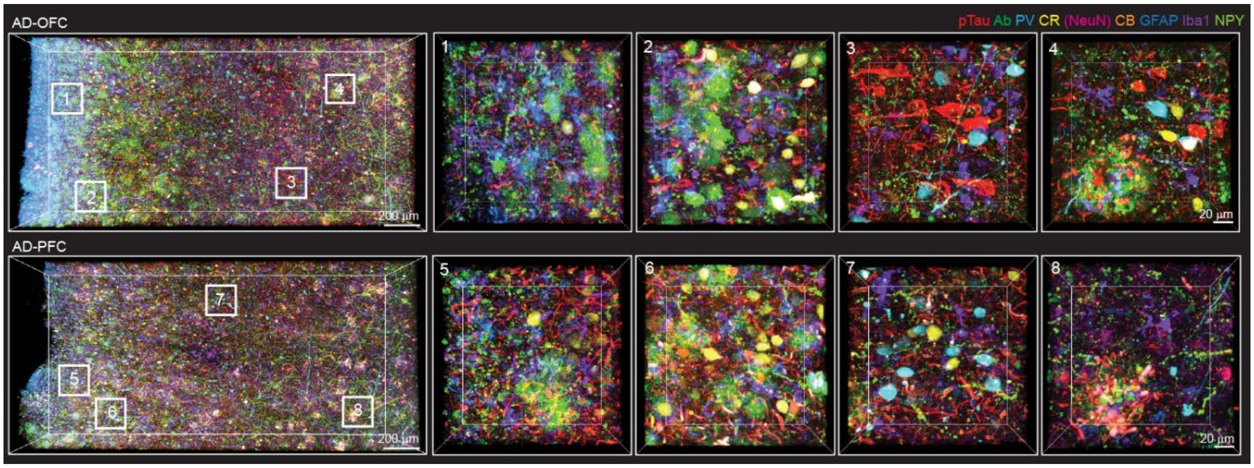

Figure 4-1. Overlayed 3D representation of spatial proteomic detection on orbitofrontal cortex (OFC) and prefrontal cortex (PFC) of human brain samples with Alzheimer's Disease. The multi-channel, multi-round images from one shot labeling with all relevant antibodies via Andor Dragonfly Spinning Disk Microscope with 25x objective (Leica HCX IRAPO L 25x/0.95 W). Zoom-in images show the high resolution image setting of our datasets, enabling cellular and subcellular analysis of proteins.

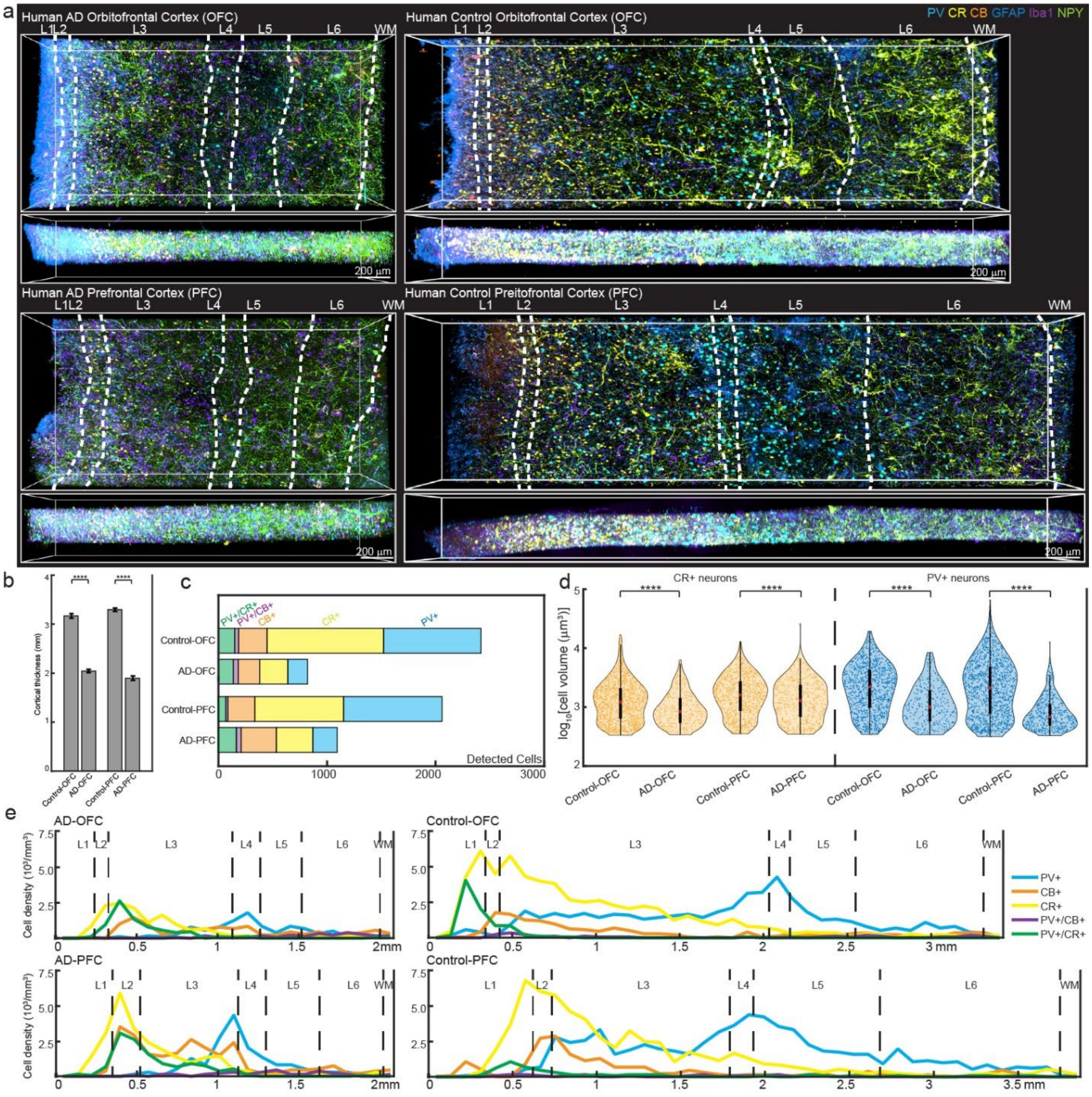

Figure 4-2. Region-matched comparative cell profiling of human brain samples with Alzheimer's Disease is realized on thick tissues. (**a**) 3D representation of cell type marker labeling on orbitofrontal cortex (OFC) and prefrontal cortex (PFC) of human brain samples with Alzheimer's Disease and control. Images are computationally stitched, warped and co-aligned based on the signals from nuclei channel. Cortical layers (dashed lines) are manually segmented based on regional features of cell density, shape and size. (**b**) Measurement of cortical thickness of OFC and PFC of AD and control human brain samples. AD-associated cortical atrophy is observed in in both OFC and PFC of the AD brain samples (two-sample Kolmogorov-Smirnov test, **** P ≤ 0.0001). (**c**) Total number and cellular composition of calcium binding protein expressing inhibitory interneurons detected in the human brain samples. Disproportional neuronal loss is observed among

different categories of inhibitory neurons. (**d**) Cell volume distribution of calretinin (CR) and parvalbumin (PV) positive neurons from AD and control brains. Significantly decreased cell sizes are observed in in both OFC and PFC of the AD brain samples (two-sample Kolmogorov-Smirnov test, **** P ≤ 0.0001). (**e**) Spatial profiling of calcium binding protein expressing neuronal densities from pial surface to white matter is enabled by high resolution imaging.

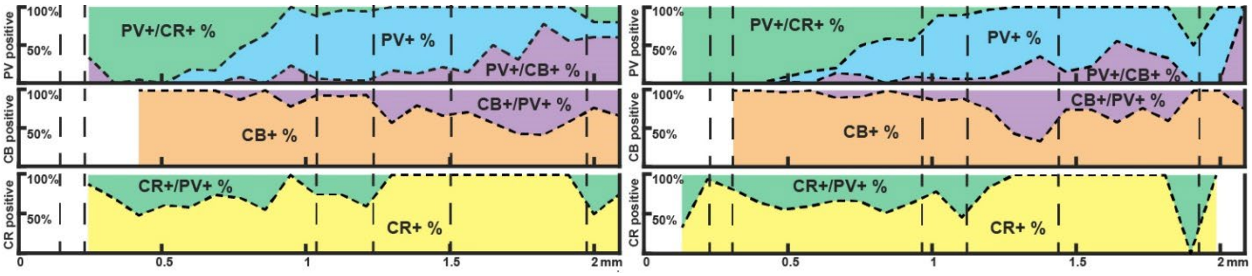

Figure 4-3. Co-expressing analysis of PV, CB, and CR in inhibitory neurons from pial surface to white matter. Percentages of cell subpopulations expressing one or more of calcium binding proteins are calculated and plotted in perpendicular direction to cortical layers.

4.2.2 3D quantitative characterization of Alzheimer's Disease pathology

Accumulation of pTau and amyloid beta (Aβ) are hallmarks of AD pathology, yet they were often studied or characterized in 2D or thin tissue slices[101–105]. To improve our understanding of the effect of AD on tissue architecture and composition, the 3D distribution and morphology of pTau and Aβ plaques were characterized at high resolution, as well as their association with microglia and axons. Volumetric imaging enabled the capture of whole plaques in the context of their cortical localization (**Figure 4-4 a**), and precise morphological evaluation without biases associated with incomplete capture in thin slices (**Figure 4-4 b**). Quantitative analysis of the density, size and morphology of NFTs and Aβ plaques along the cortical axis was performed (**Figure 4-4 c,d**). Consistent with previous reports for heavier pathological burden in OFC[99,106], a higher density for both markers was observed in this region, particularly in upper cortical layers. Notably, a major contributor to the plaque density difference in OFC was a higher occurrence of diffuse plaques stacking in layer I to III.

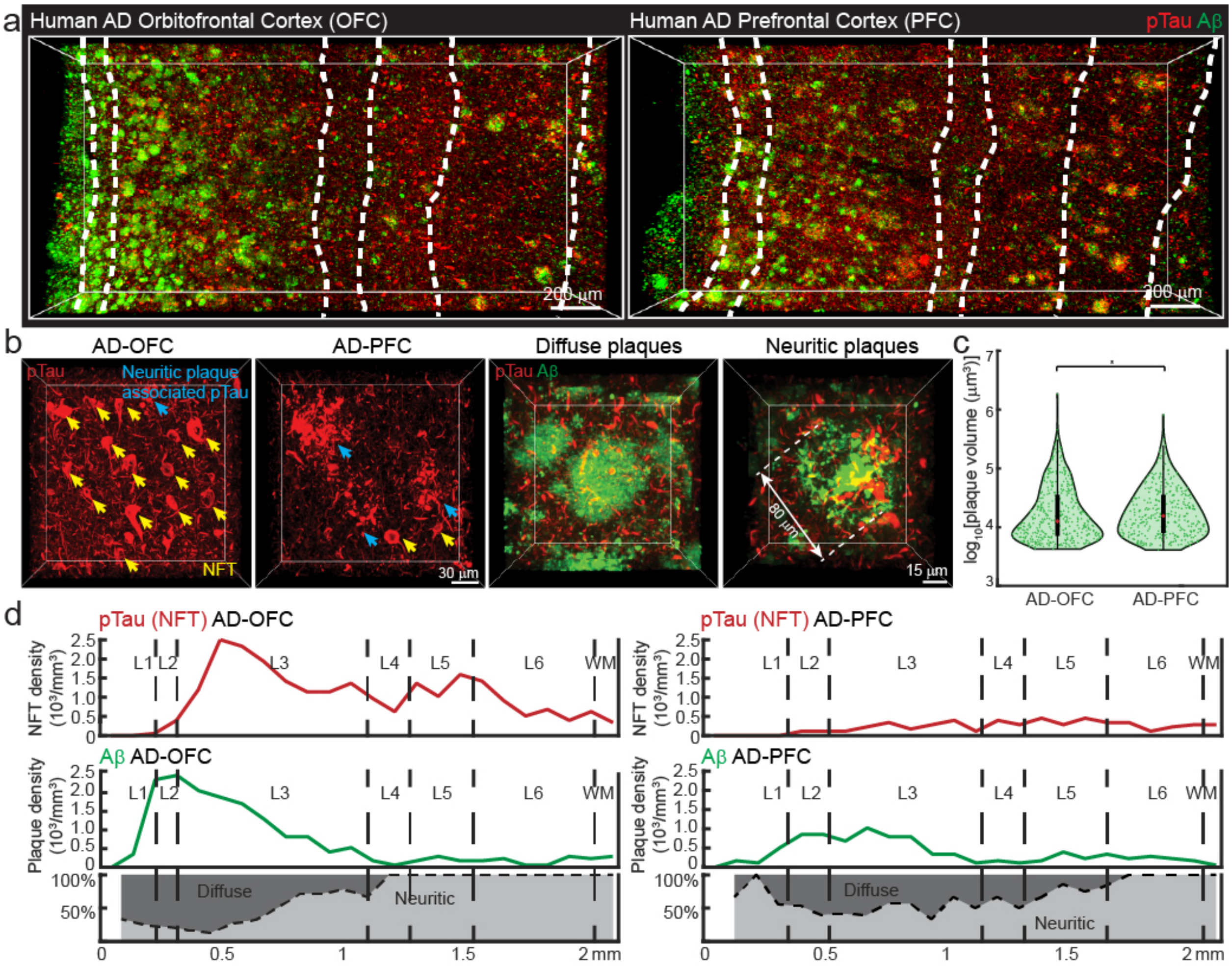

Figure 4-4. Characterization of Alzheimer's Disease associated pathology at cellular resolution. (**a**) 3D representation of AD pathological marker signals from orbitofrontal cortex (OFC) and prefrontal cortex (PFC) of human AD brain samples. Images are acquired via Andor Dragonfly Spinning Disk Microscope with 25x objective (Leica HCX IRAPO L 25x/0.95 W). Cortical layers (dashed lines) are manually segmented based on regional features of cell density, shape and size. (**b**) Example images of classic morphology of pTau positive and amyloid beta positive pathological structures. pTau positive neurofibrillary tangles (NFTs) and neuritic plaque associated pTau signals are pointed out by arrows of different colors. Examples of a diffuse plaque and a neuritic plaque are shown accordingly. (**c**) Amyloid plaque volume distribution in OFC and PFC of AD brain samples. Two-sample Kolmogorov-Smirnov test, * $P \leq 0.05$. (**d**) Spatial profiling of the density of neurofibrillary tangles and amyloid plaques in OFC and PFC regions. Manual classification and annotation of NFTs, diffuse plaques and neuritic plaques are allowed based on the high resolution imaging through spatial proteomic mapping platform. Percentages of diffuse and neuritic plaques are calculated and displayed alongside the spatial profile of amyloid plaques.

4.2.3 Spatial dependence between brain-resident immune system and Alzheimer’s Disease pathology

The association of AD pathological hallmarks (Aβ and pTau accumulation) and the immune system has been commonly pointed out as a key element in disease progression[107]. To highlight the power of our 3D spatial proteomic platform we performed a detailed examination of the interactions between immune components and AD pathological hallmarks leveraging our high resolution, uniformly stained, multiplexed 3D datasets. Automated detection and segmentation of Iba1+ microglia and NPY+ structures (soma and axons) in the context of the previously described AD hallmarks were performed to study the interplay between microglia, the primary brain-resident immune cell[108–112], and NPY, a neuropeptide considered to be an important modulator of M2 microglia activation[113].

Examination of the NPY signal revealed a partitioning with very sparse soma per evaluated volume (<15 total identified soma per sample, **Figure 4-5 b**), and the majority of dense signal associated to axons. Due to the scarcity of labeled soma, for quantification purposes the NPY signals refer to axonal from here onwards. Evaluation of the density profile of Iba1+ microglia and NPY+ axons along the cortical layers (**Figure 4-5 a**) revealed an increased abundance of both microglia and NPY+ axons in Aβ-rich regions in the AD tissue, particularly within layer I to III, a pattern mirroring that of Aβ plaques (**Figure 4-5 e**). A positive correlation between the distribution of Iba1+ microglia and Aβ accumulation was detected for both OFC ($R = 0.8141$, $p \leq 0.0001$) and PFC ($R = 0.8313$, $p \leq 0.0001$) regions in AD tissue (**Figure 4-5 d**) as previously observed[114]. Contrary to the AD-associated reduction in cell volume for interneurons reported above, microglia cell volume showed a significant increase in both OFC and PFC regions (**Figure 4-5 c**). This change in apparent size is consistent with previous observations on the morphological change associated with aging and disease states[115–118], suggesting AD pathology-associated immune activation. Interestingly, the observation of increased density of axonal NPY in Aβ-rich regions of AD tissues, was unexpected in human tissues. Though similar phenotypes have been reported in the cerebral cortex and hippocampus of mouse brains[119,120], only reduced level of NPY immunoreactivity has been previously reported in human brains[121–125].

To further investigate the increased NPY density in axonal fibers in Aβ-rich regions observed in AD, the spatial relationship between amyloid plaques, NPY+ axons and microglia was evaluated by projecting the intensity level of Aβ in regions segmented as NPY+ axons and microglia (**Figure 4-6 a**). Using this approach, plaque-associated microglia and NPY+ axons, defined as those with full or partial spatial overlap with plaques, could be detected (**Figure 4-6 b**), detailed examination of the fiber segments detected inside plaques revealed axonal swelling. A phenotype previously proposed to act as a trigger for Aβ plaque formation[122,126]. To determine their proportion, an arbitrary threshold of > 2 geometric standard deviation above the geometric mean of Aβ intensity was set to classify NPY+ axons and microglia as plaque-associated vs not plaque-associated. Across the entire volumes, 20-30% of the microglia and NPY+ axons were detected in association with plaques (**Figure 4-6 c**). When evaluated along the cortical column, the number of plaque-associated microglia and NPY+ axons tracked the Aβ abundance, suggesting a proportional recruitment of microglia and NPY+ axons (**Figure 4-6 d)** further indicating an immunological feedback mechanism may be at play.

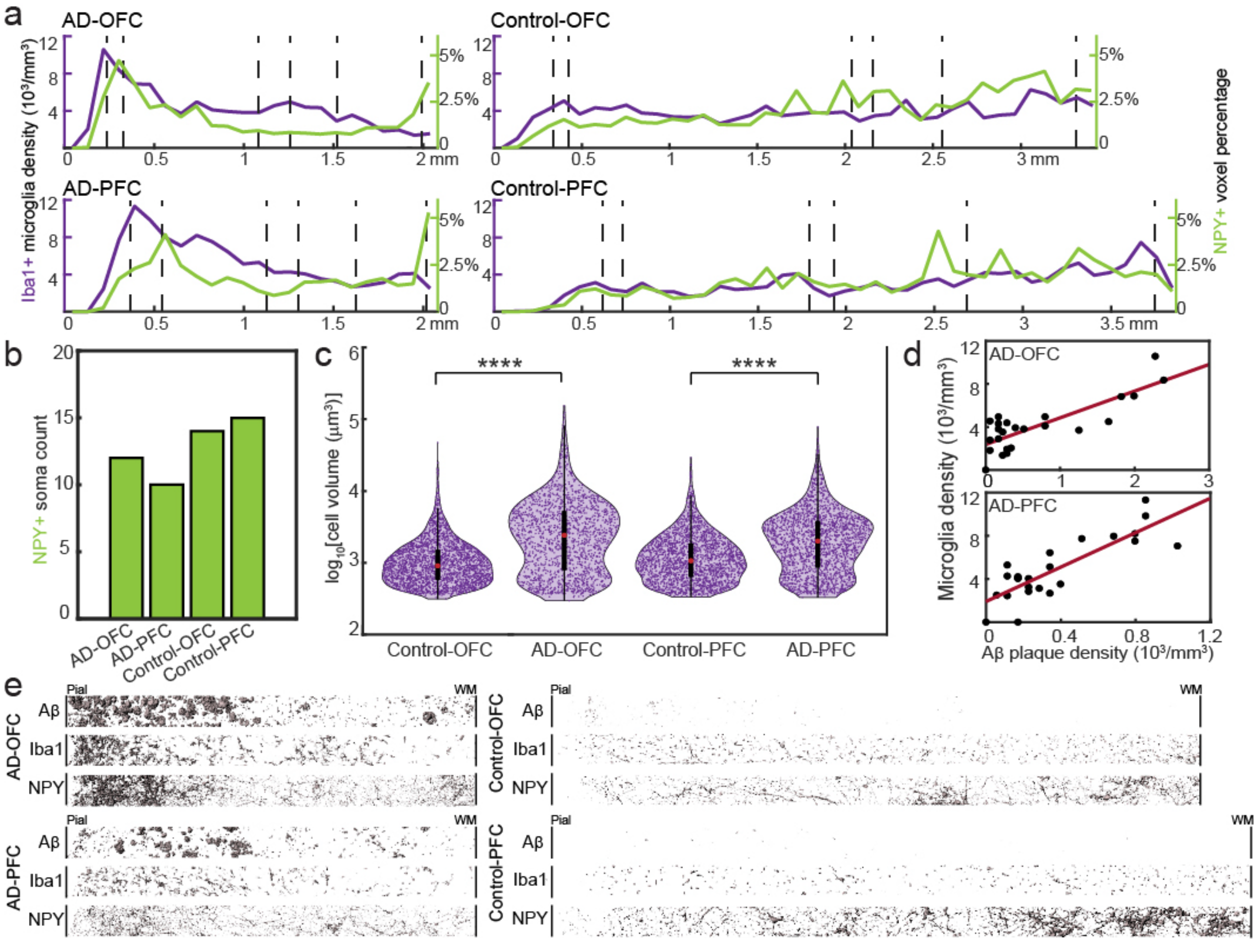

Figure 4-5. Characterization of the spatial dependence between brain-resident immune system and Alzheimer's Disease associated pathology. (**a**) Spatial profiling of detected densities of Iba1+ microglia and NPY+ axons from pial surface to white matter in AD and control brain samples. (**b**) Soma count of NPY+ neurons. (**c**) Cell volume distribution of Iba1+ microglia from AD and control brains. A population of microglia with significantly increased sizes is observed in both OFC and PFC of the AD brain samples (two-sample Kolmogorov-Smirnov test, **** $P \leq 0.0001$). (**d**) Correlation tests between distributions of amyloid plaque density and microglia density in OFC and PFC of AD brains. (**e**) Side-by-side comparison of amyloid plaques, Iba1+ microglia and NPY+ axons distributions in OFC and PFC of AD and control brains.

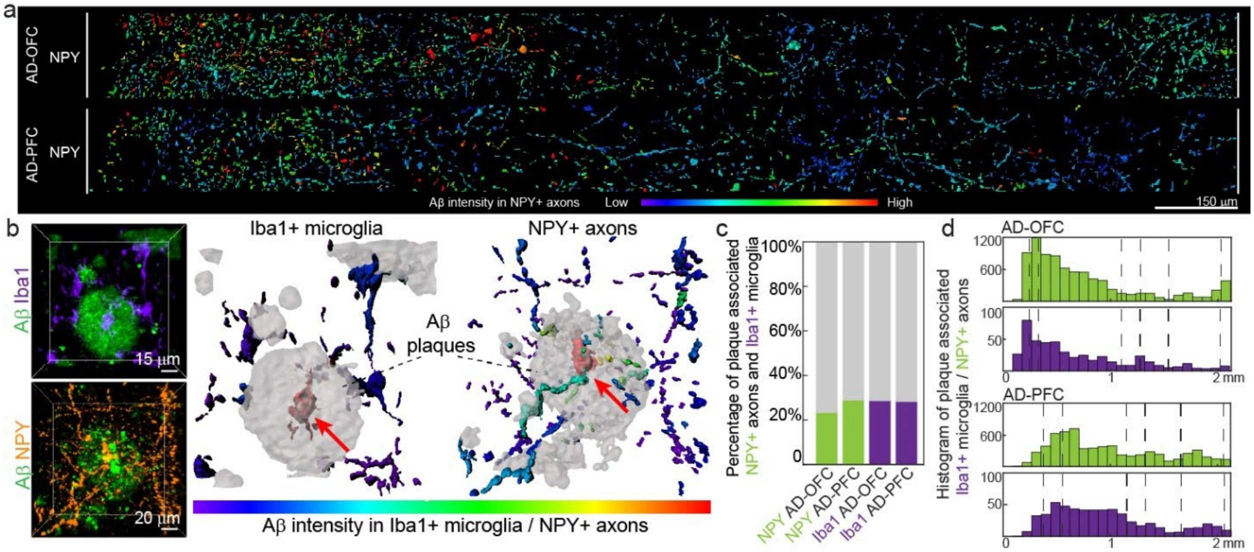

Figure 4-6. Classification of AD pathology associated cells and axons enabled by high resolution proteomic mapping. (**a**) Spatial map of detected NPY+ axons with projected intensity of amyloid plaque channel in OFC and PFC of AD human brain samples. (**b**) Representative images of plaque associated Iba1+ microglia and NPY+ axons. Examples of Iba1+ microglia and NPY+ axons were found inside amyloid plaques (pointed by red arrows), with the terminal of NPY+ axon swollen. (**c**) Proportion of plaque associated Iba1+ microglia and NPY+ axons in OFC and PFC of AD and control human brains. A threshold of > 2 geometric standard deviation above the geometric mean of Aβ intensity was used. (**d**) Histogram of plaque associated Iba1+ microglia and NPY+ axons with respect to spatial coordinates. A threshold of > 2 geometric standard deviation above the geometric mean of Aβ intensity was used.

4.2.4 Axonal connectivity features affected by Alzheimer's Disease pathology

Volumetric imaging also enabled the capture and evaluation of higher order connectivity features, such as axonal arborization and axonal orientation in the context of AD pathology, highlighting the need for multiscale analysis. Understanding the function of these structures, as well as their association with disease will require a detailed view of their interacting partners. As a demonstration of the potential of our technology to study complex neuronal networks, here we present a high-resolution reconstruction of a NPY+ neuron, covering dendrites, soma, axon and its projection to an axonal arborization[127,128], detected across hundreds of micrometers in each dimension (**Figure 4-7 a**), exceeding the length scale of any thin slice approach. Further inspection of these arborization structures within the sampled volumes revealed reduced size in the AD cases (**Figure 4-7 b**). Finally, although the highest density of PV+ soma was observed around layer IV, we noticed structural variation in the PV+ axonal network between AD and control tissues, most strikingly at the interface between layer VI and white matter (**Figure 4-7 c**). Directionality analysis in this region revealed a clear shift in the structural orientation of the PV+ axonal network (**Figure 4-7 d**), from predominantly perpendicular to the axis defined by white matter/pial surface (denoted as 90 and -90 degrees in the plot), a pattern that was consistent across the tissue volume (z-axis), to a less defined case with a strong signal at parallel orientation (0 degrees) and variability across z. To validate that this phenotype was not due to variation in the orientation in which the samples were obtained, the same analysis was performed on the pTau channel on the AD tissues (**Figure 4-7 d**). Due to the degree of AD-progression, this channel served as pan-axonal marker and showed a directionality pattern consistent with the control case, suggesting that the observed changes were specific to PV-associated fiber networks. Given the central role of PV+ neurons in regulating network oscillations and shaping the encoding, consolidation and retrieval of memories[129], this reconfiguration of the PV+ axonal network may have significant implications in AD-associated changes in connectivity and inter-regional communications.

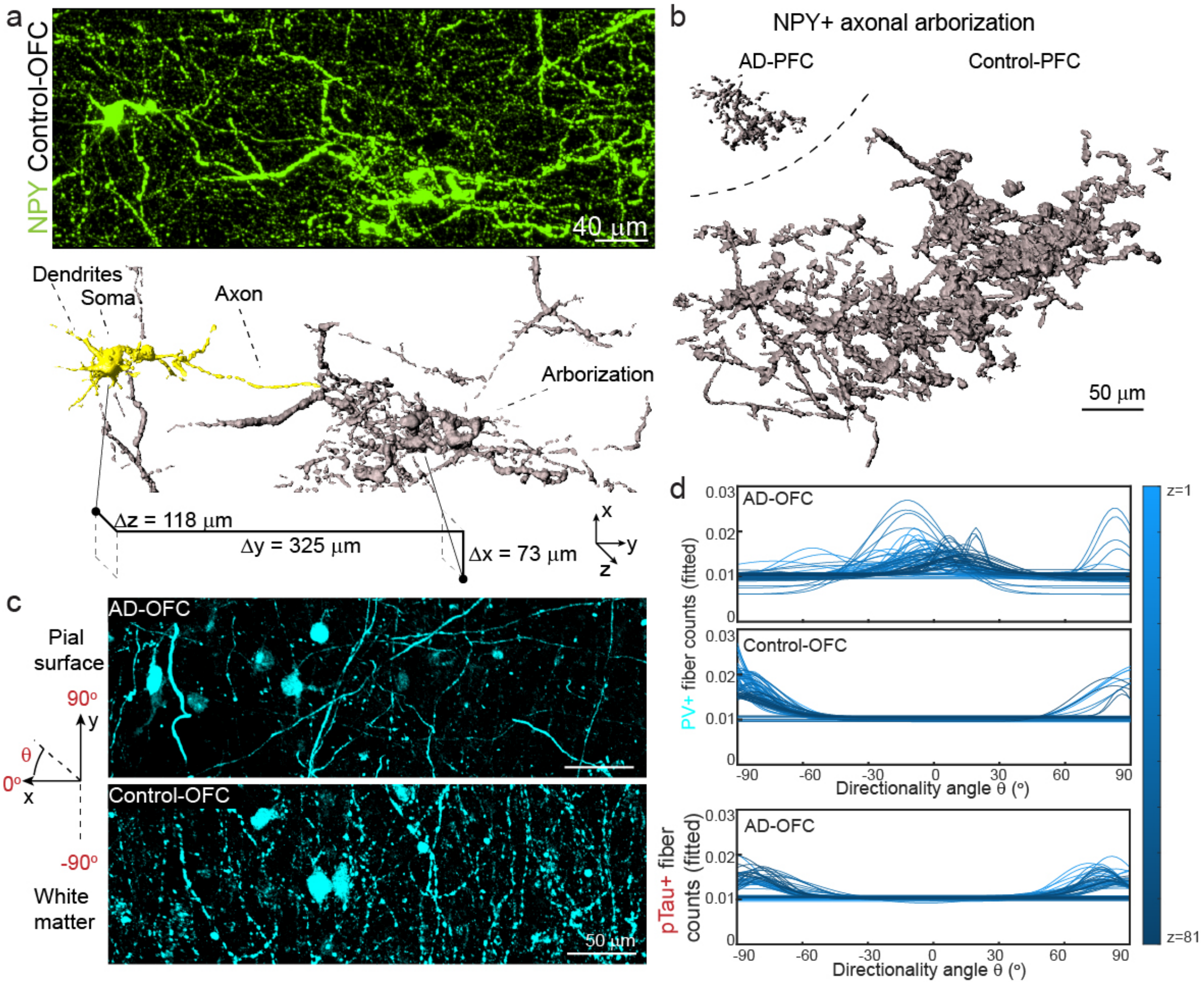

Figure 4-7. Comparative analysis of the effect of AD pathology on axonal connectivity features. (**a**) Example of an NPY+ neuron with axonal arborization structure found in OFC of control human brain. (**b**) Comparison of the size of NPY+ axonal arborization structure between AD and control brains. (**c**) Maximum z projection of PV+ neurons and axons at the grey matter-white matter interface in the OFC of AD and control brains. (**d**) Fourier based directionality analysis of PV+ fibers in the OFC of AD and control brains. As a comparison, same analysis was performed on pTau+ fibers in the OFC of AD brain.

4.3 Methods

4.3.1 Preparation of human brain samples

Postmortem human brain tissues were obtained from the Massachusetts General Hospital (MGH) brain bank. The brain tissues were manually cut into small blocks using a razor blade and sectioned into 200 um thick slices using a vibratome (LEICA VT 1200S). A polyepoxide solution for SHILED processing was prepared by dissolving 2 w/v% polyglycerol 3-polyglycidyl ether (P3PE, product name ERISYS GE38 PAIL, 51115140, Emerald) in 0.05 M Sodium Carbonate (S7795, MilliporeSigma, St. Louis, MO, USA) and 0.05 M Sodium Bicarbonate buffer (S5761, MilliporeSigma). The solution was thoroughly vortexed for 1 minute, centrifuged for 10 min at 7200g at 4 ^{o}C, and the supernatant was collected. The sectioned human brain slices were incubated in the polyepoxide solution in the cold room (4 ^{o}C) overnight and then transferred to the shaker at room temperature to initiate crosslinking reaction. After 24 hours, the SHIELD-processed tissues were washed with 1XPBST (0.2%) for 0.5-1 days to remove the remaining GE38 molecules inside tissues. The tissues were permeabilized and delipidated in the SDS solution (0.2 M, pH 9) at 80 ^{o}C for 1 day and then washed with 1XPBST (0.2%) to remove the remaining SDS molecules.

4.3.2 Multiround alignment of images of human brain samples

Each subsequent round of multi-channel imaging was registered to the same space as the first round by adapting the workflow of UNSLICE[61], described in more detail previously. Instead of using blood vessel endpoints as features, we use detected cell centers in the nuclear stain channel (POPO1). Briefly, some manual anchor points (representing cell centers) that match between two rounds of staining are selected and used to define an initial warping. Additionally, automated blob detection is run to detect cells in each image by using a difference-of-Gaussians (DoG) blob detection algorithm. An intensity threshold of 100 and minimum distance threshold of 10 microns were set to filter out local maxima that are too dim or too close together. Then, the automatically detected cell centers in each image are matched using a geographic nearest-neighbors matching algorithm that maximizes how much better a correspondence is over other candidate correspondences in the same region based on how well the constellation of nearest neighbors match. After outlier removal using RANSAC, these matches are combined with the initial manually labelled correspondences to generate a deformation field with which nonrigid thin plate splines are used to warp the entire image. This process is repeated for all rounds of staining in the same tissue.

4.3.3 Cortical layer segmentation of human brain samples

Cortical layers were segmented based on regional features of cytoarchitecture[130,131], such as cell density, shape, and size, based on nuclei and NeuN staining. Layer I-VI, white matter (WM) boundaries were manually identified and visualized using imageJ.

4.3.4 Thresholding based cell/axon detection using Imaris

3D image volumes and their representations were made using the Imaris software. The cellular and axonal detection, 3D intensity map, and volume measurements were facilitated by the surface function in Imaris software.

4.3.5 Fourier component based directionality analysis

The Directionality Plugin of ImageJ (https://imagej.net/plugins/directionality) was used to analyze the stacked images of AD and control brains.

4.4 Conclusion and discussion

To fully showcase the value of the proteomic mapping platform proposed in this work, we decided to pursue the characterization of biological features that are hard to access with conventional methods. In the context of Alzheimer's disease, the presence and morphological features of amyloid and pTau plaques have been associated with disease diagnostics and progression[83]. However, the size of them can often exceed the dimensional limits for existing proteomic platforms (5-40 um thickness), leading to incomplete or biased results and inferences. Leveraging our dense proteomic labelling modality, we were able to characterize and quantify entire amyloid plaques with diameter ranging from tens to hundreds of micrometers in human brains diagnosed with Alzheimer's Disease, providing an unprecedented and unbiased view of this important pathological signs in their native context.

As demonstrated previously ([61,62,132], Choi, et al. in preparation), volumetric analysis reduces biases associated with the determination of cellular composition and evaluation of cytoarchitecture using thin sections. Taking advantage of the high-resolution, uniformly labeled images, a comparative 3D analysis of the spatial distribution of a set of inhibitory neurons subtypes (PV+, CB+, CR+) between healthy and AD tissues was performed. The region-specific, comparative data revealed changes in their abundance, density and size, as well as variation in their cortical profiles in response to disease, consistent with previous reports[84–86,88–93], highlighting the accuracy and robustness of our results. Noteworthy, our volumetric strategy enabled the capture and characterization of the distribution of NPY+ neurons, whose soma is much more sparse than processes. Though they are recognized to be important for neuroendocrine functions, memory processing, as well as other regulations[133], soma of NPY+ neurons can easily be missed or miscounted using 2D methods due to their sparsity (**Figure 4-5 b**). Additionally, evaluation of glial types revealed patterns of dense, long, unbranched processes of interlaminar astrocytes (GFAP+) in upper layers of healthy human brain samples[134], consistent with reports from other spatial proteomics platform[61], yet evaluated in 3D providing a more comprehensive view. These unbranched processes were not observed in AD-derived brain samples consistent with compromised pial structure in atrophied tissue[135]. In addition to cell detection and profiling, the high resolution 3D protein map generated by our platform enabled the quantitative evaluation of spatial dependence between microglia and AD pathology signatures. A positive correlation between microglia presence and amyloid plaques was observed, consistent with their role in the accumulation, maintenance and clearance of amyloid deposits[107–111,114] highlighting the power of quantitative analysis on 3D data.

Chapter 5. Three dimensional in situ functional detection of proteins enabled by mechanical interlocking

5.1 Introduction

Biochemical processes, including enzymatic reaction, molecular recognition, signaling and modulations, relies on intermolecular reactions such as the formation of covalent bonds, hydrogen bonds, ionic bonds, or hydrophobic interactions between subdomains of binding sites. Therefore, functionality investigation requires both information of spatial distribution and preservation of binding sites. In fixed tissues processed through the method of commonly used aldehyde fixation, all these interactions are inevitably weakened due to the chemical modification of binding sites (**Figure 5-1 b**). In contrast, as we propose mechanical interlocking, we expect the entanglement between polymer chains and the secondary structures of biomolecules will preserve biomolecules and their functionality with minimal chemical modifications to binding sites.

The key mechanism to realize permanent mechanical interlocking of biomolecules in free solution, cells and tissue context is the interlocking effect of polymer chains in dense hydrogel (**Figure 5-1 a**). After freshly perfused and dissected from animal, the tissues were firstly equilibrated with a concentrated monomer solution that contains monomer, crosslinker and thermal initiators. After complete equilibration, polymerization was slowly initiated at a low temperature to avoid denaturation and degradation. During this process, biomolecules with complex secondary structures (e.g. proteins, DNAs, RNAs) would be intermingled with dense polymer chains.

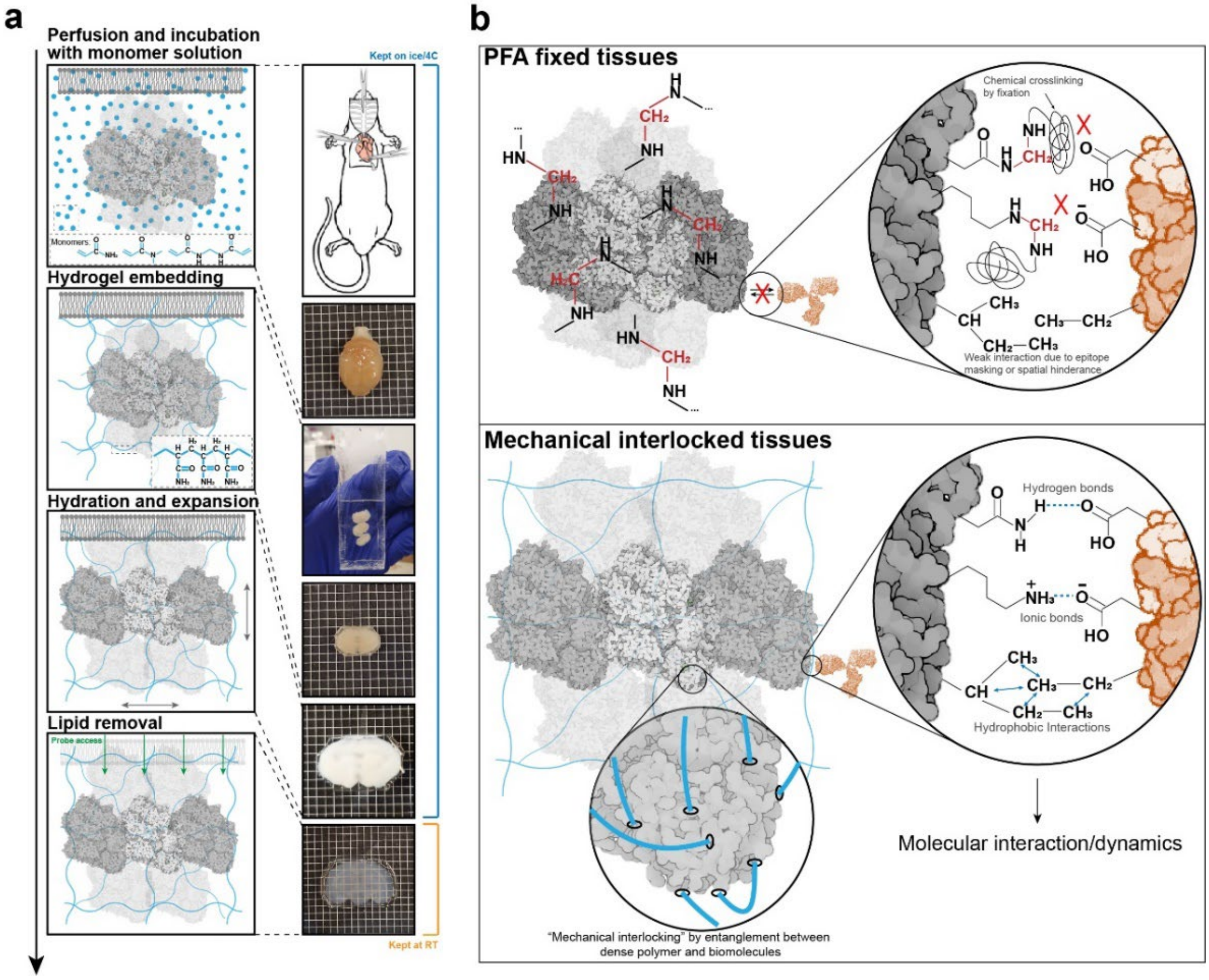

Figure 5-1. Mechanical interlocking enables preservation of biomolecular interaction. (**a**) Pipeline of preservation of biomolecules via mechanical interlocking. (**b**) Comparative illustrations of the mechanism of chemical fixation and mechanical interlocking.

5.2 Results

5.2.1 Validation of mechanical interlocking effect between dense hydrogel mesh and biomolecules

To verify our hypothesis of mechanical interlocking, we embedded DNA ladder and protein standard following the mechanical interlocking pipeline. Dense polyacrylamide hydrogel with identical composition as mechanical interlocking hydrogel were prepared as media. Biomolecules in the form of freely dispersed solution and embedded hydrogel were subject to electrophoresis (**Figure 5-2 a**). It was observed that DNAs and proteins in the form of free solution migrated along the direction of electric field, while their hydrogel embedded version remained stationary. The result indicated that the interlocking effect did not rely on the trapping effect of small sized pores in dense hydrogel, which was an indirect evidence of the formation of mechanical entanglement between biomolecules and hydrogel mesh. To further explore the possibility of preserving biomolecules within various tissue contexts, biological tissues from multiple organs (i.e. brains, lymph nodes, colons, lungs) were perfused, dissected and embedded following the mechanical interlocking protocol (**Figure 5-2 b**). Organ-specific cell type markers were used to confirm the antigenicity of various protein targets respectively, including immune membrane-bound markers that are known to be sensitive to chemical fixation.

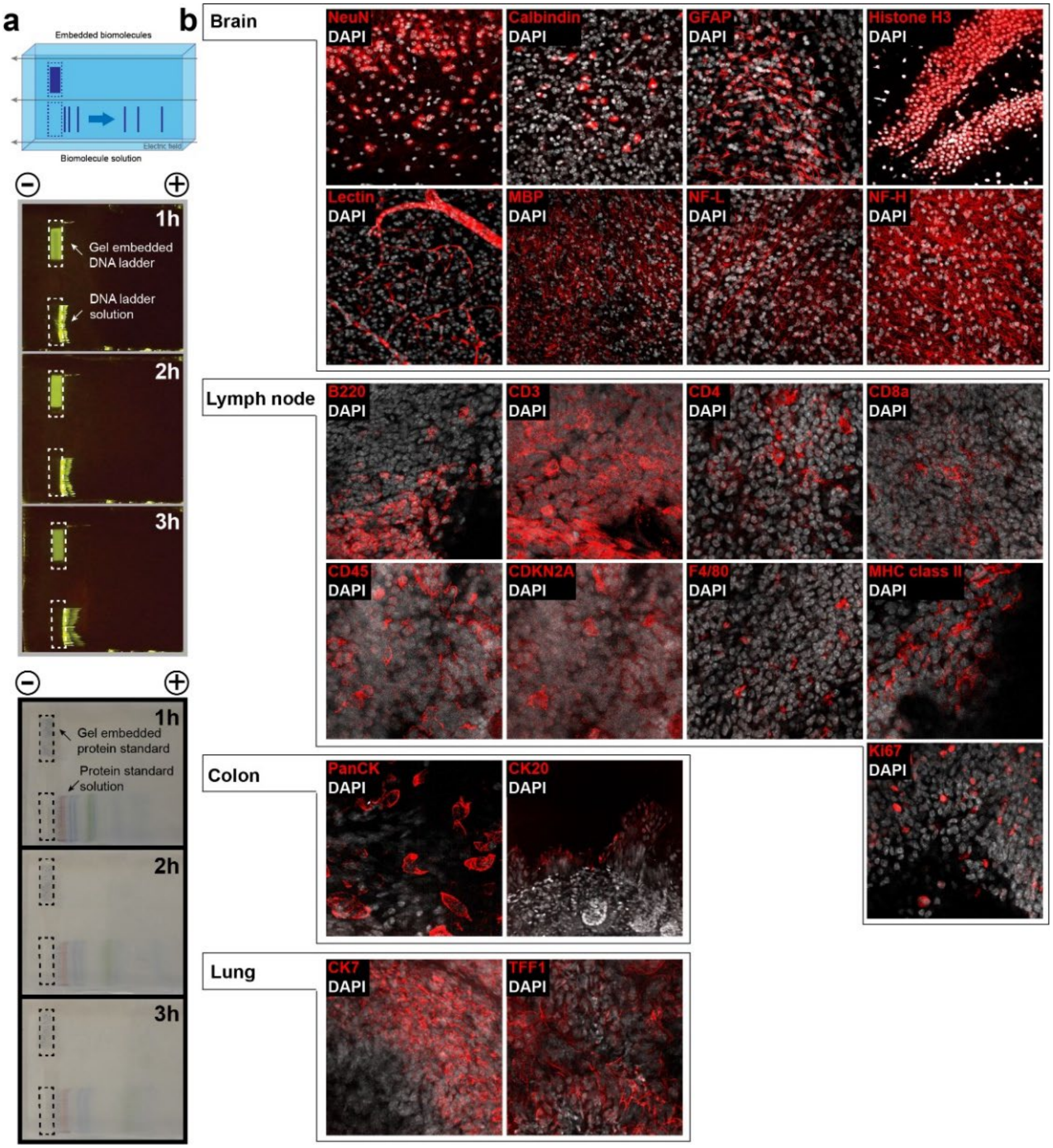

Figure 5-2. Validation of mechanical interlocking effect. (**a**) Electrophoresis confirmed the interlocking effect of biomolecules in mechanical interlocking hydrogels. (**b**) Antigens from various sources of tissues were detected with antibody after embedding in mechanical interlocking hydrogel.

5.2.2 Validation of biomolecular functionality after mechanical interlocking: enzymes and their activity

In order to evaluate the functions of interlocked proteins, the activity of three commonly used enzymes, i.e. horseradish peroxidase, glucose oxidase, and calf intestinal alkaline phosphatase, was tested by respective enzymatic reactions after mechanical interlocking embedding (**Figure 5-3 a,b**). Considerable level of enzymatic activity was observed in samples embedded in mechanical interlocking hydrogel, confirming enzymatic activity is preserved after mechanical interlocking pipeline, whereas no activity was detected in fixative-containing hydrogel. Additionally, no enzymatic activity was detected in the low concentration hydrogel (4% CLARITY gels), where few entanglement could be formed due to insufficient density of polymer chains. To further test the robustness of embedded enzymes after mechanical interlocking pipeline, a piece of glucose oxidase embedded hydrogel was subject to iterative enzymatic reactions (**Figure 5-3 c**), where the colored product indicates the detection of robust glucose oxidase activity.

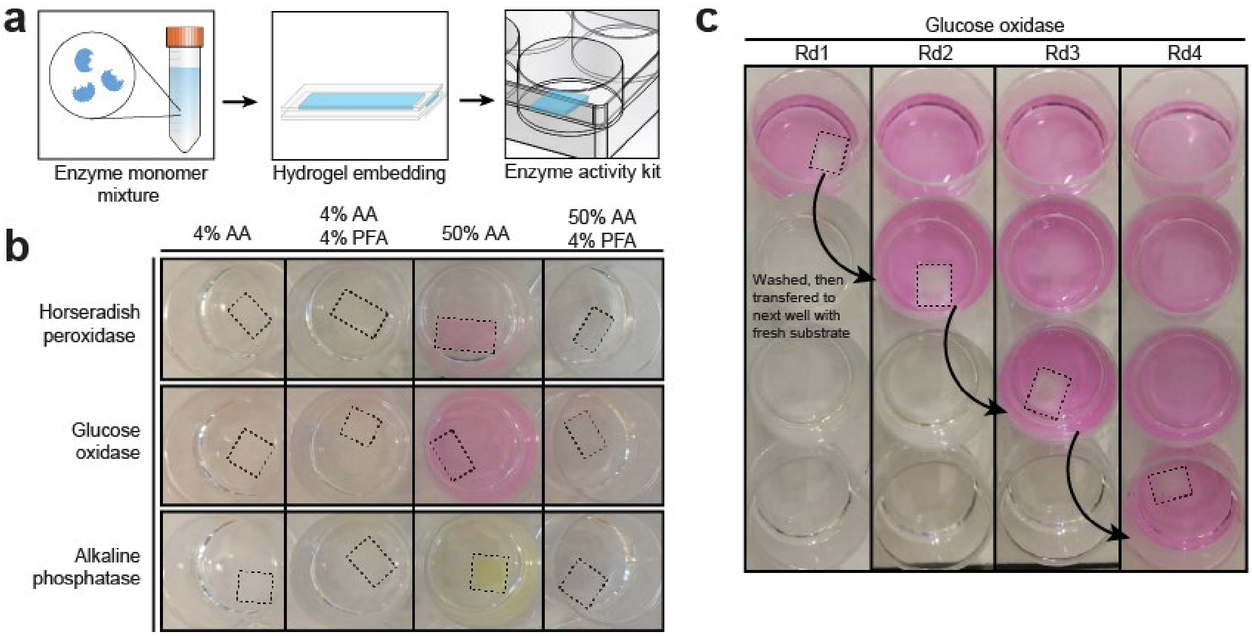

Figure 5-3. Detection of enzymatic activity after mechanical interlocking pipeline. (**a**) Schematic diagram of method to evaluate activity of embedded enzymes. (**b**) Embedded enzymes displayed activity in mechanical interlocking hydrogels. Substrates were added to the embedded enzymes respectively to test the residue activity. (**c**) A piece of glucose oxidase embedded hydrogel was subject to iterative enzymatic reactions.

5.2.3 3D visualization of endogenous proteases in mouse colon with activatable zymography probes enabled by mechanical interlocking

Given that enzymatic activity can be preserved in mechanical interlocking hydrogel, we expected our technology could be used to investigate endogenous enzymatic activities. The dysfunctioning and dysregulation of certain enzymes have been recognized as a crucial marker for diseases such as cancer[136]. Many advanced diagnostics and therapeutics utilize the feature of abnormally high protease activity of cancer for better specificity. In order to profile protease activity within context of tissue microenvironment, activatable zymography probes (AZPs) were designed to spatially resolve the protease activity profile in cancer[41]. However, to date the application of AZPs is still limited to ultra-thin fresh-frozen sections within 10 um.

Therefore, we further investigated whether the spatial distribution and activity profile of endogenous proteases can be obtained with our mechanical interlocking framework. The AZPs were structurally composed of three parts: a negatively charged polyE arm, a positively charged polyR arm, and a substrate linker responsive to active proteases. These protease specific probes remained neutrally charged until the cleavage of their substrate linker by local proteases. As a result, the location of active proteases would be labeled by polyR arm conjugated with a fluorescent reporter due to the electrostatic forces between polyR arm and tissues. As predicted, a clear pattern of protease expression and secretion was observed on 350 um embedded mouse colon tissues (**Figure 5-4**), in contrast to weak or non-specific signals from control groups.

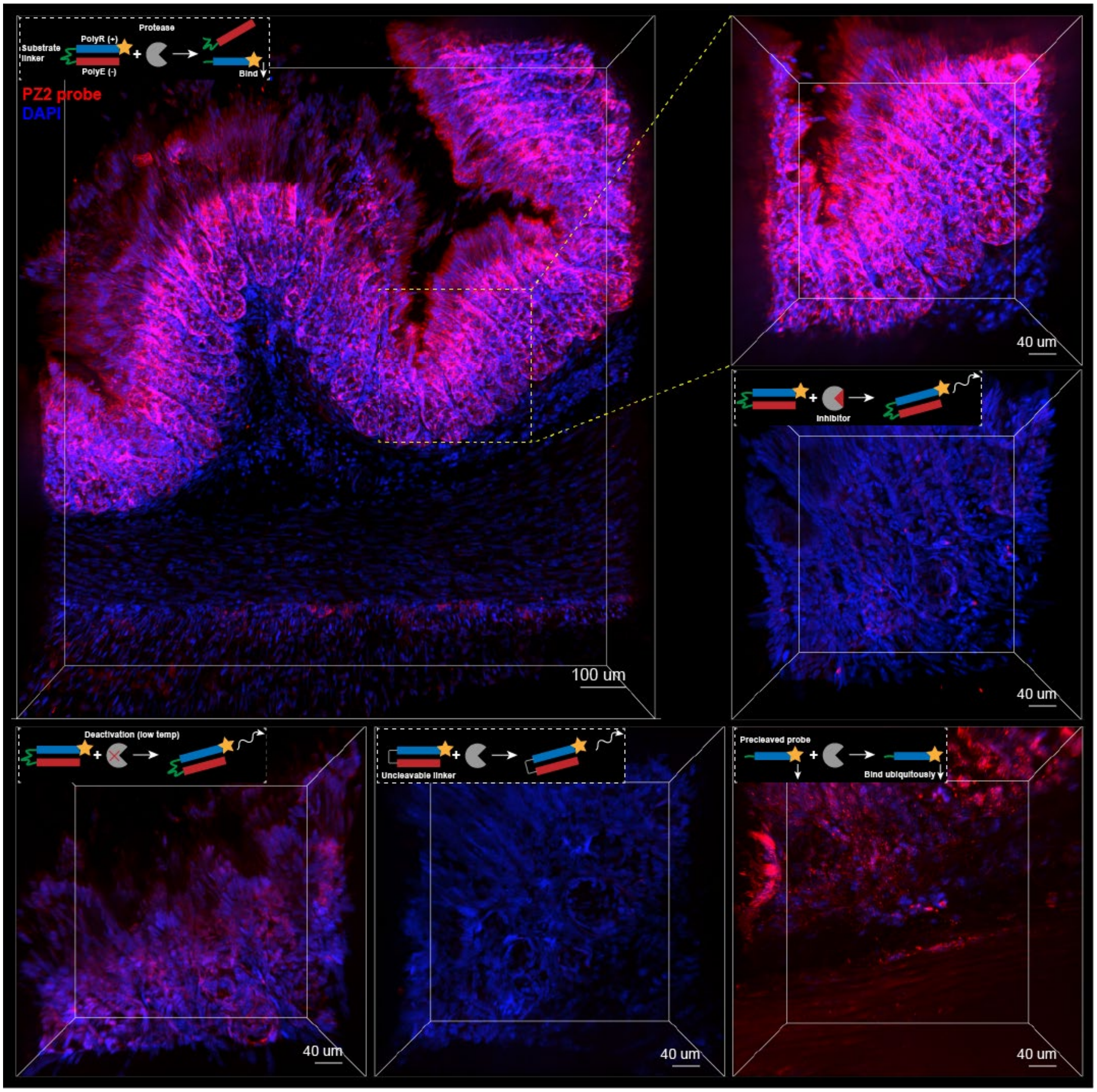

Figure 5-4. 3D visualization of endogenous proteases from volumetric mouse colon tissues incubated with AZP probes.

5.3 Methods

5.3.1 Preparation of mechanical interlocking monomer solution

To make stock solution containing mechanical interlocking monomers, 40% (w/v) acrylamide, 10% (v/v) dimethylacrylamide, 0.01% (w/v) bis-acrylamide were dissolved in DI water. 10X PBS solution was added to the mixture to reach a final concentration of 0.5X PBS. The stock solution above was thoroughly mixed and stored at 4C. Before use, add 2% (w/v) VA-044 (thermal initiator of polymerization) to the ice-cold stock solution. The solution should be kept on ice during the dissolving of VA-044. After the thermal initiator gets completely dissolved, the mechanical interlocking monomer solution is ready to use.

5.3.2 Delivery of mechanical interlocking monomer solution through transcardiac perfusion

Mice were anaesthetized following the standard protocol with FatalPlus, and then were subject to transcardiac perfusion with firstly 40 mL ice-cold 1XPBS with heparin, then 40 mL ice-cold mechanical interlocking monomer solution. Organs (brain, lung, colon, lymph nodes) were dissected and immediately incubated in at least 10 mL ice-cold mechanical interlocking monomer solution for 48 hours at 4C.

5.3.3 Mechanical interlocking hydrogel embedding

After equilibration with mechanical interlocking monomer solutions for 48 hours, tissues were transferred to freshly made ice-cold mechanical interlocking monomer solutions. Then based on the shape and thickness of the tissue, slide glass based embedding sandwich or falcon tubes were used to contain the tissues with extra monomer solution. Polymerization was initiated by nitrogen purging. Tissues were kept on ice for 48 hours until the low temperature polymerization was finished. After hydrogel embedding, tissue-hydrogel hybrids were hydrated in 1XPBS, sliced with vibratome, and delipidated in SDS/NaDC based clearing solutions. Then tissues were ready for immunolabeling.

5.3.4 Hydrogel embedding of enzymes for activity tests

Enzymes (solution form) were mixed with ice-cold mechanical interlocking monomer solution, and incubated on ice for 30 minutes. Then the liquid mixture was transferred into ice-cold slide glass based embedding sandwich. Polymerization was initiated by nitrogen purging. Embedding sandwich was kept on ice for 48 hours until the low temperature polymerization was finished. The resulting hydrogel was hydrated in 1XPBS, and was ready for enzymatic activity tests.

5.3.5 Detection of endogenous proteases in mouse colon with AZPs

Mechanical interlocking tissues of mouse colon were prepared as described above. Tissues were sliced into 350 um slices and were mildly cleared with NaDC based clearing solution at neutral pH for 12 hours at room temperature. After rinsing in 1XPBS, tissues were incubated with BSA and AZP probes at respective conditions to detect enzymatic activity.

5.4 Conclusion and discussion

In summary, we established the pipeline of mechanical interlocking as a platform to enable 3D protein functionality profiling. We proposed and experimentally validated our hypothesis of the entanglement between dense polymer chains and the secondary structures of biomolecules. Tissues from multiple organs with different molecular features were processed with the mechanical interlocking pipeline, and the spatial distributions of characteristic markers were obtained via immunolabeling. Moreover, we proved that, without any aggressive chemical modification, enzymatic activities, as an example of protein functionality, could be preserved with high specificity and robustness. As a proof of concept, we successfully detected the enzymatic activity of endogenous proteases expressed by the epithelial cells in mouse colon tissues, leveraging the ability of 3D in situ protein functionality detection.

Regarding future directions, we anticipate that mechanical interlocking technology can be applied to generate spatial and activity profile of enzymes in tissues other than colons, such as lung, colon, or tissues with tumor lesions. In addition, co-staining between cell type markers and functionality probes, e.g. activatable zymography probes and classic epithelial cell markers on colon tissues, are able to provide spatially resolved functionality map combining molecular and functional information of biomolecules.

Chapter 6. Conclusion and future directions

6.1 Conclusion and discussion

Although current spatial proteomics are able to profile molecular distribution of protein antigens with enhanced efficiency, their volumetric scalability and multiplexing capacity still have considerable room for improvement. Due to the uniqueness of overall higher expression level and greater standard deviation of proteomes, the application of spatial proteomic methods to bulk tissue volumes has been challenging owing to probe depletion during diffusion. Conventional barcoding-based labeling assays require labeling protein targets on ultra-thin tissue sections, typically measuring 5-40 μm in thickness. Saturating all protein targets with an abundant quantity of probes can be accomplished and has been universally employed in practice. However, the same strategy becomes cost-prohibitive and highly empirical for volumetric tissues. In order to saturate proteins with high expression levels, an extremely large amount of antibodies has to be used. Moreover, given the huge inter-molecular and inter-regional variabilities of protein abundance, it is almost impossible to even estimate the precise amount of antibodies necessary for saturation.

Additionally, unlike the nature of mRNAs, the highly expressed proteins are difficult to resolve as single-molecular signals without super-resolution microscopy. Since every cell expresses countless types of proteins simultaneously, the combinatorial barcoding strategy is inapplicable for multiplexed proteomic detection due to the confusion in barcode reading brought by co-expressed proteins. Lacking the compatibility to combinatorial barcoding strategy, barcoding-based spatial proteomics have been limited to linear multiplexing capacity on ultra-thin slices thus far. As a pioneering attempt to address these challenges, we propose our proteomic mapping platform which opens the door to the implementation of combinatorial barcoding strategies for spatial proteomics. Enlightened by the theoretical modeling, our platform enabled unsaturated yet uniform proteomic labeling by balancing the reaction-diffusion process of antibody transport.

Based on the theoretical analysis, our approach to modulate the diffusion-reaction process of antibodies is not sensitive to the type of reaction kinetics. We envision that, as long as the binding reaction order is positive, the conclusions of our proteomic mapping platform are extendable to various types of molecular probes, such as isotypes other than IgG, single domain antibodies, Fab fragments, bispecific antibodies, and antibodies modified with all sorts of conjugation chemistries.

In this study, we have enabled uniform passive protein labeling of cell type markers on the scale of 1 mm thick tissues within 48 hours. To achieve protein labeling on larger volumetric scales, we expect the performance of our method to be equally trustworthy when the balance of rapid diffusion and slow reaction is kept. We are confident that similar level of uniformity will be enabled with our strategy on the scale of several millimeters to centimeters. According to our theoretical reasoning, we estimate the timescale needed for further volumetric scalability increases with respect to the square of tissue thickness.

Aside from the improved volumetric and multiplexing scalability, mapping spatial proteomic distribution using barcoding based methods grants further advantages. As we have demonstrated, all involved DNA oligo conjugated antibodies can be labeled at one shot. Since only initiators and HCR hairpins are recycled in each round, tissue deformation and antigen damage due to antibody staining-destaining iterations are alleviated. Additionally, stochastic sparse labeling, in particular, significantly narrows the variance of signal abundance between proteins of different expression levels, therefore avoiding signal dominance of highly expressed proteins in combinatorial barcoding.

Taking advantage of the simplicity, scalability, and adaptability of our platform, we were able to precisely evaluate cytoarchitecture and capture characteristic structures that often exceed the thickness of ultra-thin sections. For example, we managed to characterize and quantify entire amyloid plaques with diameter ranging from tens to hundreds of micrometers in human brains diagnosed with Alzheimer’s Disease. By expanding sampling volume, we were more likely to profile sparse cells with lower bias and characterize patterns with local heterogeneity. After acquiring the brain images of patients diagnosed with Alzheimer’s Disease and control, we confirmed that most of our observations were consistent with conclusions from previous reports based on various experimental methods, suggesting the robustness of our method. For example, although the role of calcium binding proteins in the progression of AD is still controversial, patient dependent, and brain region dependent according to different reports, we reported the spatial distribution of PV+, CB+, CR+ neurons with respect to cortical layers, which is similar to previous observations. Specific combinations of the three CBPs were observed to co-express in double positive neurons in OFC and PFC as in other brain regions. Moreover, as a common marker of astrocytes of our particular interest, GFAP+ cells were captured and analyzed together with other neuronal and microglial markers in OFC and PFC of both brain samples. We observed the same pattern of dense, long, unbranched processes of interlaminar astrocytes in upper layers of control human brain samples as reported by other spatial proteomics platform[61], whereas we didn't spot such patterns in corresponding cortical layers in AD brain samples. We weren't able to detect and segment the soma of astrocytes in a similar way as microglia because of these dense processes of interlaminar astrocytes.

In summary, we report the development of a versatile proteomic mapping platform for multiplexed cellular characterization. This technology enables spatial proteomic detection on volumetric tissues with compatibility to common instrumentation, reasonable experimental cost, and applicability to various types of antibodies, encouraging the implementation of 3D spatial proteomics to more laboratories. As the first attempt to incorporate combinatorial barcoding strategy to spatial proteomics, we envision that our spatial proteomic platform will contribute to enhancing the throughput of protein immunolabeling. We believe with cumulative efforts hereafter, our spatial proteomic mapping platform with combinatorial barcoding strategy will provide more insights of biological questions in a more systematic and efficient way.

6.2 Future directions

Our spatial proteomic mapping platform exhibited great adaptability to confocal microscopy commonly equipped by many labs on millimeter scaled tissues. We demonstrated its performance using spinning disk confocal microscope with high resolution objectives (25X and 63X). For thicker tissue volumes scaling from millimeters above, we envision that the efficiency of image acquisition can be further improved using Selective Plane Illumination Microscopy (SPIM) as sample dimension increases. Furthermore, the high-quality, high-resolution images generated through the pipeline were proved to be compatible with existing imaging processing techniques, such as stitching, blob detection, surface detection and various statistical analysis with ImageJ or Imaris. We expect that the current image analysis will benefit from the advances of machine learning based signal detection algorithms for barcode calling and cell identification with higher accuracy and efficiency.

Besides cell detection and profiling, the high resolution 3D protein map generated by our platform has enabled the quantitative evaluation of spatial dependence between relevant cells and structures. Microglia are known to play key roles in the accumulation, internalization and clearance of amyloid deposits. We were able to profile microglia based on their relative locations to local amyloid plaques, thus to conclude the positive correlation between microglia presence and AD pathology. With more advanced computational analyzing tools applied to our dataset, we envision that cellular categorization based on their relative locations to amyloid plaques can be achieved with better accuracy.

Lastly, leveraging the potentials of our spatial proteomic mapping platform, we expect to perform highly multiplexed proteomic profiling on human brain tissues using combinatorial barcoding strategy facilitated by stochastic sparse labeling. In the current proof of concept experiments, we included only a short list of commonly used cell type markers for brain research. Yet we didn’t realize automated spot detection and barcode reading due to the challenges of lack of a microfluidic buffer delivery system and lack of practical expertise of coping with combinatorial barcode reading in highly multiplexed datasets.

References

1. Langseth, C. M. *et al.* Comprehensive in situ mapping of human cortical transcriptomic cell types. *Commun. Biol.* **4**, 998 (2021).
2. Siletti, K. *et al.* Transcriptomic diversity of cell types across the adult human brain. *Science* **382**, eadd7046 (2023).
3. Park, Y. G. *et al.* Protection of tissue physicochemical properties using polyfunctional crosslinkers. *Nat. Biotechnol.* **37**, 73 (2019).
4. Fazal, F. M. *et al.* Atlas of Subcellular RNA Localization Revealed by APEX-Seq. *Cell* **178**, 473-490.e26 (2019).
5. Rodriques, S. G. *et al.* Slide-seq: A scalable technology for measuring genome-wide expression at high spatial resolution. *Science* **363**, 1463–1467 (2019).
6. Geier, B. *et al.* Spatial metabolomics of in situ host–microbe interactions at the micrometre scale. *Nature Microbiology* **5**, 498–510 (2020).
7. Yuan, Z. *et al.* SEAM is a spatial single nuclear metabolomics method for dissecting tissue microenvironment. *Nat. Methods* **18**, 1223–1232 (2021).
8. Choi, S. W., Guan, W. & Chung, K. Basic principles of hydrogel-based tissue transformation technologies and their applications. *Cell* **184**, 4115–4136 (2021).
9. Sylwestrak, E. L., Rajasethupathy, P., Wright, M. A., Jaffe, A. & Deisseroth, K. Multiplexed Intact-Tissue Transcriptional Analysis at Cellular Resolution. *Cell* **164**, 792–804 (2016).
10. Wang, Y. *et al.* EASI-FISH for thick tissue defines lateral hypothalamus spatio-molecular organization. *Cell* **184**, 6361-6377.e24 (2021).
11. Wang, F. *et al.* RNAscope: A novel in situ RNA analysis platform for formalin-fixed, paraffin-embedded tissues. *J. Mol. Diagn.* **14**, 22–29 (2012).
12. Eng, C. H. L. *et al.* Transcriptome-scale super-resolved imaging in tissues by RNA seqFISH+. *Nature* **568**, 235–239 (2019).
13. Chen, K. H., Boettiger, A. N., Moffitt, J. R., Wang, S. & Zhuang, X. Spatially resolved, highly multiplexed RNA profiling in single cells. *Science* **348**, 1360–1363 (2015).
14. Codeluppi, S. *et al.* Spatial organization of the somatosensory cortex revealed by osmFISH. *Nat. Methods* **15**, 932–935 (2018).
15. Shi, H. *et al.* Highly multiplexed spatial mapping of microbial communities. *Nature* **588**, 676–681 (2020).
16. Vu, T. *et al.* Spatial transcriptomics using combinatorial fluorescence spectral and lifetime encoding, imaging and analysis. *Nat. Commun.* **13**, 1–14 (2022).
17. Lee, J. H. *et al.* Fluorescent in situ sequencing (FISSEQ) of RNA for gene expression profiling in intact cells and tissues. *Nat. Protoc.* **10**, 442–458 (2015).

18. Chen, X., Sun, Y. C., Church, G. M., Lee, J. H. & Zador, A. M. Efficient in situ barcode sequencing using padlock probe-based BaristaSeq. *Nucleic Acids Res.* **46**, 1–10 (2018).

19. Wang, X. *et al.* Three-dimensional intact-tissue sequencing of single-cell transcriptional states. *Science* **361**, (2018).

20. Alon, S. *et al.* Expansion sequencing: Spatially precise in situ transcriptomics in intact biological systems. *Science* **371**, (2021).

21. Vickovic, S. *et al.* High-definition spatial transcriptomics for in situ tissue profiling. *Nat. Methods* **16**, 987–990 (2019).

22. Liu, Y. *et al.* High-Spatial-Resolution Multi-Omics Sequencing via Deterministic Barcoding in Tissue. *Cell* **183**, 1665-1681.e18 (2020).

23. Lee, Y. *et al.* Xyzeq: Spatially resolved single-cell RNA sequencing reveals expression heterogeneity in the tumor microenvironment. *Science Advances* **7**, 1–15 (2021).

24. Vickovic, S. *et al.* SM-Omics is an automated platform for high-throughput spatial multi-omics. *Nat. Commun.* **13**, (2022).

25. Jungmann, R. *et al.* Multiplexed 3D cellular super-resolution imaging with DNA-PAINT and Exchange-PAINT. *Nat. Methods* **11**, 313–318 (2014).

26. Goltsev, Y. *et al.* Deep Profiling of Mouse Splenic Architecture with CODEX Multiplexed Imaging. *Cell* **174**, 968-981.e15 (2018).

27. Saka, S. K. *et al.* Immuno-SABER enables highly multiplexed and amplified protein imaging in tissues. *Nat. Biotechnol.* **37**, 1080–1090 (2019).

28. Guo, S. M. *et al.* Multiplexed and high-throughput neuronal fluorescence imaging with diffusible probes. *Nat. Commun.* **10**, (2019).

29. Keren, L. *et al.* MIBI-TOF: A multiplexed imaging platform relates cellular phenotypes and tissue structure. *Science Advances* **5**, (2019).

30. Passarelli, M. K. *et al.* The 3D OrbiSIMS - Label-free metabolic imaging with subcellular lateral resolution and high mass-resolving power. *Nat. Methods* **14**, 1175–1183 (2017).

31. Ganesh, S. *et al.* Spatially resolved 3D metabolomic profiling in tissues. *Science Advances* **7**, 1–17 (2021).

32. Valm, A. M., Mark Welch, J. L. & Borisy, G. G. CLASI-FISH: principles of combinatorial labeling and spectral imaging. *Syst. Appl. Microbiol.* **35**, 496–502 (2012).

33. Levesque, M. J. & Raj, A. Single-chromosome transcriptional profiling reveals chromosomal gene expression regulation. *Nat. Methods* **10**, 246–248 (2013).

34. Knopman, D. S. *et al.* Alzheimer disease. *Nat. Rev. Dis. Primers* **7**, 33 (2021).

35. 2021 Alzheimer's disease facts and figures. *Alzheimers. Dement.* **17**, 327–406 (2021).

36. Abubakar, M. B. *et al.* Alzheimer’s disease: An update and insights into pathophysiology. *Front. Aging Neurosci.* **14**, 742408 (2022).

37. Haass, C. & Selkoe, D. J. Soluble protein oligomers in neurodegeneration: lessons from the Alzheimer’s amyloid beta-peptide. *Nat. Rev. Mol. Cell Biol.* **8**, 101–112 (2007).

38. Gallardo, G. & Holtzman, D. M. Amyloid-β and tau at the Crossroads of Alzheimer’s disease. *Adv. Exp. Med. Biol.* **1184**, 187–203 (2019).

39. Pooler, A. M., Noble, W. & Hanger, D. P. A role for tau at the synapse in Alzheimer’s disease pathogenesis. *Neuropharmacology* **76 Pt A**, 1–8 (2014).

40. Eftekharzadeh, B. *et al.* Tau protein disrupts nucleocytoplasmic transport in Alzheimer’s disease. *Neuron* **99**, 925-940.e7 (2018).

41. Soleimany, A. P. *et al.* Activatable Zymography Probes Enable in Situ Localization of Protease Dysregulation in Cancer. *Cancer Res.* **81**, 213–224 (2021).

42. Stickels, R. R. *et al.* Highly sensitive spatial transcriptomics at near-cellular resolution with Slide-seqV2. *Nat. Biotechnol.* **39**, 313–319 (2021).

43. Merritt, C. R. *et al.* Multiplex digital spatial profiling of proteins and RNA in fixed tissue. *Nat. Biotechnol.* **38**, 586–599 (2020).

44. Unterauer, E. M. *et al.* Spatial proteomics in neurons at single-protein resolution. *bioRxiv* (2023) doi:10.1101/2023.05.17.541210.

45. Sanchez-Molina, P. *et al.* Single-cell spatial proteomic analysis by multiplexed imaging enables identification of microglial heterogeneity in Alzheimer’s disease human brain. *Research Square* (2023) doi:10.21203/rs.3.rs-2870341/v1.

46. Taniguchi, Y. *et al.* Quantifying E. coli Proteome and Transcriptome with Single-Molecule Sensitivity in Single Cells. *Science* **329**, 533–539 (2011).

47. Marguerat, S. *et al.* Quantitative analysis of fission yeast transcriptomes and proteomes in proliferating and quiescent cells. *Cell* **151**, 671–683 (2012).

48. Lewis, S. M. *et al.* Spatial omics and multiplexed imaging to explore cancer biology. *Nature Methods* vol. 18 997–1012 Preprint at https://doi.org/10.1038/s41592-021-01203-6 (2021).

49. Tengerdy, R. P. & Small, W. H. Reaction kinetic studies of the antigen-antibody reaction. *Nature* **210**, 708–710 (1966).

50. Howat, W. J. & Wilson, B. A. Tissue fixation and the effect of molecular fixatives on downstream staining procedures. *Methods* **70**, 12–19 (2014).

51. Paavilainen, L. *et al.* The impact of tissue fixatives on morphology and antibody-based protein profiling in tissues and cells. *J. Histochem. Cytochem.* **58**, 237–246 (2010).

52. DiDomenico, C. D. *et al.* The effect of antibody size and mechanical loading on solute diffusion through the articular surface of cartilage. *J. Biomech. Eng.* **139**, (2017).

53. Reverberi, R. & Reverberi, L. Factors affecting the antigen-antibody reaction. *Blood Transfus.* **5**, 227–240 (2007).

54. Sadana, A. & Sii, D. Binding kinetics of antigen by immobilized antibody: influence of reaction order and external diffusional limitations. *Biosens. Bioelectron.* **7**, 559–568 (1992).

55. Sadana, A. & Vo-Dinh, T. Antibody-antigen binding kinetics. A model for multivalency antibodies for large antigen systems. *Appl. Biochem. Biotechnol.* **67**, 1–22 (1997).

56. Lee, E. *et al.* ACT-PRESTO: Rapid and consistent tissue clearing and labeling method for 3-dimensional (3D) imaging. *Sci. Rep.* **6**, 18631 (2016).

57. Matsumoto, K. *et al.* Advanced CUBIC tissue clearing for whole-organ cell profiling. *Nat. Protoc.* **14**, 3506–3537 (2019).

58. Kim, S.-Y. *et al.* Stochastic electrotransport selectively enhances the transport of highly electromobile molecules. *Proc. Natl. Acad. Sci. U. S. A.* **112**, E6274-83 (2015).

59. Murray, E. *et al.* Simple, Scalable Proteomic Imaging for High-Dimensional Profiling of Intact Systems. *Cell* **163**, 1500–1514 (2015).

60. Ku, T. *et al.* Elasticizing tissues for reversible shape transformation and accelerated molecular labeling. *Nat. Methods* 1–5 (2020).

61. Park, J. *et al.* Integrated platform for multi-scale molecular imaging and phenotyping of the human brain. *bioRxiv* (2022) doi:10.1101/2022.03.13.484171.

62. Cai, R. *et al.* Whole-mouse clearing and imaging at the cellular level with vDISCO. *Nat. Protoc.* **18**, 1197–1242 (2023).

63. Yun, D. H. *et al.* Ultrafast immunostaining of organ-scale tissues for scalable proteomic phenotyping. *bioRxiv* 660373 (2019) doi:10.1101/660373.

64. Tang, F. *et al.* mRNA-Seq whole-transcriptome analysis of a single cell. *Nat. Methods* **6**, 377–382 (2009).

65. Shalek, A. K. *et al.* Single-cell transcriptomics reveals bimodality in expression and splicing in immune cells. *Nature* **498**, 236–240 (2013).

66. Habib, N. *et al.* Massively parallel single-nucleus RNA-seq with DroNc-seq. *Nat. Methods* **14**, 955–958 (2017).

67. Grindberg, R. V. & Yee-Greenbaum, J. RNA-sequencing from single nuclei. *Proc. Natl. Acad. Sci. U. S. A.* **110**, 19802–19807 (2013).

68. Krishnaswami, S. R. *et al.* Using single nuclei for RNA-seq to capture the transcriptome of postmortem neurons. *Nat. Protoc.* **11**, 499–524 (2016).

69. Uhlén, M. *et al.* Tissue-based map of the human proteome. *Science* **347**, (2015).

70. Thul, P. J. *et al.* A subcellular map of the human proteome. *Science* **356**, (2017).

71. Sharma, K. *et al.* Cell type- and brain region-resolved mouse brain proteome. *Nat. Neurosci.* **18**, 1819–1831 (2015).

72. Blackman, M. L., Royzen, M. & Fox, J. M. Tetrazine ligation: Fast bioconjugation based on inverse-electron-demand Diels-Alder reactivity. *J. Am. Chem. Soc.* **130**, 13518–13519 (2008).
73. Kishi, J. Y. *et al.* SABER amplifies FISH: enhanced multiplexed imaging of RNA and DNA in cells and tissues. *Nat. Methods* **16**, 533–544 (2019).
74. Summer, H., Grämer, R. & Dröge, P. Denaturing urea polyacrylamide gel electrophoresis (Urea PAGE). *J. Vis. Exp.* 3–5 (2009).
75. Westphal, V. *et al.* Video-rate far-field optical nanoscopy dissects synaptic vesicle movement. *Science* **320**, 246–249 (2008).
76. Rust, M. J., Bates, M. & Zhuang, X. Sub-diffraction-limit imaging by stochastic optical reconstruction microscopy (STORM). *Nat. Methods* **3**, 793–795 (2006).
77. Liu, H. *et al.* Visualizing long-term single-molecule dynamics in vivo by stochastic protein labeling. *Proc. Natl. Acad. Sci. U. S. A.* **115**, 343–348 (2017).
78. Mathys, H. *et al.* Single-cell transcriptomic analysis of Alzheimer's disease. *Nature* **570**, 332–337 (2019).
79. Morabito, S. *et al.* Single-nucleus chromatin accessibility and transcriptomic characterization of Alzheimer's disease. *Nat. Genet.* **53**, 1143–1155 (2021).
80. Gerrits, E. *et al.* Distinct amyloid-β and tau-associated microglia profiles in Alzheimer's disease. *Acta Neuropathol.* **141**, 681–696 (2021).
81. Chen, S. *et al.* Spatially resolved transcriptomics reveals genes associated with the vulnerability of middle temporal gyrus in Alzheimer's disease. *Acta Neuropathol. Commun.* **10**, 188 (2022).
82. Gabitto, M. I. *et al.* Integrated multimodal cell atlas of Alzheimer's disease. *Res. Sq.* (2023) doi:10.21203/rs.3.rs-2921860/v1.
83. Deture, M. A. & Dickson, D. W. The neuropathological diagnosis of Alzheimer's disease. *Molecular Neurodegeneration 2019 14:1* **14**, 1–18 (2019).
84. Brady, D. R. & Mufson, E. J. Parvalbumin-immunoreactive neurons in the hippocampal formation of Alzheimer's diseased brain. *Neuroscience* **80**, 1113–1125 (1997).
85. Solodkin, A., Veldhuizen, S. D. & Van Hoesen, G. W. Contingent Vulnerability of Entorhinal Parvalbumin-Containing Neurons in Alzheimer's Disease. *Journal of Neuroscience* **16**, 3311–3321 (1996).
86. Mikkonen, M., Alafuzoff, I., Tapiola, T., Soininen, H. & Miettinen, R. Subfield- and layer-specific changes in parvalbumin, calretinin and calbindin-D28k immunoreactivity in the entorhinal cortex in Alzheimer's disease. *Neuroscience* **92**, 515–532 (1999).
87. Saiz-Sanchez, D., Ubeda-Baon, I., De La Rosa-Prieto, C. & Martinez-Marcos, A. Differential expression of interneuron populations and correlation with amyloid-β deposition in the olfactory cortex of an AβPP/PS1 transgenic mouse model of Alzheimer's disease. *J. Alzheimers. Dis.* **31**, 113–129 (2012).

88. Zallo, F., Gardenal, E., Verkhratsky, A. & Rodríguez, J. J. Loss of calretinin and parvalbumin positive interneurones in the hippocampal CA1 of aged Alzheimer's disease mice. *Neurosci. Lett.* **681**, 19–25 (2018).

89. Hof, P. R. *et al.* Parvalbumin-Immunoreactive Neurons in the Neocortex are Resistant to Degeneration in Alzheimer's Disease. *J. Neuropathol. Exp. Neurol.* **50**, 451–462 (1991).

90. Ferrer, I., Soriano, E., Tunon, T., Fonseca, M. & Guionnet, N. Parvalbumin immunoreactive neurons in normal human temporal neocortex and in patients with Alzheimer's disease. *J. Neurol. Sci.* **106**, 135–141 (1991).

91. Sampson, V. L., Morrison, J. H. & Vickers, J. C. The Cellular Basis for the Relative Resistance of Parvalbumin and Calretinin Immunoreactive Neocortical Neurons to the Pathology of Alzheimer's Disease. *Exp. Neurol.* **145**, 295–302 (1997).

92. Leuba, G., Kraftsik, R. & Saini, K. Quantitative Distribution of Parvalbumin, Calretinin, and Calbindin D-28k Immunoreactive Neurons in the Visual Cortex of Normal and Alzheimer Cases. *Exp. Neurol.* **152**, 278–291 (1998).

93. Hof, P. R., Nimchinsky, E. A., Celio, M. R., Bouras, C. & Morrison, J. H. Calretinin-immunoreactive neocortical interneurons are unaffected in Alzheimer's disease. *Neurosci. Lett.* **152**, 145–149 (1993).

94. Wang, X., L. Michaelis, M. & K. Michaelis, E. Functional genomics of brain aging and alzheimers disease: Focus on selective neuronal vulnerability. *Curr. Genomics* **11**, 618–633 (2010).

95. O'Banion, M. K., Coleman, P. D. & Callahan, L. M. Regional neuronal loss in aging and Alzheimer's disease: a brief review. *Semin. Neurosci.* **6**, 307–314 (1994).

96. Rinne, J. O., Paljärvi, L. & Rinne, U. K. Neuronal size and density in the nucleus basalis of Meynert in Alzheimer's disease. *J. Neurol. Sci.* **79**, 67–76 (1987).

97. Vereecken, T. H. L. G., Vogels, O. J. M. & Nieuwenhuys, R. Neuron loss and shrinkage in the amygdala in Alzheimer's disease. *Neurobiol. Aging* **15**, 45–54 (1994).

98. Vogels, O. J. M. *et al.* Cell loss and shrinkage in the nucleus basalis Meynert complex in Alzheimer's disease. *Neurobiol. Aging* **11**, 3–13 (1990).

99. Arnold, S. E., Hyman, B. T., Flory, J., Damasio, A. R. & Van Hoesen, G. W. The topographical and neuroanatomical distribution of neurofibrillary tangles and neuritic plaques in the cerebral cortex of patients with Alzheimer's disease. *Cereb. Cortex* **1**, 103–116 (1991).

100. Van Hoesen, G. W. Orbitofrontal cortex pathology in Alzheimer's disease. *Cereb. Cortex* **10**, 243–251 (2000).

101. Rudelli, R. D., Ambler, M. W. & Wisniewski, H. M. Morphology and Distribution of Alzheimer Neuritic (Senile) and Amyloid Plaques in Striatum and Diencephalon. *Acta Neuropathol.* **64**, 273–281 (1984).

102. Kato, S. *et al.* Confocal observation of senile plaques in Alzheimer's disease: Senile plaque morphology and relationship between senile plaques and astrocytes. *Pathol. Int.* **48**, 332–340 (1998).

103. Dickson, T. C. & Vickers, J. C. THE MORPHOLOGICAL PHENOTYPE OF L-AMYLOID PLAQUES AND ASSOCIATED NEURITIC CHANGES IN ALZHEIMER'S DISEASE. *Neuroscience* **105**, 99–107 (2001).

104. Wippold, F. J., Cairns, N., Vo, K., Holtzman, D. M. & Morris, J. C. Neuropathology for the neuroradiologist: Plaques and tangles. *American Journal of Neuroradiology* vol. 29 18–22 Preprint at https://doi.org/10.3174/ajnr.A0781 (2008).

105. Liu, F. *et al.* Focal-type, but not Diffuse-type, Amyloid Beta Plaques are Correlated with Alzheimer's Neuropathology, Cognitive Dysfunction, and Neuroinflammation in the Human Hippocampus. *Neurosci. Bull.* **38**, 1125–1138 (2022).

106. Hornberger, M. *et al.* Orbitofrontal dysfunction discriminates behavioral variant frontotemporal dementia from Alzheimer's disease. *Dement. Geriatr. Cogn. Disord.* **30**, 547–552 (2010).

107. Nagele, R. G. *et al.* Contribution of glial cells to the development of amyloid plaques in Alzheimer's disease. *Neurobiol. Aging* **25**, 663–674 (2004).

108. Frautschy, S. A. *et al.* Microglial response to amyloid plaques in APPsw transgenic mice. *Am. J. Pathol.* **152**, 307–317 (1998).

109. Bolmont, T. *et al.* Dynamics of the microglial/amyloid interaction indicate a role in plaque maintenance. *J. Neurosci.* **28**, 4283–4292 (2008).

110. Lee, C. Y. D. & Landreth, G. E. The role of microglia in amyloid clearance from the AD brain. *J. Neural Transm. (Vienna)* **117**, 949–960 (2010).

111. Hansen, D. V., Hanson, J. E. & Sheng, M. Microglia in Alzheimer's disease. *J. Cell Biol.* **217**, 459–472 (2018).

112. Leng, F. & Edison, P. Neuroinflammation and microglial activation in Alzheimer disease: where do we go from here? *Nat. Rev. Neurol.* **17**, 157–172 (2021).

113. Carniglia, L. *et al.* Neuropeptides and microglial activation in inflammation, pain, and neurodegenerative diseases. *Mediators Inflamm.* **2017**, 5048616 (2017).

114. Stalder, M. *et al.* Association of microglia with amyloid plaques in brains of APP23 transgenic mice. *Am. J. Pathol.* **154**, 1673–1684 (1999).

115. Davis, B. M., Salinas-Navarro, M., Cordeiro, M. F., Moons, L. & De Groef, L. Characterizing microglia activation: a spatial statistics approach to maximize information extraction. *Sci. Rep.* **7**, 1576 (2017).

116. Gober, R. *et al.* Microglia activation in postmortem brains with schizophrenia demonstrates distinct morphological changes between brain regions. *Brain Pathol.* **32**, e13003 (2022).

117. Paasila, P. J., Davies, D. S., Kril, J. J., Goldsbury, C. & Sutherland, G. T. The relationship between the morphological subtypes of microglia and Alzheimer's disease neuropathology. *Brain Pathol.* **29**, 726–740 (2019).

118. Edler, M. K., Mhatre-Winters, I. & Richardson, J. R. Microglia in aging and Alzheimer's disease: A comparative species review. *Cells* **10**, 1138 (2021).

119. Diez, M., Koistinaho, J., Kahn, K., Games, D. & Hökfelt, T. Neuropeptides in hippocampus and cortex in transgenic mice overexpressing V717F beta-amyloid precursor protein--initial observations. *Neuroscience* **100**, 259–286 (2000).

120. Diez, M. *et al.* Neuropeptide alterations in the hippocampal formation and cortex of transgenic mice overexpressing beta-amyloid precursor protein (APP) with the Swedish double mutation (APP23). *Neurobiol. Dis.* **14**, 579–594 (2003).

121. Beal, M. F. *et al.* Neuropeptide Y immunoreactivity is reduced in cerebral cortex in Alzheimer's disease. *Ann. Neurol.* **20**, 282–288 (1986).

122. Chan-Palay, V., Lang, W., Haesler, U., Köhler, C. & Yasargil, G. Distribution of altered hippocampal neurons and axons immunoreactive with antisera against neuropeptide Y in Alzheimer's-type dementia. *J. Comp. Neurol.* **248**, 376–394 (1986).

123. Davies, C. A., Morroll, D. R., Prinja, D., Mann, D. M. & Gibbs, A. A quantitative assessment of somatostatin-like and neuropeptide Y-like immunostained cells in the frontal and temporal cortex of patients with Alzheimer's disease. *J. Neurol. Sci.* **96**, 59–73 (1990).

124. Duarte-Neves, J., Pereira de Almeida, L. & Cavadas, C. Neuropeptide Y (NPY) as a therapeutic target for neurodegenerative diseases. *Neurobiol. Dis.* **95**, 210–224 (2016).

125. Li, C. *et al.* Roles of neuropeptide Y in neurodegenerative and neuroimmune diseases. *Front. Neurosci.* **13**, 869 (2019).

126. Krstic, D. & Knuesel, I. Deciphering the mechanism underlying late-onset Alzheimer disease. *Nat. Rev. Neurol.* **9**, 25–34 (2013).

127. Chan-Palay, V. & Yasargil, G. Immunocytochemistry of human brain tissue with a polyclonal antiserum against neuropeptide Y. *Anat. Embryol. (Berl.)* **174**, 27–33 (1986).

128. Van Reeth, O. *et al.* Distribution of neuropeptide Y immunoreactivity in human visual cortex and underlying white matter. *Peptides* **8**, 1107–1117 (1987).

129. Hijazi, S., Smit, A. B. & van Kesteren, R. E. Fast-spiking parvalbumin-positive interneurons in brain physiology and Alzheimer's disease. *Mol. Psychiatry* (2023) doi:10.1038/s41380-023-02168-y.

130. Schleicher, A., Morosan, P., Amunts, K. & Zilles, K. Quantitative architectural analysis: a new approach to cortical mapping. *J. Autism Dev. Disord.* **39**, 1568–1581 (2009).

131. Amunts, K. & Zilles, K. Architectonic mapping of the human brain beyond brodmann. *Neuron* **88**, 1086–1107 (2015).

132. Mai, H. *et al.* Whole-body cellular mapping in mouse using standard IgG antibodies. *Nat. Biotechnol.* (2023) doi:10.1038/s41587-023-01846-0.

133. Caberlotto, L., Fuxe, K., Sedvall, G. & Hurd, Y. L. Localization of neuropeptide Y Y1 mRNA in the human brain: abundant expression in cerebral cortex and striatum. *Eur. J. Neurosci.* **9**, 1212–1225 (1997).

134. Vasile, F., Dossi, E. & Rouach, N. Human astrocytes: structure and functions in the healthy brain. *Brain Struct. Funct.* **222**, 2017–2029 (2017).

135. Colombo, J. A., Quinn, B. & Puissant, V. Disruption of astroglial interlaminar processes in Alzheimer's disease. *Brain Res. Bull.* **58**, 235–242 (2002).

136. Dudani, J. S., Warren, A. D. & Bhatia, S. N. Harnessing Protease Activity to Improve Cancer Care. (2017) doi:10.1146/annurev-cancerbio.